ULB ÉCOLE POLYTECHNIQUE DE BRUXELLES
UNIVERSITÉ LIBRE DE BRUXELLES

Passive and Active Strategies for Vibration Control of Lightly Damped Structures

Thesis presented by Ahmad PAKNEJAD SEYEDAHMADIAN
with a view to obtaining a PhD Degree in Engineering Sciences and Technology (Docteur en Sciences de l'Ingénieur et Technologie)
Academic year 2020-2021

Supervisor: Professor Christophe COLLETTE
[BEAMS Department]
Co-supervisor: Professor Frederic ROBERT
[BEAMS Department]

Thesis jury:

Prof. Christophe COLLETTE (Université libre de Bruxelles, Supervisor)
Prof. Frederic ROBERT (Université libre de Bruxelles, Co-supervisor)
Prof. Arnaud DERAEMAEKER (Université libre de Bruxelles, Chair)
Prof. Patrick HENDRICK (Université libre de Bruxelles, Secretary)
Prof. Gaetan KERSCHEN (Université de Liege)
Prof. Simon CHESNE (INSA-Lyon)

beams
Precision Mechatronics Laboratory

Abstract

Lightweight designs in engineering applications give rise to flexible structures with extremely low internal damping. Vibrations of these flexible structures due to an unwanted excitation of system resonances may lead to high cyclic fatigue failure and noise propagation. A common method to suppress the vibrations is to increase the damping of the system using one of classical control techniques i.e. passive, active, and/or hybrid. Passive techniques are those control systems which are simply integrated into the structures with no need of external power source for their operations, like viscoelastic damping, piezoelectric and electromagnetic shunt damping, tuned mass damper, etc. However, the control performance of these systems, in terms of the damping ratio and the robustness to uncertainties, is highly limited to the system properties. For example, viscoelastic damping may not perform well at low frequencies and the performance of shunt damping is dependent on the electromechanical coupling between the structure and the transducer. To overcome the passive limitations, it has been proposed to use active control systems, which are less sensitive to system's parameters, to improve the control performance. It requires an integration of sensors and actuators with a feedback loop containing control laws. However, high requirement of the external power source is not favorable for the engineering applications where energy efficiency is the key parameter. The combination of active and passive strategies, known as hybrid control systems, provide a fail-safe configuration with a high control performance and a low power consumption. The price to pay for such configurations is the complexity of the design.

This doctoral thesis first investigates the conceptual designs of all kinds of the classical control systems for a simplified mechanical system. They include 1) the passive shunt using electromagnetic transducer, 2) the active control system using a positive feedback as well as a negative feedback, and 3) the hybrid electromagnetic shunt damper using both an active voltage source as well as an active current source. The next part of this thesis is focused on bladed structures as real-life applications which highly require vibration control due to their low internal damping. Because of the practical reasons, piezoelectric transducers are used for the application of control systems. Finite element model of the structure is made first without piezoelectric patches to optimize the best locations of piezoelectric patches. Then, the model is updated with the piezoelectric patches to numerically simulate different control strategies. The experiments are performed to validate the numerical designs.

Acknowledgements

First and foremost, I am extremely grateful to my supervisor, Prof. Christophe Collette, the director of the Precision Mechatronic Laboratory (PML) at ULB and ULiege. He has been contentiously supportive from the very first days that I met him via Skype meetings. He supported me not only by providing me insightful feedback on my research activity but also by helping me through the rough road I had sometime in my personal life. His ambitious goals in research activities always pushed me to sharpen my thinking and brought my work to a higher level. Working with him means working on the edge of academic and industrial challenges. This was a great opportunity for me to get a better sense of the industrial problems too. I am so delighted to have done my PhD thesis in his laboratory.

My gratitude extends to my co-supervisor, Prof. Frederic Robert, for his help and patience throughout my research project. His problem solving approach inspired me to think outside the box especially at the beginning of my project when I needed to manage my thoughts. He helped me to make the right definitions for the electromechanical concepts such as the passive and the active control strategies as well as the power budget of a system. Thanks to him I could derive the power consumption of the operational amplifier too.

I would like to express my sincere gratitude to Prof. Arnaud Deraemaeker not only for accepting the role of president of my PhD committee, but also for his dedicated support during the past years on my project, my publications, and in particular on my finite element modeling. I am deeply grateful to have worked in a close collaboration with him since he always offered me a nice solution to the problems that I was dealing with. I remember that I was always looking for his comments. Also, thanks to him I got to know the Structural Dynamics Toolbox (SDT) in Matlab to make the finite element model of piezoelectric material in a more convenient way.

I would like to thank Prof. Patrick Hendrick who accepted to be a member of my PhD committee, and to review this doctoral thesis.

I would like to thank Prof. Gaetan Kerschen for his help on my publications, and his support on my work when I was studying the nonlinear vibration and control. I also want to thank him for accepting to be the member of my jury.

I would like to thank Prof. Simon Chesne who gave me the chance to spend time in his lab at INSA-Lyon. I was not lucky enough to finish the exceptionally interesting research that we started together only because of corona crisis. I will definitely miss it. I am very thankful to him not only for his help on my research and publications but also for accepting to be the member of my jury.

My special appreciation goes to Michel Osee for his time and great help throughout the design and development of several electrical circuits. Without his hands-on experience, it would be impossible for me to complete my research.

I was lucky to collaborate with a number of colleagues with whom I shared the main project (Maveric project). I want to thank Ghislain who was always available for exchanging ideas throughout very detailed conversations, and for sharing numerical and experimental knowledge. I also want to acknowledge Guoying for the time that we spend together to validate nonlinear vibration control.

I had a chance to meet excellent people who are my colleagues in PML. In particular, Thomas, Vicente, Jennifer, Dimitri, Cedric, Shashank, and Binlei. Thank you very much my friends for all these nice time that we spent together and for making my working environment so pleasant. I also thank the ULB staff: Ariane for her kind support, and Salvo for his help on manufacturing the mechanical parts.

I would like to acknowledge the financial support of the service public de Wallonie (SPW) with a grant for the Maveric project (WALInnov grant 1610122). This work could not have been possible without your financial support.

Last but not least, I would like to express my tremendous gratitude and appreciation for all my family and close friends. My very special thanks must go to my parents and my sister for their unconditional trust, heart-warming kindness, and endless patience. I also thank Niloufar for her timely encouragement, and for helping me endure the disappointing moments.

Contents

List of Figures

List of Tables

Chapter 1

Introduction

Contents

A turbomachine is a power plant producing a mechanical work in order to drive a secondary system such as a fan of jet engine, a shaft of a helicopter, an electrical generator, etc. Figure 1.1 shows a schematic of the turbomachine designed by General Electric Company for an aircraft engine [1].

Bladed disk assemblies are being used in different stages of the turbomachines. The bladed disk assembly is referred to as a structure consisting of blades mounted on a disk-shaped part as support.

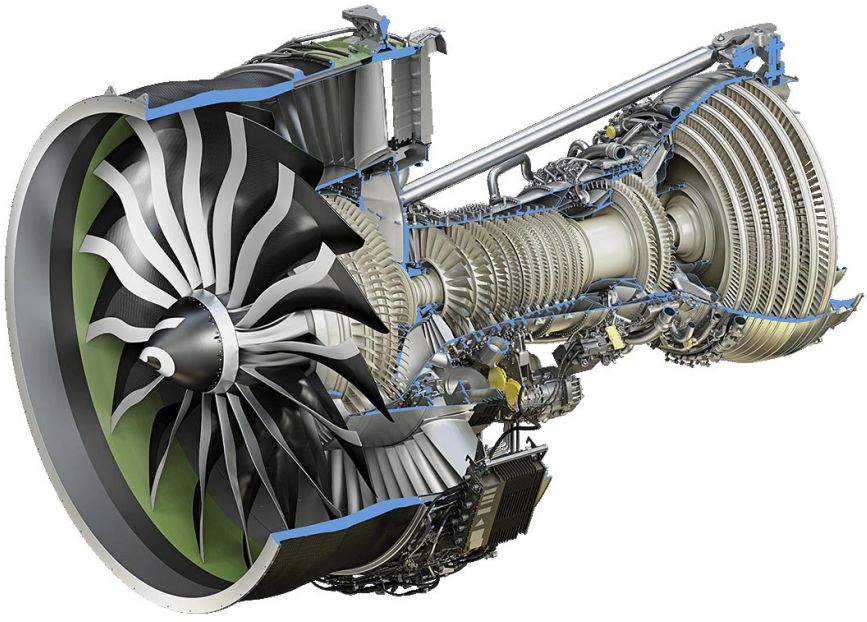

Figure 1.1: General Electric GE9X Cutaway Drawing [1].

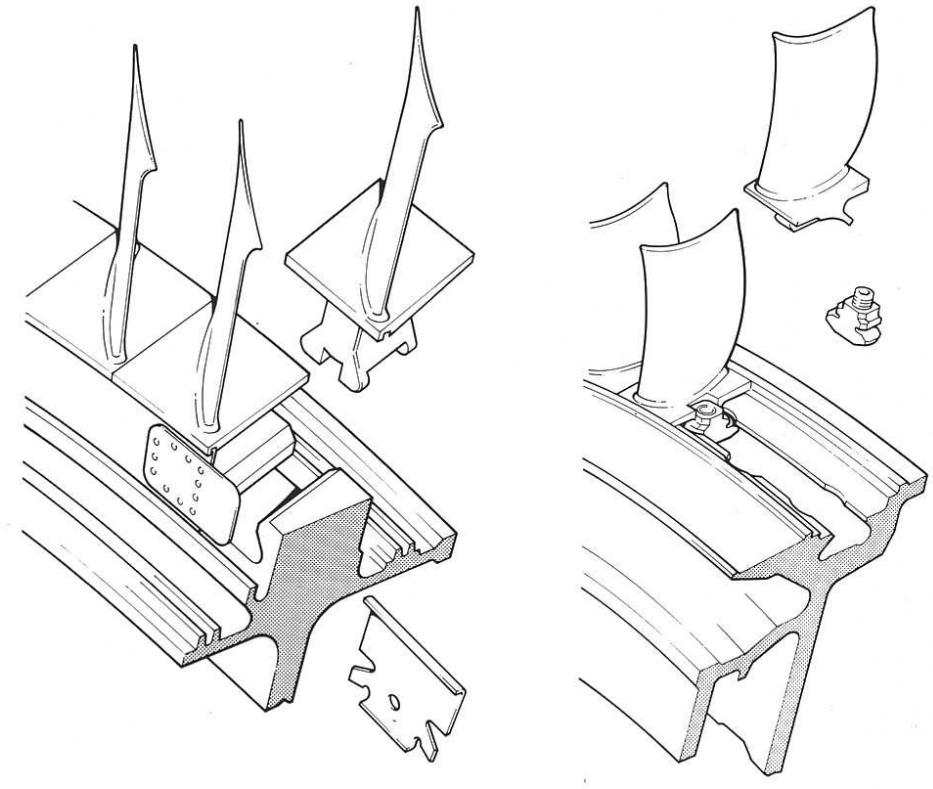

Figure 1.2: Two methods of attaching blades to turbine discs [2].

Figure 1.2 shows two early methods for manufacturing such structures in a way that the blades are attached to the disk using root fixing features [2]. These methods facilitate the maintenance of the machine in case of the need for replacing the blades due to damages. In addition, both fixing solutions provide a considerable damping intrinsic to the blades. However, these advances have severely decreased the energy efficiency of the machine due to the mass added to the structure leading to high centrifugal loads applied to the disk. In order to improve the energy efficiency of the turbomachines, the bladed structures have been redesigned, in the past years, by using new materials and/or new fabrication techniques. Manufacturing blades and disk in a single piece is the new design of such bladed structures which interestingly reduces the mass of the structures. This method, however, makes the maintenance of the machine complicated and most importantly removes the inherent damping of the blades. It is still possible to lighten the machine by replacing the disk to a ring- or drum-shaped structures. The bladed rings is also known as 'blings' and the bladed drum is known as 'blums'. As shown in Figure 1.3, a new design of the monobloc bladed drum called BluM, where the blades have been attached to the drum part using friction welding, has been manufactured by SAFRAN Techspace Aero.
The BluM is the structure of interest in this thesis.

1.1 Vibration of bladed structures

Vibrations of the bladed structures appear due to the unwanted excitation force induced by the fluctuation of gas flows in turbomachines. The presence of dynamic loads can excite the resonances of blades with high levels of vibration due to the lack of enough inherent damping. As shown in Figure 1.4, the vibratory stresses leave the blades susceptible to high cycle fatigue failures [12]. Therefore, any further damping provided to the structure is desirable to extend structural lifetime. Beyond an extended lifetime, a reduction of the blade vibration could also allow a reduction in noise propagation.

Figure 1.3: A CAD view of the monobloc bladed drum (i.e. BluM).

To design a robust vibration damping system, it is first necessary to characterize the dynamic behavior of the BluM in terms of the natural frequencies and mode shapes. Its particular geometry, containing the drum and the blades, makes it more complicated than beams or plates. As shown in Figure 1.5, their vibrations are typically classified into three groups:

- Blades dominated modes where the maximum deformations are mostly distributed on the blades
- Drum dominated modes where the maximum deformations are mostly distributed on the drum
- Coupled modes where the maximum deformations are uniformly distributed on both drum and the blades

Due to the axisymmetry of the structure, the mode shapes appear with N nodal diameters. N can be varied from 0 to n/2, where n is the number of blades. In addition, the mode shapes occur

Figure 1.4: Fan blade failure due to a high cycle fatigue of the blades [3].

in degenerate orthogonal pairs. Both modes of the pair with the same resonance frequency have also the same shape, but are rotated with respect to each other by 90° around the axis of symmetry.

The first 200 resonances of the BluM are shown in Figure 1.6. The natural frequencies corresponding to the drum dominated modes and the coupled modes are well-separated with each others. However, the high modal density resonances occur when the modes of the blades are dominated. In this case, a high number of modes, known as the family of modes, appears in a short range of frequency. The number of modes in a family depends on the number of blades and equal to n/2. The first modes family corresponds to first bending mode of the blades and the second family corresponds to the first torsion mode of the blades. The rigidity of the drum governs the difference between resonance frequencies in each family such that a set of 76 independent resonances happens with the same frequency if the drum was completely rigid and the blades were perfectly identical. Owing to the transmission of the energy of the blades through the flexible drum, the flexibility of the drum makes the blades modes occur with different frequencies and shapes.

Vibration response of turbomachinery bladed structures is extremely subjected to plant uncertainties from different sources. During the normal operation of the machine, centrifugal forces and thermal gradients subject the blades to the static loads. The centrifugal force, induced by the high rotational speed of the structure, can directly affect the static stiffness and subsequently creates resonance uncertainties. In addition, mistuning is another source of resonance uncertainties. Mistuning is referred to small bladed-to-blade variations which occur during the manufacturing of the blades. Therefore, the blades are no longer identical and the rotational periodicity of the

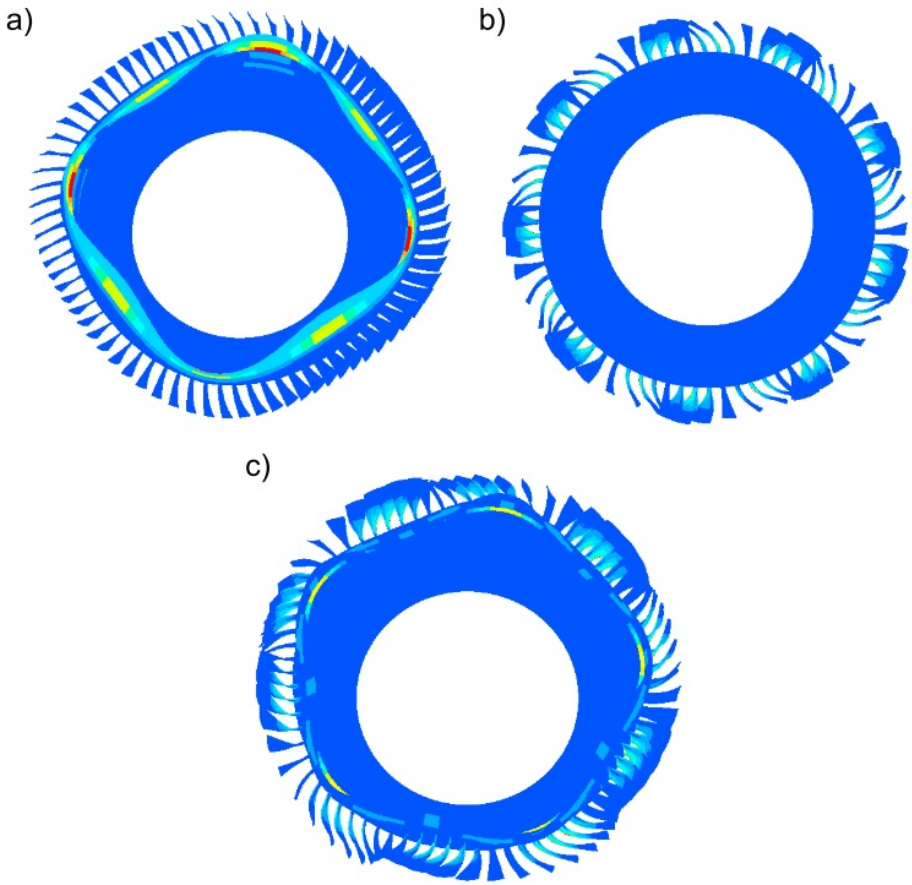

Figure 1.5: Typical mode shapes of the BluM. a) Drum dominant mode with 4 nodal diameters; b) Blade dominant mode with 9 nodal diameters; c) Coupled mode with 5 nodal diameters [4].

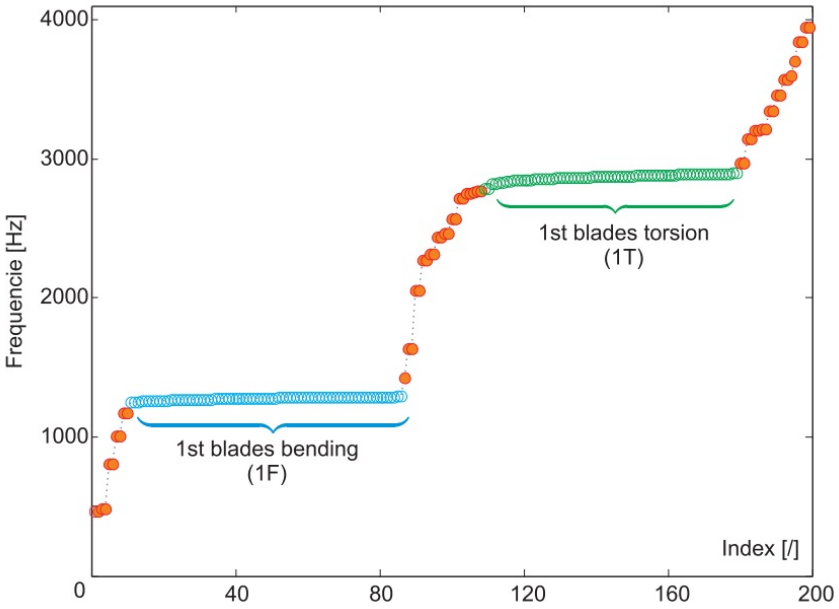

Figure 1.6: Resonance frequencies of the BluM [5].

structure is distorted. Although the mistuning is very complex to be characterized in practice, it can certainly affect the resonance frequencies and mode shapes of the structure.

1.2 Damping of bladed structures

It has been discussed that three main vibration characteristics of the BluM include the low inherent damping, the high modal density resonances, and the plant uncertainties. Therefore, the control system aims at achieving an acceptable control performance (in terms of damping for a broadband vibration resonances) in the presence of the plant variations. However, there is a fundamentally tradeoff between the conflicting goals of the control performance versus robustness to the plant uncertainties. Besides this, there are other requirements on a control system such as the fail-safe design, the power consumption, as well as the stability in terms of gain and phase margins. What follows is a summary of different control strategies.

1.2.1 Passive damping

Passive techniques are those control systems which are simply integrated into the structures with no need of external source of power. Figure 1.7 shows three kinds of the passive control system to suppress the vibration of the system, containing a mass m, a small primary damping c, and the spring k, when it is excited by an external force f_d. According to Figure 1.7a, a relative deformation between the structure and the constraining layer causes shear deformations in the viscoelastic material that dissipate vibration energy. While simple, viscoelastic damping may not perform well at low frequencies [13]. Using friction damping as shown in Figure 1.7b, the mechanical energy is dissipated at the interface between the structure and the rough surface. Despite the fact that friction damping techniques is a broadband vibration absorber like viscoelastic devices, difficulties arise from their highly nonlinear behavior [14]. Another passive control technique is tuned mass damper (TMD) as it is shown in Figure 1.7c. By properly tuning the mass, the spring, and the damping of TMD, it can suppress a target resonance of the primary system. Although TMD is an effective damping technique, its performance is highly related to the mass ratio between the mass of the TMD and the mass of the structure [15]. This means that the better performance comes at the expense of the added mass to the system which is not favorable in our application.

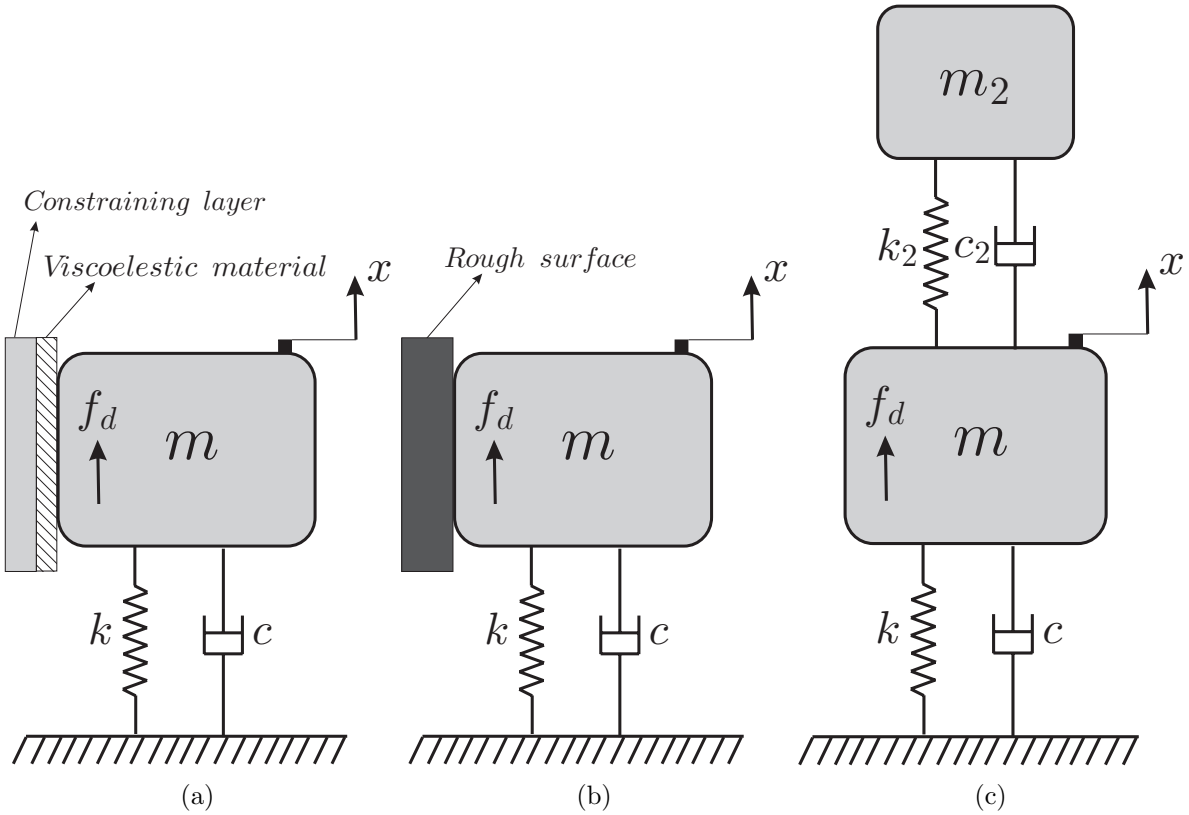

Figure 1.7: Schematic of different passive control systems. (a) Viscoelastic damping. (b) Friction damping. (c) Tuned mass damper.

piezoelectric and electromagnetic transducers are commonly used in the design of the passive control systems when they are connected to a shunt circuit as shown in Figures 1.8a and 1.8b. Those transducers are able to transduce mechanical energy into electrical domain and vice versa. Hence, when the structure is under excitation, the mechanical energy can be transferred to the electrical energy and consequently dissipated by shunting elements. Resistive shunt connected to either piezoelectric [16] or electromagnetic [17] transducers has been used to provide a broadband vibration damping. On the other hand, resonant shunt can enhance the vibration damping of a target mode compared to that of the resistive shunt. The corresponding resonant circuit when a piezoelectric transducer is used differs from that of an electromagnetic transducer. From electrical point of view, a piezoelectric transducer behaves as a capacitor in series to a voltage source (Figures 1.8c); whereas, an electromagnetic transducer acts as an inductor and a resistor in series to a voltage source (Figures 1.8d). Therefore, to form resonant RLC circuit, the inherent capacitance of the piezoelectric is shunted with a resistor as well as an inductor and the inherent inductance of the coil is shunted with a resistor as well as a capacitor. In spite of the interest, such passive techniques are limited by the electromechanical factor which measures the ability of the transducer to convert mechanical energy into the electrical energy and vice versa.

When it comes to rotating structures, practical implementation of the control system becomes a key factor. Clearly, TMD is no longer an option due to the added mass to the structure. The viscoelastic damping, the friction damping and the piezoelectric shunt damping have been designed and developed for the bladed structures. In the following, we will review these techniques.

The viscoelastic material has been used to damp the vibrations of the structures where the blades are attached to the disk using root fixing solutions. As shown in Figure 1.9, Nguyen et al.

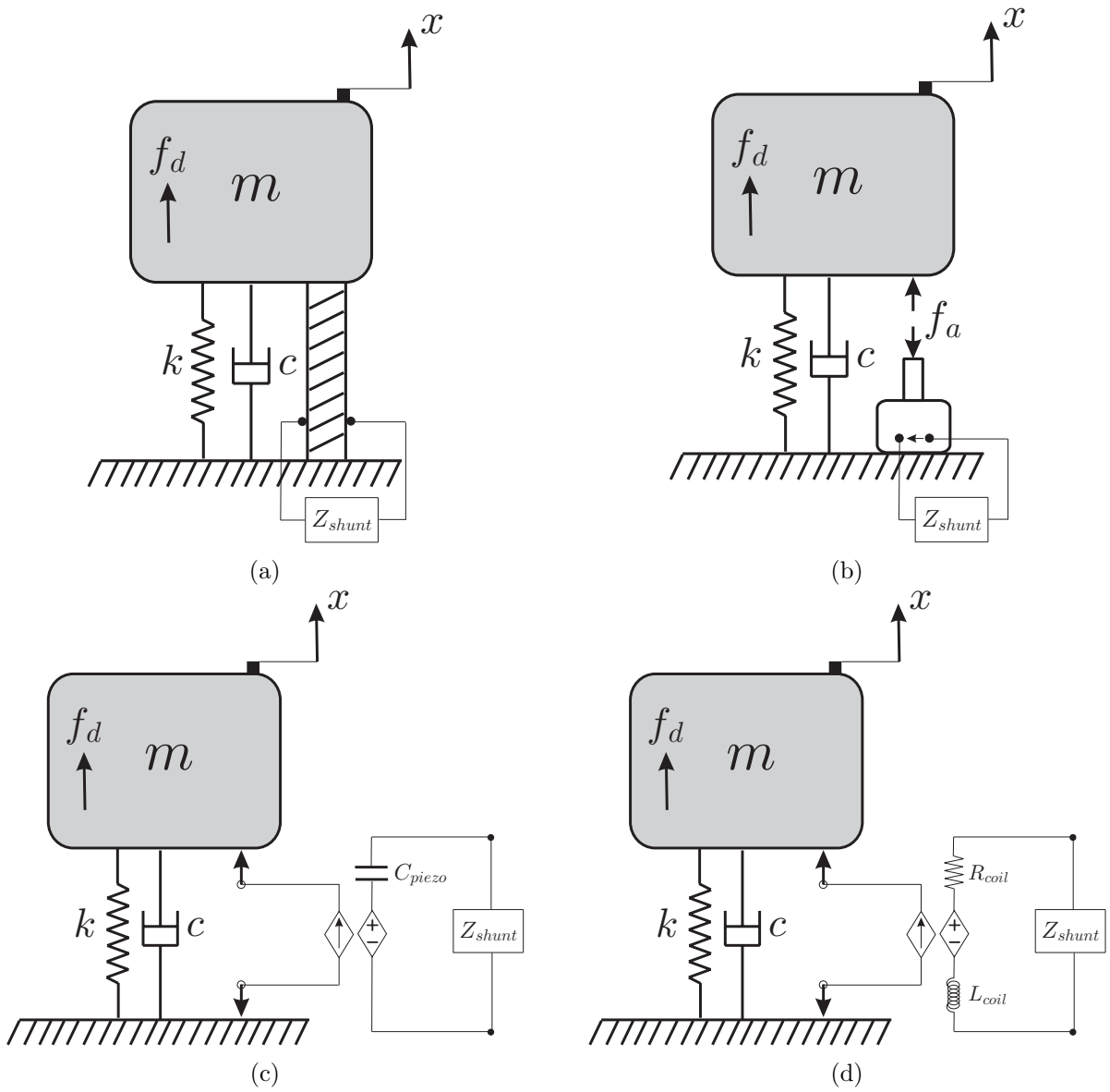

Figure 1.8: Schematic of passive shunt damping using (a) piezoelectric and (b) electromagnetic transducers.

[6] proposed the use of such material at the interface of the blades and the disk for non-monobloc bladed disk assemblies. It is still possible to use this technique on monobloc bladed disk assemblies. However, high temperature severely degrades its performance.

The friction damping techniques have been proposed to suppress the vibration of bladed structures in different ways [18]. For a bladed disk assemblies where the blades are mounted by using root fixing solution, Yeo and Goodman [19] introduced three locations for the use of friction damping devices including (i) at the root of the blades as shown in Figure 1.10a, (ii) between the blades themselves, and/or (iii) at the shrouds. For monobloc bladed disk, Laxalde et al. [20] developed friction damping ring as shown in Figure 1.10b and Stangeland et al. [21] designed friction fingers mechanism illustrated in Figure 1.10c. Nevertheless the efficiency of the friction damping solutions even at the presence of its nonlinear behavior, the new fabrication technique of the bladed assemblies renders impossible the use of such damping systems in practice.

The passive piezoelectric shunt damping has also been the subject of many research ac-

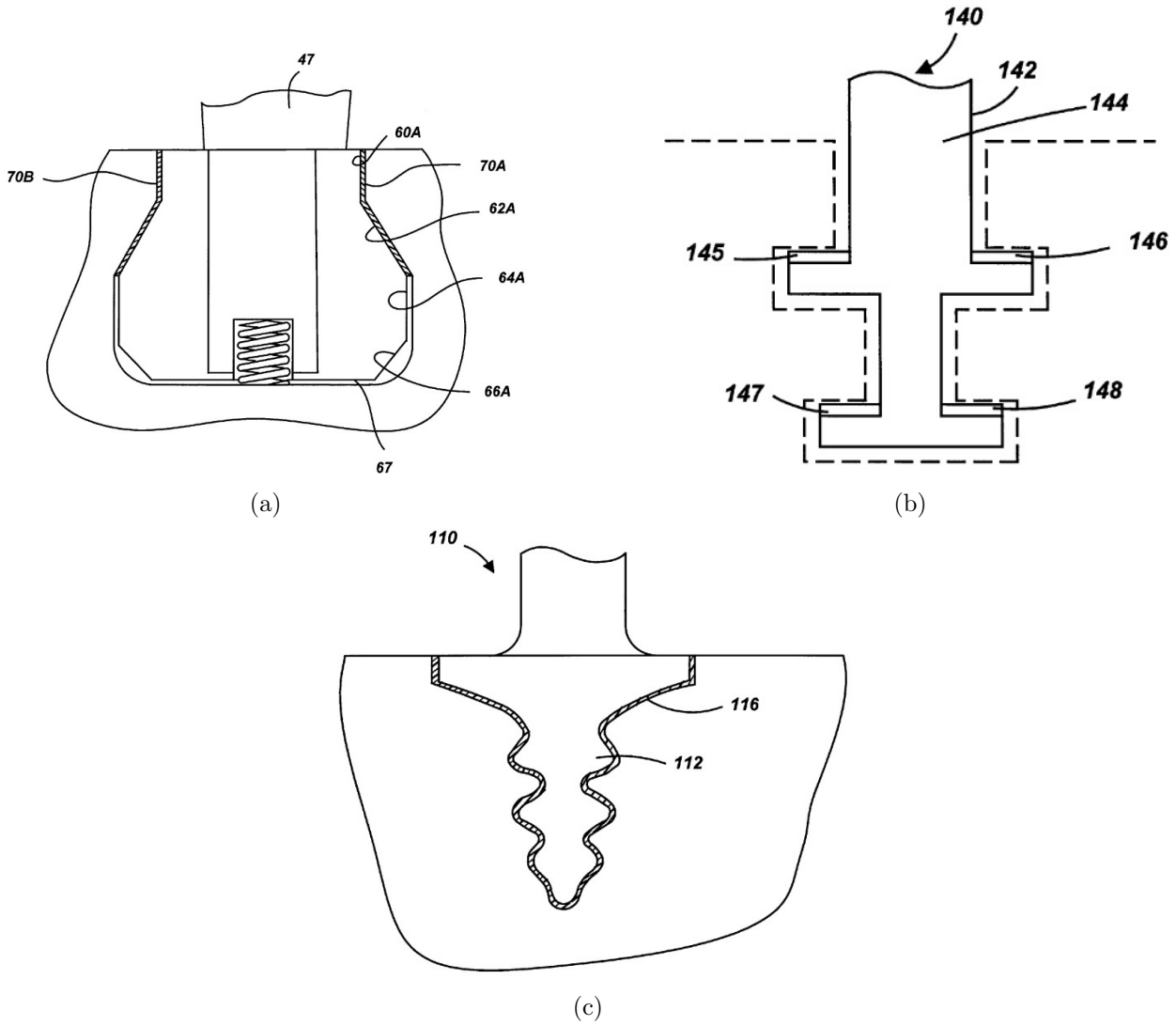

(a) (b)

(c)

Figure 1.9: Using viscoelastic material to damp the vibration of blades attached to the disk with different root fixing solutions such as a) the dovetail root attachment, b) the T-block root attachment, and c) the fir tree root attachment [6]

tivities for bladed structures. It was first studied by Schwarzendahl et al. [22]. The study was performed on a plate-like compressor blade where the maximum amplitude reduction of the first mode of the blade was highlighted to optimize the shunt circuit. In order to reduce the complexity required to implement a passive system targeting multiple modes, Kauffman et al. [23] proposed a semi-active approach using low-power frequency-switching. The use of negative capacitance to enhance the control performance of the passive shunt has been studied on a test-rig of a bladed disk model with eight blades [24]. In these studies, piezoelectric patches were mounted directly on the blade. Although locating patches on the blade can offer a better electromechanical coupling factor since the patches are placed near the maximum strain distribution, they cannot be implemented in practice since they disturb the aerodynamic flow. As shown in Figure 1.11, Mokrani et al. [7] used multiple patches on the internal part of the BluM and tuned the shunt elements using the average frequency of the first bending modes family.

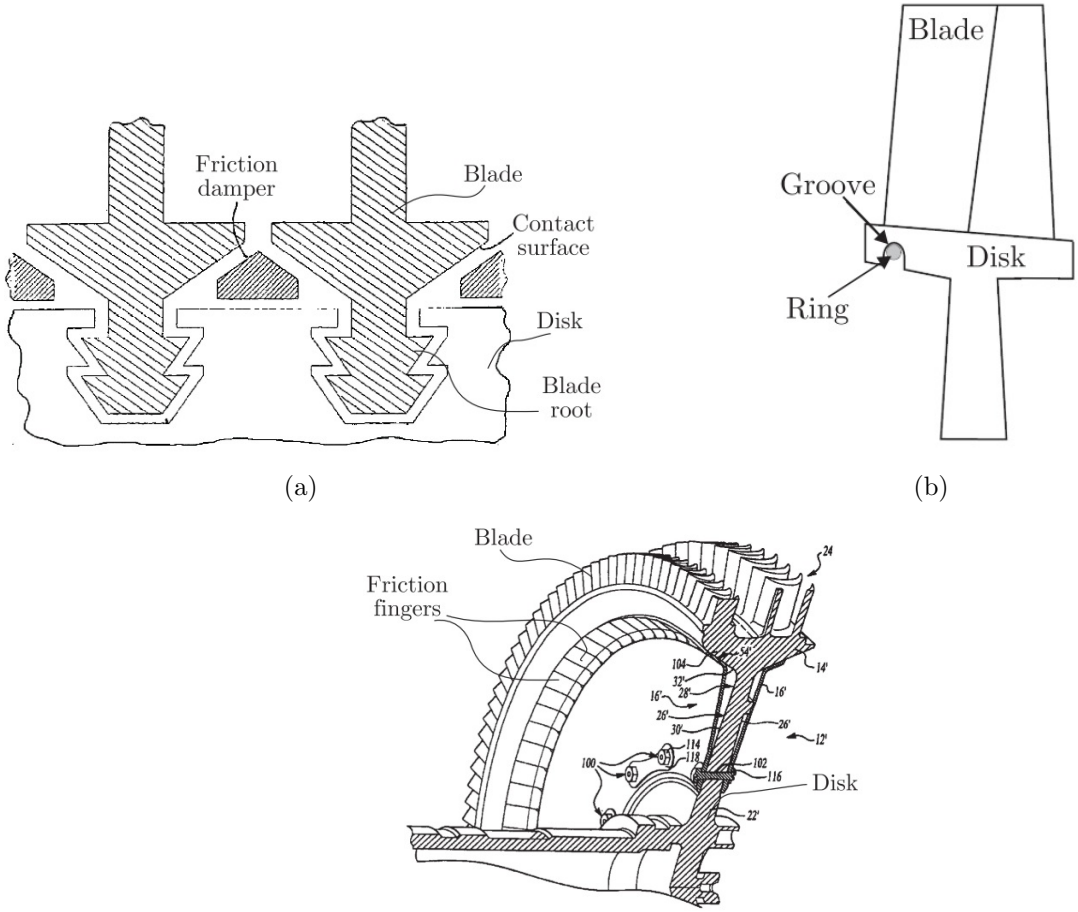

Figure 1.10: Friction damping technique for a) a non-monobloc bladed disk (at the root of blades) and for monobloc bladed disk: b) the friction ring device and c) the friction fingers mechanism

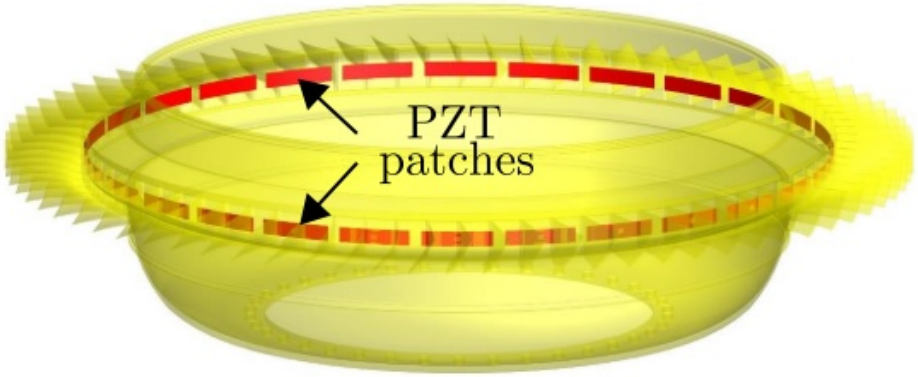

Figure 1.11: For the purpose of the shunt damping used for the BluM, the piezoelectric patches are mounted on the internal part of the structure [7].

1.2.2 Active damping

It has been mentioned that the control performance of these systems is highly limited to the system properties. To overcome the passive limitations and further improve the control performance, it has been proposed to use active control systems, which are less sensitive to system's parameters.

An active control system requires an integration of sensors and actuators with a feedback loop containing control laws [25]. In the literature, different control laws have been proposed successfully when a sensors is collocated with an actuator. These include direct velocity feedback (DVF) [26], positive position feedback (PPF) [27], digital shunt damping [28], integral force feedback (IFF) [29], etc. The choice of the control law for a system depends on the type of sensor/actuator leading to different shapes of the open-loop transfer function in terms of pole/zero pattern.

When a force actuator is combined with a velocity sensor as shown in Figure 1.12, DVF can be simply used as the control law [30] such that the feedback loop can artificially increase the viscous damping of the structure. In practice, the force actuator is found in two commercial types, i.e., the inertial actuator and the reactive actuator shown in Figures 1.12a and 1.12b, respectively. The inertial actuator is a force actuator that is in parallel to a passive mount consisting of a reaction mass supported by a spring attached to a substructure. Its resonance frequency is much lower than the fundamental resonance frequency of the controlled structure due to a very low stiffness of its spring. This may results in high deflections of the proof mass. In order to add viscous damping to the structure, the natural way is to drive the actuator with a signal which is proportional to the velocity. This is called active mass damper (AMD). Although AMD can still increase the damping of the system, the stability of the system is no longer guaranteed for high value of the feedback gain even when the sensor and actuator are collocated [30]. Unlike the inertial actuators where actuation force acts against the inertial mass, reactive actuators can be directly mounted on the ground because of no additional passive mount. Interestingly, such actuators do not suffer from

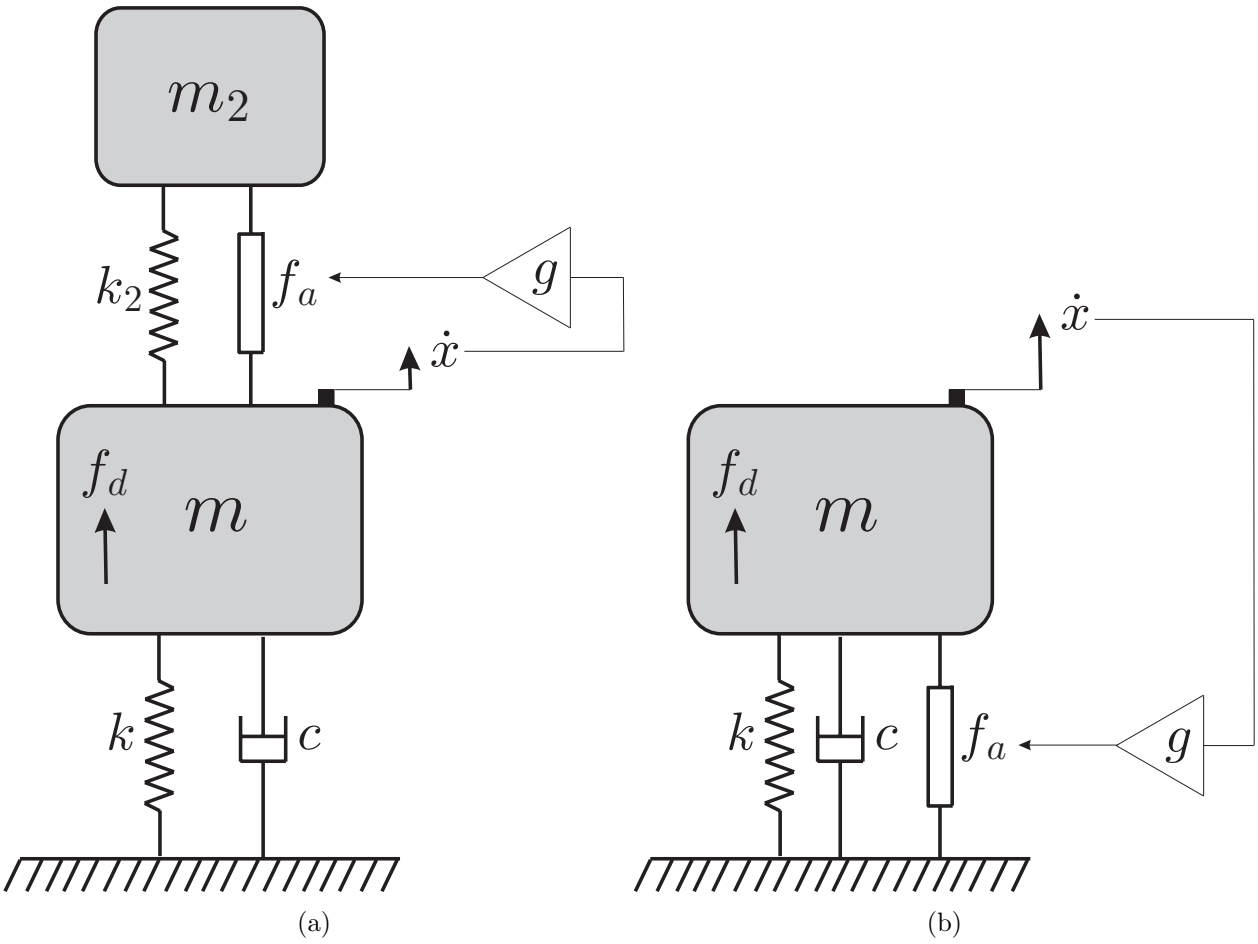

Figure 1.12: Schematic of velocity feedback collocated with a) an inertial force actuator and b) a reactive force actuator.

the aforementioned limitations.

For some applications, DVF suffers from high control effort and spill-over which refers to the amplification of the response at high frequencies. To overcome such limitations, PPF is proposed to be implemented on a system equipped by a displacement sensor collocated with a reactive actuator as shown in Figure 1.13a. In fact, PPF can add high frequency roll-off in a feedback loop since its control law contains either a first- and second-order low-pass filter. In fact, first-order PPF is a multimode vibration control system like DVF; while, second-order PPF is a resonant control which is able to damp a target mode. Properly tuning parameters of PPF can lead to a better control performance in terms of the closed-loop damping compared to DVF. These advantages come at the expense of a lower static response, a lower phase and gain margin, and conditional closed-loop stability. Beside, for collocated piezoelectric patches used as sensor and actuator, the open-loop transfer function has no high frequency roll-off. Therefore, PPF is highly recommended as the control law to avoid high risk of spill-over at frequencies higher than frequency band of interest.

Similar to DVF which artificially increase the damping ratio of a system, IFF is applied on a structure combined with a force sensor between the structure and a force actuator that its time delay or its hysteresis is negligible [29]. The actuator is driven by a signal proportional to the integral of the forces applied to the structure and measured by the sensor as shown in Figure 1.14a. Considering the force is proportional to the acceleration, the control force is proportional to the velocity leading to a higher value of the damping ratio. Although IFF is a robust broadband control system, its performance is limited by the stiffness ratio between the actuator and the primary structure. In order to improve the control performance of a target mode in terms of the closed-loop damping ratio, α-controller, consisting of a double integrator and a real zero, is proposed. For such control laws, the low frequency content is significantly amplified during the integration process which leads to a dynamically softer system. In order to solve this issue, it has been proposed to use a high-pass filter in series with the IFF or α-controller. It is also worth pointing out that piezoelectric stacks

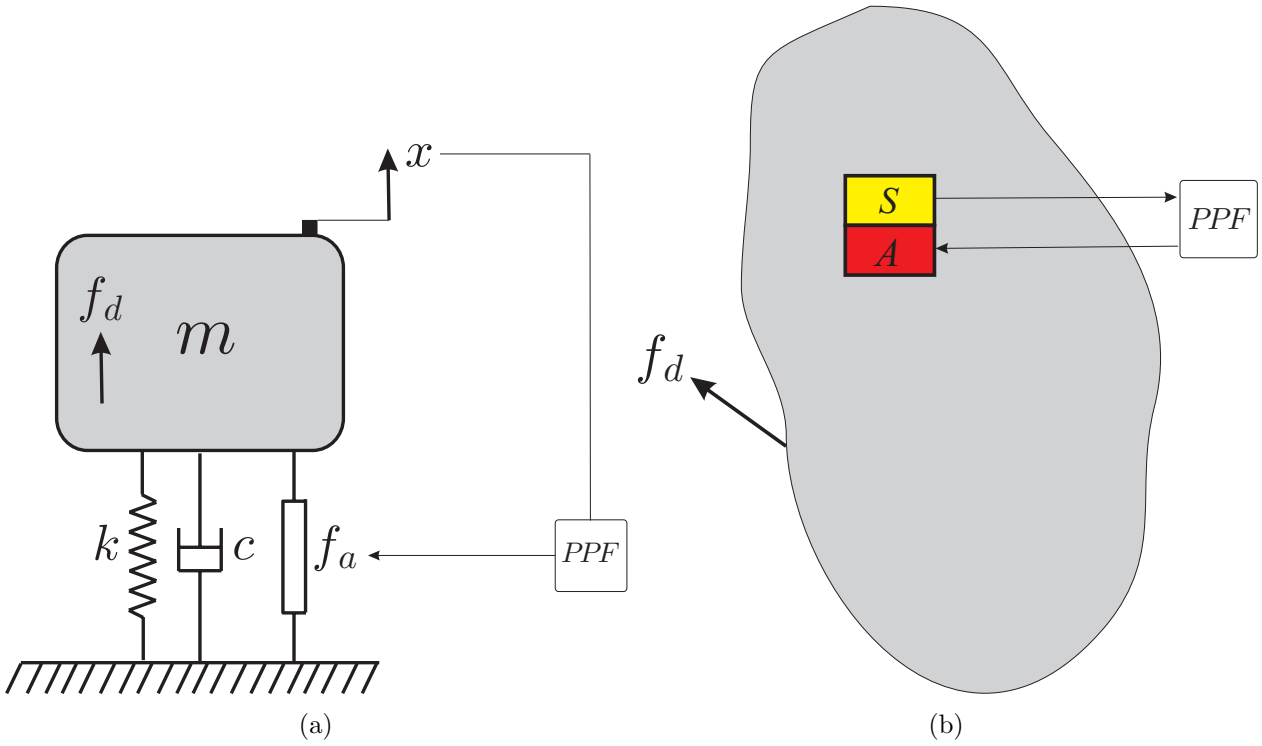

Figure 1.13: Schematic of PPF when a) displacement sensor is collocated with a reactive force actuator, and b) two piezoelectric patches are collocated.

are widely used as the actuator in practice since they possess a high value of stiffness (Figure 1.14b).

For a classical active control system, the same or a similar mechanical analogy might be obtained. The mechanical analogy contains passive elements like masses, dashpots, springs, and inerters. Note that inerter is known as a device which generates a force proportional to relative accelerations across its two terminals [31]. This can be used in mechanical designs to modify or substitute the mass of structures. The problem of realizing the mechanical designs passively comes in practical implementations because of some imperfections which will be inevitably present in the mechanical construction preventing them to act as idealized passive elements. For example, springs may have unwanted internal resonances at high frequency [32] which prevents from having high frequency roll-off in the response. Several mechanical forms have been proposed to realize inerters in practice. Two early ideas were to use rack and pinion based inerters [31] as well as ball and screw based inerters [33]. However, their performance may degrade because of the friction and backlash or elastic effect of gears or screws [34]. Hydraulic inerters [35] have been proposed although they may exhibit some nonlinear damping in addition to the inertance-like behavior [36].

Other than the mechanical analogy of an active control system, it might be possible to obtain an electrical analogy which consists of a piezoelectric or an electromagnetic transducer combined with an electrical network. A well-known example is IFF [37] which is analogous to the relaxation isolator (i.e. its mechanical analogy) as well as an electromagnetic transducer connected to a RL circuit (i.e. its electrical analogy). For piezoelectric transducers, their low capacitance may lead to a large inductance required for the electrical network [38]. The large inductance cannot be easily realized fully passively. Furthermore, high internal resistance of the coil can degrade the performance of the system for electromagnetic transducers [39].

Realizing the mechanical or the electrical systems by means of active techniques can overcome the aforementioned problems. Tuned inerter damper (TID) system is a well-know mechanical passive control system [40] which has been realized actively in [41] and [11]. In addition, direct acceleration feedback has been introduced in [42] to synthesize the inerter actively. In [27], a nonlinear spring has been added to a cantilever beam experimentally by feeding back the displacement of the structure through a cubic function. Moreover, piezoelectric shunt damping has been implemented actively by generating the signal corresponding to the RL circuit digitally [28]. Consequently, active techniques provide us a more flexible tool to shape the behavior of the possible mechanical and

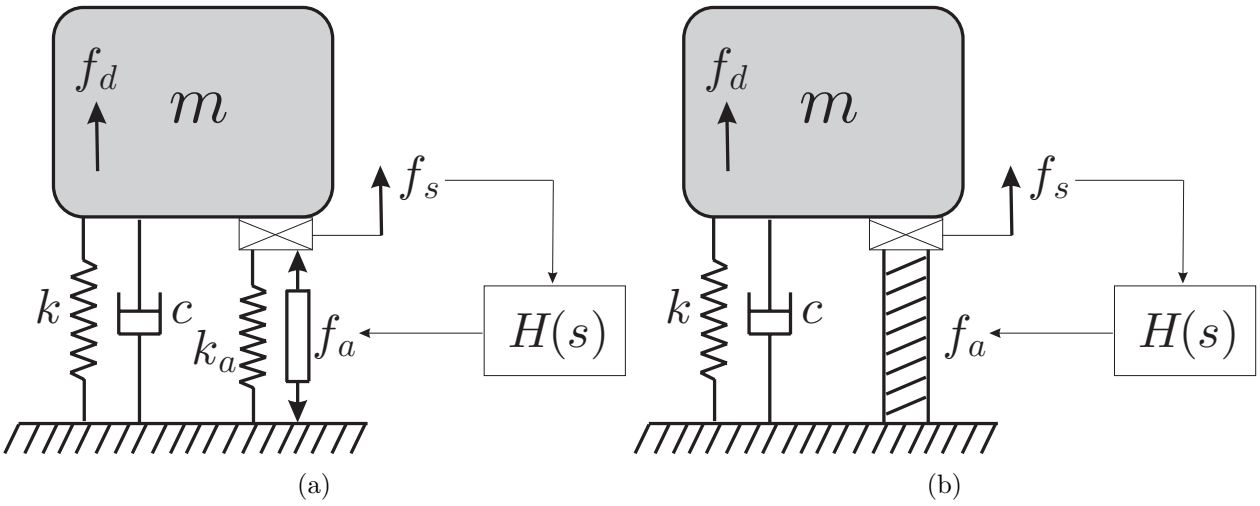

Figure 1.14: Schematic of force feedback configuration using a) a force actuator which possess an interal spring k_a, or b) piezoelectric stack as an actuator.

electrical systems. Nevertheless, its advantage comes at the expense of a power consumption as an external source is required for actuators [43].

Despite the potential of the active control systems, only a few studies have been focused on using such tools for the bladed structures. An active control system has been implemented on General Electric Aviation (GE) subscale composite fan blades using piezoelectric patches as sensors and actuators as shown in Figure 1.16. In this study [8], the control system has been inspired from the transfer function of a simple RL circuit which is used for the passive piezoelectric shunt damping. It has been reported that the advantages of this technique compared to the common passive technique are the use of an amplifier to achieve a higher actuation level, and the fact that the active control does not require an actual resistor or inductor, which can be very large-sized at low target frequencies.

Figure 1.15: General Electric Aviation (GE) subscale composite fan blades with piezoelectric patches for the implementation of active control system [8].

A number of studies has proposed active noise control (ANC) to reduce the source of engine noise induced from the large fan at the front of the engine of the modern commercial jet aircraft. Those studies have been conducted either numerically or experimentally in laboratory settings [44], [45], [46], and [9]. For example, an ANC system, designed in [47], consists of multiple microphones as sensors, multiple piezoelectric patches as actuators, and adaptive filters for controlling unit.

1.2.3 Hybrid damping

It has been shown that active control systems outperform passive techniques in terms of control performance i.e. the total damping of the closed-loop system and robustness versus plant uncertainty. However, the active systems suffer from other practical difficulties. They are mainly expensive and complex to design and realize in practice. In their design, the stability of the closed-loop system needs to be carefully checked since parametric errors in the feedback loop(s) can potentially destabilize the system. The spillover effect is among one of the most challenging issues that might spoil the active control system too. The lack of fail-safe feature in a sense that the structure is left with no additional damping if the feedback loop is distorted illustrates low reliability. Besides the complexity of such systems to be designed and developed, an external power source is required to

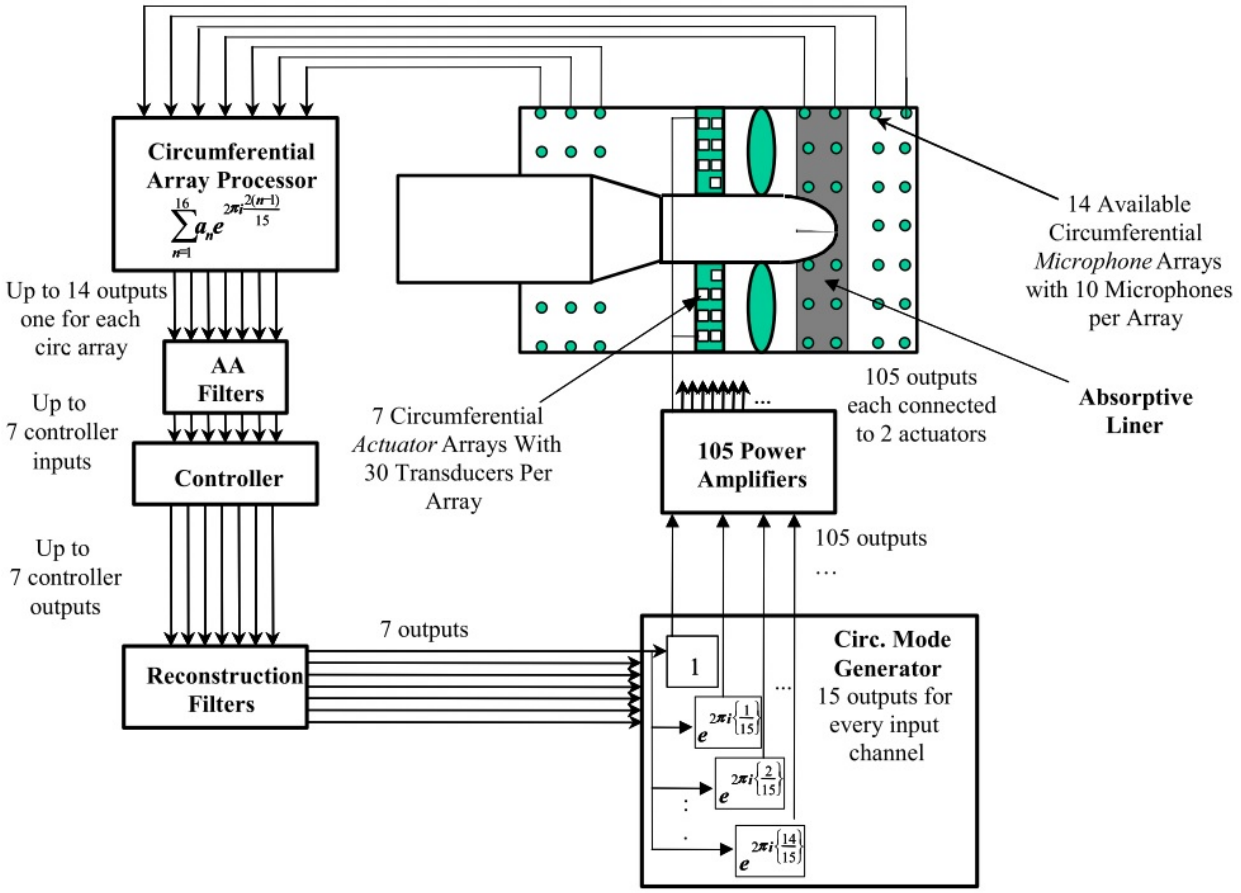

Figure 1.16: Schematic of the ANC used in [9].

derive the actuator. The power consumption plays an important role in the practical implementation of such active control systems especially for the modern industries where the energy efficiency is the key factor. Consequently, the superiority of the active control system comes at the price of high cost, high complexity, and high energy consumption of the system compared to the passive ones. Recently, a novel class of control devices aiming to possess several objectives at the same time has been introduced by combining the best of active and passive approaches. These devices are gathered under the common name of hybrid control systems. What follows is a summary of two hybrid control systems. Their objectives are threefold: (1) increase performance compared to the purely passive control system, (2) reduce energy consumption with respect to the purely active control system, and (3) ensure a fail-safe behavior which means that the device will work as the passive system when the active controller is undesirably turned off.

A class of hybrid control system known as hybrid mass damper has been introduced with the combination of TMD as the passive absorber and AMD as the active control system. According to the schematic of the HMD shown in Figure 1.17, an actuator is placed in parallel to the passive elements of TMD. The TMD adds another degree of freedom (DOF) to the structure with a resonance frequency close to that of primary structure. This make the design of the feedback loop more challenging. It has been shown that DVF is no longer effective due to the stability issue [30]. In [48], an stable active control system based on pole placement has been designed to retrofit the conventional TMD. In [49], a dual feedback loop has been preferred to increase the stability margins. A hyperstable control law has been proposed in [50] and verified experimentally in [51].

There are a number of studies on active-passive-hybrid-piezoelectric-networks (APPN). Agnes [52]

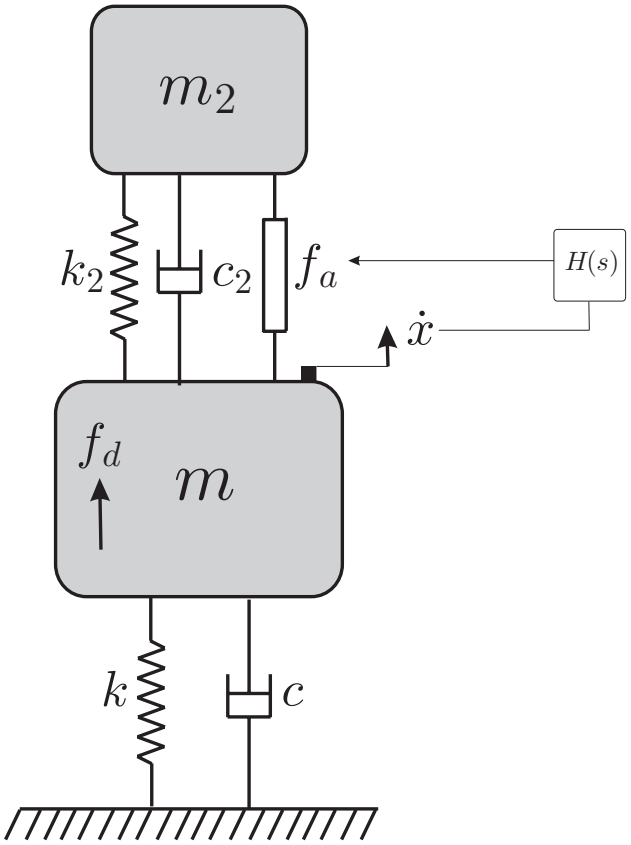

Figure 1.17: Schematic of the HMD based on the combination of TMD and AMD.

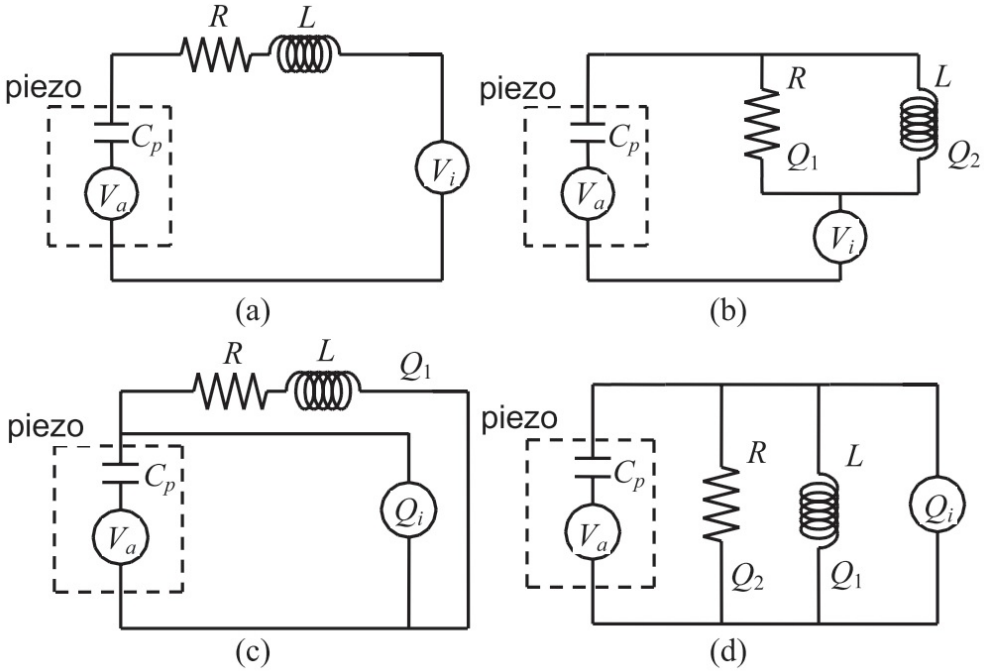

Figure 1.18: Various schematics of APPN configurations. Va: equivalent voltage generator attributed to the piezoelectric effect; Vi: voltage source; Qi: charge or current source; Q1 and Q2: charge flow in branches; Cp: piezoelectric capacitance; R: resistance; L: inductance. [10].

proposed the concept of APPN and Tsai et al. [53] presented more insight and fundamental understandings to the APPN configuration. Basically, the APPN integrates piezoelectric shunt damping with an active voltage or charge source [10]. The active voltage or charge source is made of a feedback signal coming from the sensor amplified with a control system. Various APPN configurations have been shown in Figure 1.18. It was shown in [54] that the APPN is an attractive configuration for the applications where minimizing the power consumption is critical. Morgan et al. [55] used active coupling feedback to enhance the electromechanical coupling of the transducer. They have also validated the concept experimentally on a cantilever beam in [56]. In most studies about the APPN, a collocated piezoelectric sensor has been used to generate the feedback signal. However, Li et al. [57] employed a velocity feedback control for the application of the APPN by using a displacement sensor. The optimal values of the resistance and inductance could be quite different from those of the purely passive system in the case of APPN. Therefore, Tsai el al. [58] proposed a methodology to determine the optimal values of the resistor and inductor simultaneously with the control law. Furthermore, the multiple APPN has been also investigated to control of a quadrilateral plate [59] and a ring structure [60].

1.3 Motivations and Contributions

This thesis has been realized within the Maveric project which has been funded by Service public de Wallonie (SPW). The Maveric project was with a consortium of academic and industrial partners involving Université Libre de Bruxelles, Université de Liège, and Safran Techspace Aero. The aim of the Maveric project was to design and develop an intelligent absorber to suppress the blade modes of the BluM. The absorber is supposed to meet multiple requirements such as multimodes, high control performance, high robustness to plant uncertainty, fail-safe, and low external power consumption. It is also called an intelligent absorber since it tends to be autonomous as much as possible in terms of the energy balance. To do so, an energy harvesting device has been developed as a part of the design to provide a portion of or the whole energy required for the control system.

Three different labs are directly involved in the Maveric project. The S3L group in Université de Liège is responsible to design and develop a digital shunt device. Although the piezoelectric shunt damping has been implemented on the BluM in [7], its main weakness is that the shunt damping was tuned to damp only a target resonance of the blade. The novelty of the digital shunt proposed by S3L group is to target multimode resonances of the blades in different families. The Microys group in Université de Liège is in charge of tests and realize different energy harvesting devices to maximize the extracted energy from the BluM during the rotation. And, PML group in Université Libre de Bruxelles takes the lead in the design and the development of an active-passive control system which has not been implemented before in the literature. The designed control strategies need to be validated experimentally on both academic setup and the BluM. The academic setups have been chosen to be a cantilever beam and a bladed rail structure. The cantilever beam is representative of a simple blade where its support is fully rigid. The bladed rail is seen as a simplified version of the BluM where it possess a reduced number of the blades and the shape of its support is simplified. While simple, the dynamic behavior of the bladed rail is supposed to be similar to that of the BluM.

In PML, I have been working with two other Postdoc researchers in the context of the Maveric project. My main contributions in this project as will be presented in this thesis are specified below:

- Design and develop passive electromagnetic shunt damper. The novelty is to optimize the parameters based on two different criteria i.e. maximum damping and maximum power dissipation.

- Design and develop high performance active control systems based on positive position feedback (PPF) and negative force feedback configurations. The novelty is to optimize the corresponding parameters according to different optimization methods such as maximum damping, H_2, and H_∞ criteria.
- Experimentally validate the PPF on a cantilever beam. The experimental tests are extended to evaluate the performance of the linear and the nonlinear PPF to damp the vibration of a geometric nonlinear beam.
- Compare the power consumption of the digital shunt with the PPF.
- Design and develop active-passive (hybrid) control systems using electromagnetic devices. The novelty is the new combination of active and passive control systems. In addition, the corresponding parameters are optimized based on the method of maximum damping.
- Design the bladed rail structure as an academic model. Compared to the BluM, it is supposed to have a similar dynamic behavior but geometrically simpler.
- Optimize the type and the locations of piezoelectric patches on the structures of the bladed rail and the BluM using numerical finite element method.
- Manufacture the designed bladed rail and mount the piezoelectric patches.
- Experimentally Validate the optimal locations of piezoelectric patches on the BluM.
- Implement different control strategies on the bladed rail numerically.
- Validate the numerical designed control systems on the bladed rail, experimentally.

1.4 Outlines

In this thesis, a summary of my contributions in Maveric project, as explained above, is presented in 5 chapters:

- **Chapter2** studies a passive control system. For this purpose, the electromagnetic shunt damping is considered and two optimization criteria are employed to tune the parameters of the shunt circuit. The power consumption of the system is computed when the shunt system is implemented by the digital system.
- **Chapter3** studies different active control systems. It proposes three high performance systems including resonant force feedback (RFF), positive position feedback (PPF), and nonlinear positive position feedback (NPPF). The optimal parameters will be derived and the numerical design will be validated experimentally on a cantilever beam. In addition, the PPF is compared with the digital shunt in terms of the power consumption.
- **Chapter4** studies the novel class hybrid control system. In doing so, the passive electromagnetic shunt damper is combined with either active voltage source and active current source. The optimal parameters are derived. The performance of the proposed systems is assessed in terms of the closed loop damping, and the power consumption.
- **Chapter5** studies the vibration control of the bladed structures. For this chapter:
  - The bladed rail structure is design.
  - The locations of piezoelectric patches are optimized on the BluM and the bladed rail.
  - The optimal locations of piezoelectric patches are verified experimentally.

  - Different classical control system are designed on the bladed rail numerically.
  - The designed control systems are verified experimentally on the bladed rail.

- **Chapter6** reviews the conclusions and the perspectives.

Chapter 2

Passive Electromagnetic Shunt Damper

Contents

Recently, the electromagnetic shunt damper has been proposed as a very simple and effective passive control technique. The key idea of this technique is to connect a capacitor of capacitance C and a resistor of resistance R to the electromagnetic transducer of inductance L to form a resonant RLC circuit. The absorber dissipates the vibrational energy by the resistor and its resonance is tuned close to the resonance of the primary system thanks to the tuned capacitor [61]. Many optimization methods have been proposed to optimize the parameters R and C. de Marneffe [62] optimized the parameters through the method of maximum damping and H_∞ minimization when the system is under base excitation. He has also compared the resonant RLC shunt with a resistive shunt. Inoue et al. [63] derived the optimal parameters by using the fixed point theory which was initially proposed by Den Hartog for the mechanical vibration absorber [64]. In [65], the optimal parameters have been obtained analytically using both the H_2 and H_∞ optimization methods which consist in minimizing the root-mean-square (RMS) vibration under random excitation and the peak amplitude in the frequency domain, respectively. Moreover, Zhu et al. [66] studied the analogy between the electromagnetic shunt damper and a tuned mass damper (TMD). Then, the optimal parameters of an electromagnetic shunt have been adapted from the optimal parameters of the TMD (obtained by Ormondroyd and Den Hartog [67]) by using an equivalent mass, stiffness and damping coefficient for the electromagnetic shunt damper. The main shortcoming of this method is that the optimal parameters can be used only when the equivalent mass ratio is small enough because a full dynamic analogy does not exist.

While simple, the realization of the RC circuit may be challenging. This is because, depending on the parameters of the system, the required capacitance can be impractically large and the required resistance can be much smaller than the internal resistance of the coil. The synthetic impedance is proposed as an alternative solution. The synthetic impedance is realized by the combination of a digital processing unit with a current source. Through the digital processing unit, the voltage of the device can be sensed first. Then, it is amplified with a filter, which emulates the admittance of the circuit, to generate the control voltage. Thanks to the external current source,

the control voltage turns to the control current. Clearly, this configuration makes a flexible system to realize any arbitrary impedance only by changing the filter. The advantage of the digital shunt compared to the passive shunt comes at the expense of the external power source required for the synthetic impedance. In particular, the external power is required to activate operational amplifiers (OpAmps) in the system.

In this chapter, first, two optimization techniques, including the method of maximum damping and the method of maximum power dissipation, are used to tune the parameters of the passive electromagnetic shunt damper. Then, the digital electromagnetic shunt is studied in terms of the power consumption of the system. For this purpose, the power consumption of the OpAmp is derived when it is connected to the electromagnetic transducer. Finally, the power consumption of the OpAmp is computed when the digital shunt is applied on the electromagnetic transducer.

2.1 Mathematical modeling

Figure 2.1 shows the system under consideration. It is a single-degree-of-freedom (SDOF) oscillator with a mass m, spring k and an electromagnetic device connected to a resistor of resistance R_s and a capacitor of capacitance C_s. The system is considered as an undamped SDOF when the electromagnetic transducer is in open-circuit condition. The system is excited by a disturbance force f_d, and the impulse response of the SDOF system is of interest. The electromagnetic device which is made of a permanent magnet and a coil has the following parameters: coupling constant T, coil inductance L_c and coil resistance R_c. It can generate a force f_a which is proportional to the current I_t flowing inside the coil with a coupling coefficient T_i. In addition, the voltage across the transducer V is proportional to the velocity of the mass $\dot{x}$ with a coupling coefficient T_e. Both constants are equal to each other ($T_i = T_e = T$) thanks to a perfect transmission between the electrical and the mechanical energy. The coupling constant is equal to the product of the magnetic flux density B and the length of the coil seen by the magnetic flux [25], i.e. $T = 2\pi nrB$,

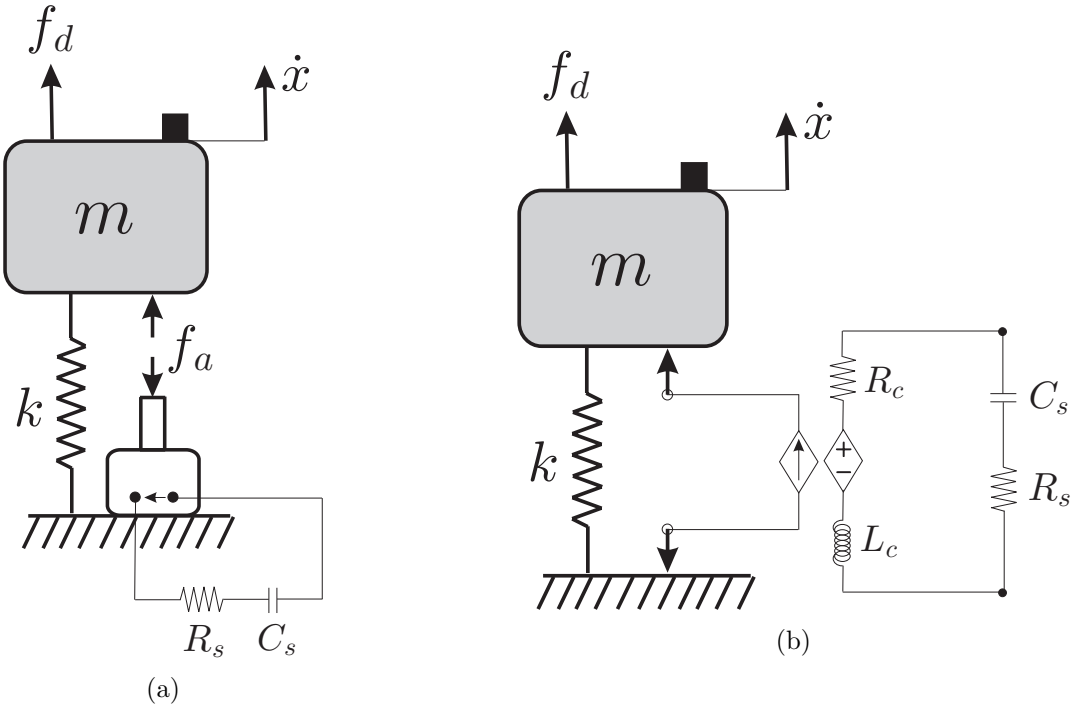

Figure 2.1: SDOF oscillator combined with the electromagnetic shunt damper. (a) Mechanical model and (b) Electrical equivalent model of the transducer.

where n and r are the number of turns in the coil and its radius (considering a cylindrical device), respectively. The governing equations of motion are written as:

$$m\ddot{x} + kx = f_d + f_a \tag{2.1a}$$
$$f_a = -TI_t = -T\dot{q} \tag{2.1b}$$
$$V = L\ddot{q} + R\dot{q} + \frac{1}{C}q = T\dot{x} \tag{2.1c}$$

where $L = L_c$, $C = C_s$, q is the charge flowing inside the coil. For the sake of simplicity, R is considered as the total resistance of the circuit i.e. $R = R_c + R_s$ (Figure 2.1b). The loop gain transfer function is now:

$$L(s) = A(s) \times B(s) = \frac{s}{m * s^2 + k} \times \frac{T^2 s}{Ls^2 + Rs + \frac{1}{C}} \tag{2.2}$$

where A(s) and B(s) are the sensor-actuator open-loop transfer function and the transfer function of the controller, respectively.
The Eq. (2.1) can be normalized with respect to the dimensionless time $\tau = \omega_0 t$ where $\omega_0 = \sqrt{k/m}$ as below:

$$x_1'' + x_1 = f - \beta_1 \omega_0 x_2' \tag{2.3a}$$
$$x_2'' + 2\xi\alpha x_2' + \alpha^2 x_2 = \beta_2/\omega_0 x_1' \tag{2.3b}$$

where the normalized parameters are:

$$\begin{gathered}\tau = \omega_0 t,\ x_1(\tau) = x(t),\ x_2(\tau) = q(t),\ \Omega = \omega/\omega_0,\ f = \frac{1}{k}f_d,\ \beta_1 = \frac{T}{k} \\ \beta_2 = \frac{T}{L},\ \beta = \beta_1\beta_2,\ \omega_f = \frac{1}{\sqrt{LC}},\ \alpha = \frac{\omega_f}{\omega_0},\ \xi = \frac{R}{2}\sqrt{\frac{C}{L}}\end{gathered} \tag{2.4}$$

The transfer function of the system from the normalized external force f to the normalized velocity of the mass $\dot{x}_1$ is then given by:

$$\frac{\dot{x}_1}{f} = \frac{s(s^2 + 2\xi\alpha s + \alpha^2)}{(s^2+1)(s^2 + 2\xi\alpha s + \alpha^2) + \beta s^2} \tag{2.5}$$

where $s = j\Omega$ is the Laplace variable. In the remaining of this section, the following numerical values are used: m=1kg, $k = 10^4$N/m, T=1N/Amp and $L = L_c = 10^{-3}$H. It should be mentioned that the resistance of the coil R_c is already included in R. According to Eq. (2.5), the passive control system adds another DOF to the system which makes the closed-loop response have two pairs.

2.2 Optimization based on maximum damping method

In this section, the method of maximum damping is used to optimized the parameters of the passive elements. The root-locus of the system (Eq. (2.2)) is shown in Figure 2.2 for different values of the resistance R and the capacitance C. Basically, the locus consists of two loops starting from the pole of the primary system (P_0) and the pole of the resonant shunt (P_1 or P_2 or P_3), respectively. One of the loop goes to the origin and the other one goes to infinity. Considering the method of maximum damping, it can be observed that the maximum closed-loop damping can be realized when both loops are intersecting at one point (Figure 2.2c). In other words, two closed-loop poles (■) are merged together. It is worth pointing out that the values of the R and C are taken arbitrarily to observe the different possible root locus curves. Considering the value of the resistance and capacitance corresponding to Figure 2.2c as the optimum ones, Figure 2.2a shows a typical

root locus of the system when a higher value of the resistance or a lower value of the capacitance is taken. For a lower value of the resistance or a higher value of the capacitance, the typical root locus of the system is shown in Figure 2.2b.

The normalized transfer function, when two closed-loop poles are merged, can be simplified as:

$$\frac{\dot{x}_1}{f} = \frac{s(s^2 + 2\xi\alpha s + \alpha^2)}{(s^2 + 2\eta\gamma s + \gamma^2)^2} \tag{2.6}$$

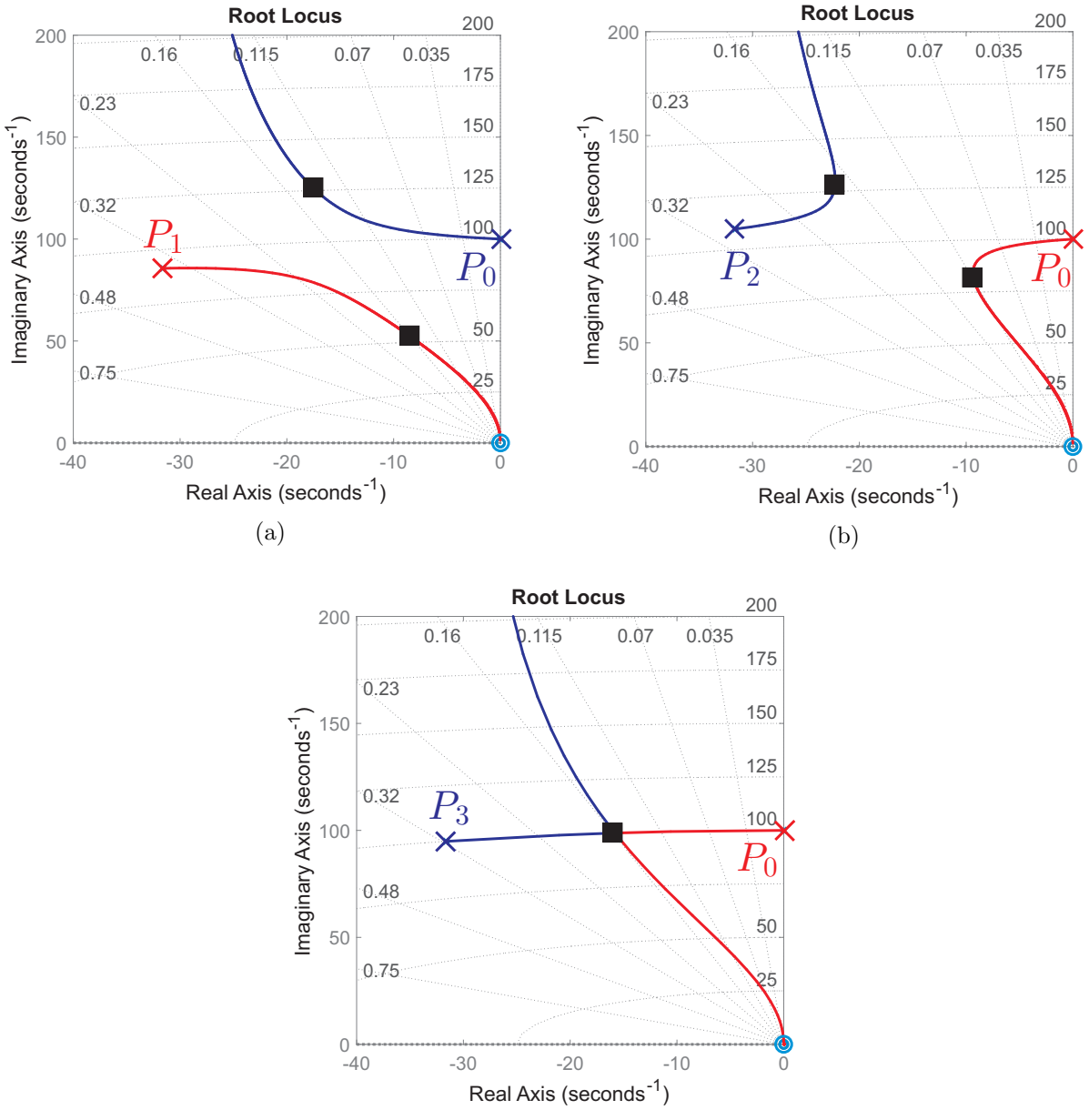

Figure 2.2: Root-locus of the system shunted with the passive circuit and different values of the resistance R and capacitance C (P_0: pole of the primary system; P_1: pole of the controller using a higher value of R or a lower value of C; P_2: pole of the controller using a lower value of R or a higher value of C; P_3: pole of the controller using optimum values of the resistance and capacitance; ◯: zero of the controller; ■: pole of the closed-loop system tuned based on the method of maximum damping)

where η is the damping ratio, ω_c, and $\gamma = \omega_c/\omega_0$ are the resonance frequency and the normalized resonance frequency of the closed-loop response function, respectively. By matching the polynomial coefficients of the denominators of Eq. (2.5) and Eq. (2.6), the set of equations can be obtained as below:

$$4\eta\gamma = 2\xi\alpha \tag{2.7a}$$
$$4\eta^2\gamma^2 + 2\gamma^2 = \alpha^2 + \beta + 1 \tag{2.7b}$$
$$4\eta\gamma^3 = 2\xi\alpha \tag{2.7c}$$
$$\gamma^4 = \alpha^2 \tag{2.7d}$$

From Eqs. (2.7a), (2.7c) and (2.7d), it can be concluded that

$$\gamma_{opt} = \alpha_{opt} = 1 \tag{2.8}$$

which means that the optimal frequency of the circuit and the closed-loop resonance frequency of the system are equal to the resonance frequency of the primary system. Considering the above equation, η can be obtained as a function of ξ from Eq. (2.7a) ($\eta = \frac{1}{2}\xi$). Substituting this equation and Eq. (2.8) to Eq. (2.7b) yields:

$$\xi_{opt} = \sqrt{\beta} \tag{2.9}$$

As a consequence, the optimal parameters of resistance and capacitance can be obtained as:

$$C_{opt} = \frac{1}{L\omega_0^2} \tag{2.10a}$$
$$R_{opt} = \frac{2T}{\sqrt{kC_{opt}}} \tag{2.10b}$$

Figure 2.3 shows the closed-loop damping ratio of the system (Eq. (2.5)) against the variation of the resistance R and capacitance C, individually, normalized with respect to their optimal values. Note that one parameter is kept constant when the other one is varied. As it can be seen, the only values which can realize the maximum damping are only the optimal values.
Figure 2.4a shows the frequency response for five different values of the resistance R when the capacitance C is set to its optimal value and kept constant. All the curves are intersecting at two points which are called fixed-points. For $R < R_{opt}$, two resonances appear in the vicinity of the resonance frequency of the primary system. The controller is no longer effective in the terms of

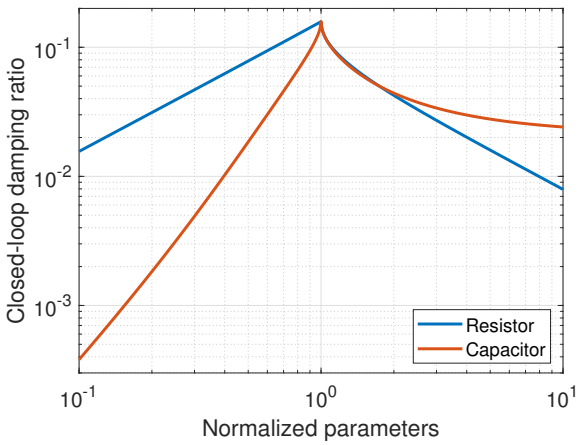

Figure 2.3: Closed-loop damping ratio of the system against the variation of the shunt elements i.e. resistance R and capacitance C normalized with respect to their optimal values

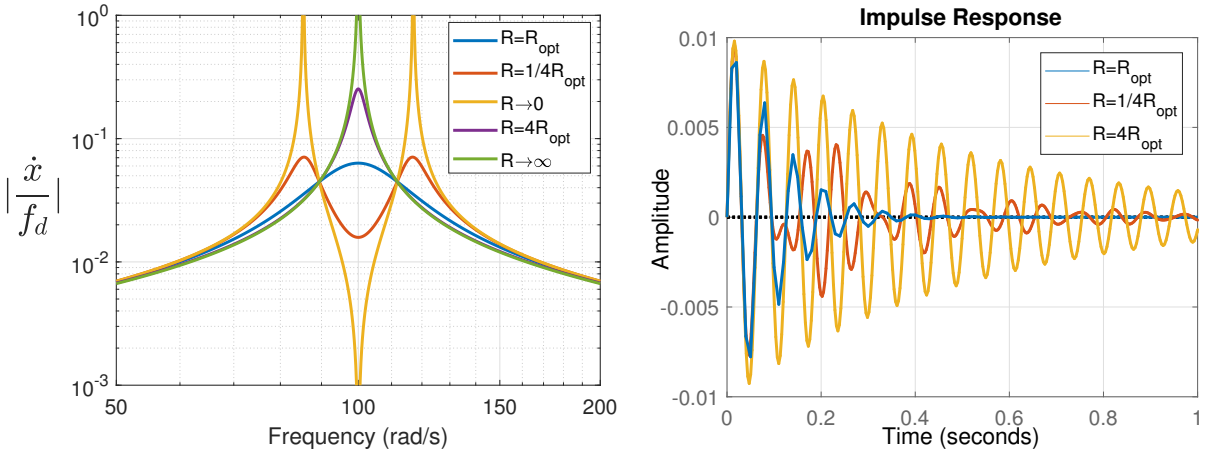

(a) (b)

Figure 2.4: For the attached passive RC circuit, (a) frequency response as well as (b) the impulse response for different values of R

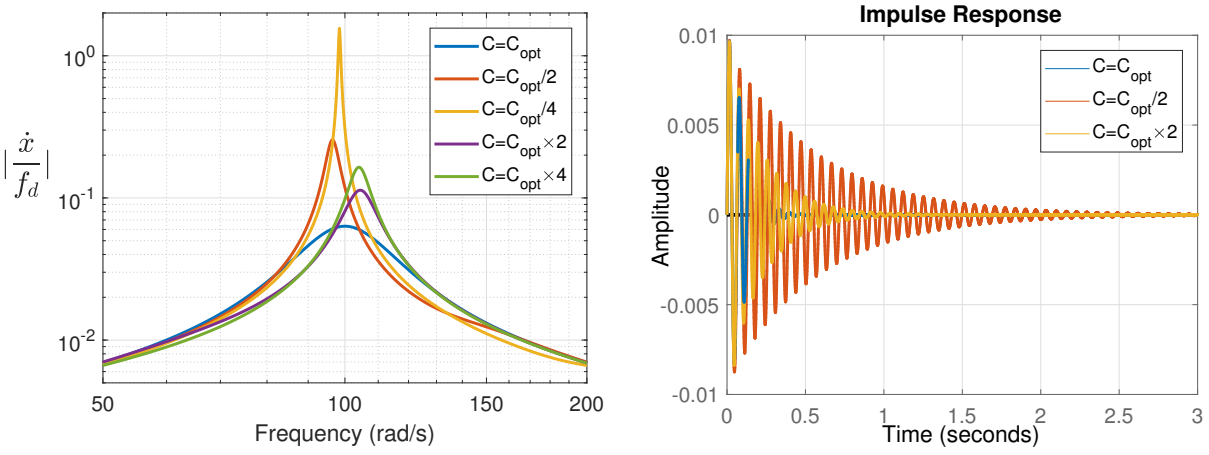

(a) (b)

Figure 2.5: For the attached passive RC circuit, (a) frequency response as well as (b) the impulse response for different values of C

amplitude reduction when $R \to 0$. In addition, the performance degradation can also be observed when $R > R_{opt}$. Especially when $R \to \infty$, the controlled system acts like a primary system with no additional damping. By using the method of maximum damping to optimize the parameters of the controller, the settling time of the transient response of the system to the impulse disturbance should be minimized. To verify this fact, the impulse response in the time domain is also shown in Figure 2.4b for three different values of R. As it can be seen, the minimum settling time can be achieved by considering the designed optimal value of R obtained in Eq. (2.10b).

Figure 2.5a shows the frequency response for five different values of the capacitance C. Note that the value of R is set to its optimum and kept constant. The evidence of the performance degradation can be seen by a deviation from the optimal capacitance C_{opt}. It is wroth pointing out that the amplitude of the resonance exhibits one peak when the parameters are optimally tuned according to Eq. (2.10). However, mistuning leads to the increase of one peak accompanied by the reduction of the other one. Figure 2.5b also demonstrates the impulse response of the system for three different values of the capacitance C. Minimum settling time occurs only when the capaci-

tance is set to its optimum.

Consequently, the passive shunt system as a frequency dependent control system is less robust to resonance uncertainty. Some studies have introduced different strategies to online adapt the parameters of the passive shunt to ensure the tuned frequency of the vibration absorber tracks the excitation frequency. More details are presented in [68, 69]. An alternative solution to online adaptation is to employ a broadband vibration absorber such that the system can tolerate a high level uncertainty, which is of interest in the present work. In the next sections, we propose two different hybrid control systems based on active voltage and current sources. One of the advantage of the proposed hybrid system is to make the system robust to resonance uncertainty.

2.3 Optimization based on maximum power dissipation

In this section, the parameters of the passive shunt are tuned based on maximum power absorption. The power can be derived both in time and frequency domains. However, according to the Parseval's theorem, the root mean square value (RMS) of a signal in time domain is equal to the RMS value of the signal in frequency domain [70]. This means that the RMS value of the power in time and frequency domains are the same. In Appendix A, the Parseval's theorem is proved mathematically for the power and an example is presented to illustrate the theory. In the following section, we use the power in frequency domain for the optimization process. The power which flows at the interface of the structure and the actuator device can be written in frequency domain $P(j\omega)$ as [71]:

$$P(j\omega) = f_a(j\omega) \times v^*(j\omega) \tag{2.11}$$

where superscript $*$ shows the complex conjugate transpose and $v(j\omega) == \dot{x}(j\omega)$ is the velocity of the mass in frequency domain, respectively. According to the set of Eq. 2.1, the actuator force $f_a(j\omega)$ and the velocity of the mass $v(j\omega)$ can be obtained as follow:

$$f_a(j\omega) = \frac{T^2 j\omega}{-L\omega^2 + Rj\omega + \frac{1}{C}} G(j\omega) f_d(j\omega) \tag{2.12}$$

and

$$v(j\omega) = G(j\omega) f_d(j\omega) \tag{2.13}$$

where $G(j\omega)$ is:

$$G(j\omega) = \frac{v(j\omega)}{f_d(j\omega)} = \frac{j\omega(-L\omega^2 + Rj\omega + \frac{1}{C})}{(-m\omega^2 + cj\omega + k)(-L\omega^2 + Rj\omega + \frac{1}{C}) - T^2\omega^2} \tag{2.14}$$

By substituting Eqs. (2.12)-(2.14) into Eq. 2.11, the power can be re-written in frequency domain after some manipulations as:

$$P(j\omega) = T^2 j\omega^3 (-L\omega^2 - Rj\omega + \frac{1}{C}) \cdot \left| \frac{1}{(-m\omega^2 + cj\omega + k)(-L\omega^2 + Rj\omega + \frac{1}{C}) - T^2\omega^2} \right|^2 \cdot |f_d(j\omega)|^2 \tag{2.15}$$

The real part of $P(j\omega)$ is called the active power which corresponds to the dissipative behavior and the imaginary part is named the reactive power which corresponds to the energy exchanged between the device and the structure. The average active power P_{ac} can be written as:

$$P_{ac} = \frac{1}{2}\Re(P(j\omega)) = \frac{1}{2} \left| \frac{T\sqrt{R}\omega^2}{(-m\omega^2 + cj\omega + k)(-L\omega^2 + Rj\omega + \frac{1}{C}) - T^2\omega^2} \right|^2 = |H(j\omega)|^2 \cdot |f_d(j\omega)|^2 \tag{2.16}$$

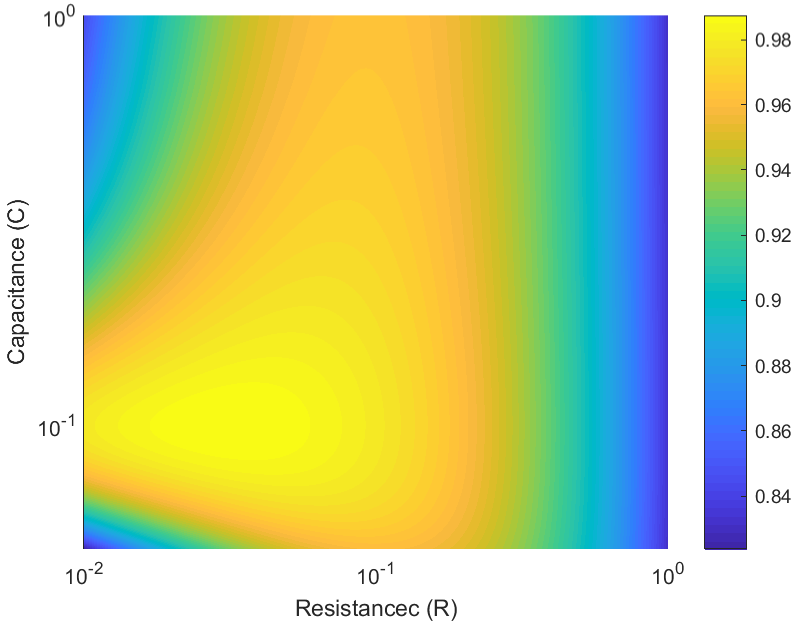

Figure 2.6: The normalized means square value of the active power I against the large variation of the resistance R and capacitance C

The mean square value of the active power can be written as:

$$E[|P_{ac}|] = \int_{-\infty}^{\infty} |H(j\omega)|^2 \, S_d(\omega) d\omega \tag{2.17}$$

where $E[\,]$ denotes the expectation value. $S_d(\omega)$ is the power spectral density of the input disturbance force which can be calculated as:

$$S_d(\omega) = |f_d(j\omega)|^2 \tag{2.18}$$

For the case of white noise excitation force, the $S_d(\omega)$ is constant as a function of frequency ($S_d(\omega) = S_d$). Therefore, the mean square value of the power can be simplified as:

$$E[|P_{ac}|] = S_d \int_{-\infty}^{\infty} |H(j\omega)|^2 \, d\omega \tag{2.19}$$

The normalized mean square value I is defined to represent the ratio of the active power to the excitation force with a uniform spectrum density like:

$$I = \frac{E[|P_{ac}|]}{S_d} = \int_{-\infty}^{\infty} |P_{ac}| \, d\omega = \int_{-\infty}^{\infty} |H(j\omega)|^2 \, d\omega \tag{2.20}$$

Substituting Eq. (2.18) in to Eq. (2.20) and using the analytical expression in [72]:

$$I = \frac{(Rk + \frac{c}{C})T^2 R}{(Rk + \frac{c}{C})(-(Rk + \frac{c}{C})mL + (Lk + \frac{m}{C} + T^2 + cR)(Lc + Rm)) - k\frac{(Lc+Rm)^2}{C}} \tag{2.21}$$

To maximize the total power absorbed by the electromagnetic shunt damper, the following conditions have to be satisfied:

$$\frac{dI}{dR} = 0 \tag{2.22a}$$

$$\frac{dI}{dC} = 0 \tag{2.22b}$$

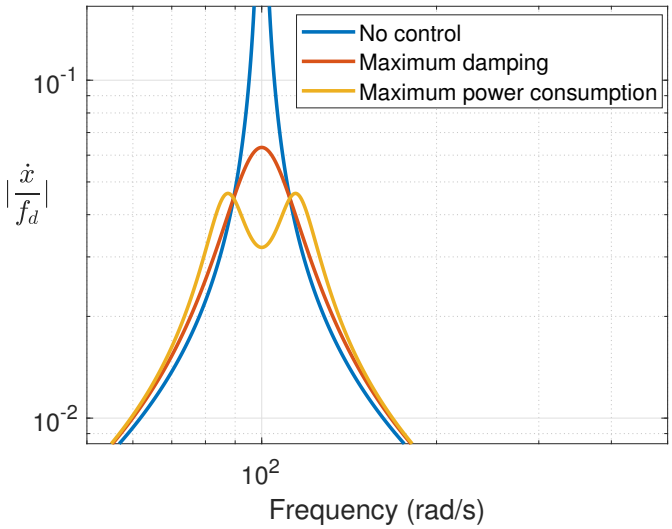

Figure 2.7: Frequency response function for control off and on

which leads to:

$$C_{opt} = \frac{m}{kL} \tag{2.23a}$$

$$R_{opt} = T\sqrt{\frac{L}{m}} \tag{2.23b}$$

Interestingly, the optimal capacitance is exactly equal to the optimal capacitance obtained according to the method of maximum damping. This means that no matter which optimization is employed, the electrical network is resonating at the same frequency which is equal to the resonance frequency of the primary system. On the other hand, this optimal value of the resistance is two times lower than of the optimal resistance which is obtained based on the method of maximum damping.

Figure 2.6 show the normalized mean square value I as a function of resistance R and capacitance C. One sees that only the optimal parameters can maximize the power absorption. Furthermore, Figure 2.7 shows the frequency response function from the disturbance force to the velocity of the mass. It compares the response for both control off and on.

2.4 Digital electromagnetic shunt damper

For the system under consideration shown in Figure 2.1, the optimal value of the capacitance is 100mF and the optimal value of the resistance are 63.2mΩ, and 31.6mΩ according to the method of maximum damping, and the method of maximum power dissipation, respectively. In the market, it is almost impossible to find the capacitor and the resistor with the right impedance. Therefore, it is proposed to realize the damping system by means of digital system. In this case, the voltage of the electromagnetic device needs to be measured and thanks to an operational amplifier (OpAmp), a current proportional to the current flowing inside the virtual shunt circuit is generated and sent to the actuator. Since the OpAmps requires an external power for its operation, the digital shunt can be seen as an active control system. Therefore, the power which is consumed by the OpAmp becomes an important key. In the following section, we will study the power budget for an OpAmp.

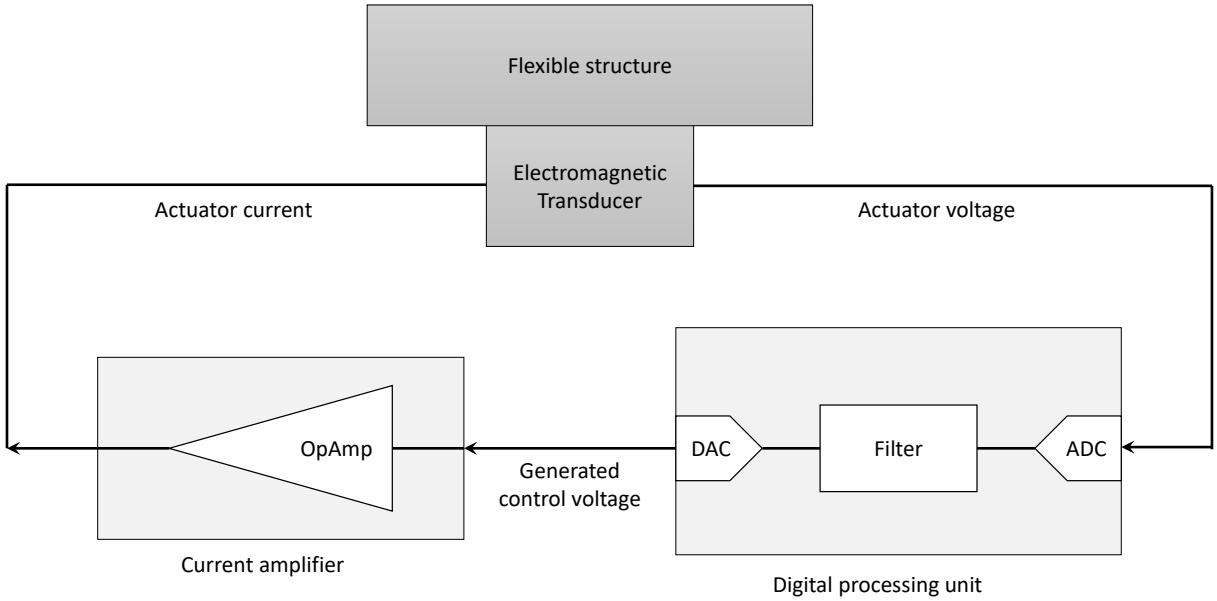

Figure 2.8: Schematic of the synthetic impedance.

2.4.1 Power consumption for an OpAmp

The schematic of the OpAmp is shown in Figure 2.9. V^+ and V^- are the input voltages. V_{out} is the output voltage. V_{CC} and V_{EE} are the power supply voltages. Figure 2.10 shows the general use of the OpAmp connected to the electromagnetic transducer as an actuator. From the figure, one sees that a power is generated by the power supply P_{supply} and distributed to the OpAmp and the load which is the transducer in this case. Therefore, the balance of the the total power reads:

$$P_{supply} = P_{OpAmp} + P_{load} \tag{2.24}$$

where P_{OpAmp} and P_{load} are the power of the OpAmp and the power of the load, respectively. We are interested in the power dissipation or consumption which causes self heating. There are two main sources of the power consumption by the OpAmp. The first one is caused by the quiescent current I_Q which OpAmp requires for the internal operation in the no-load or steady-state situation. The

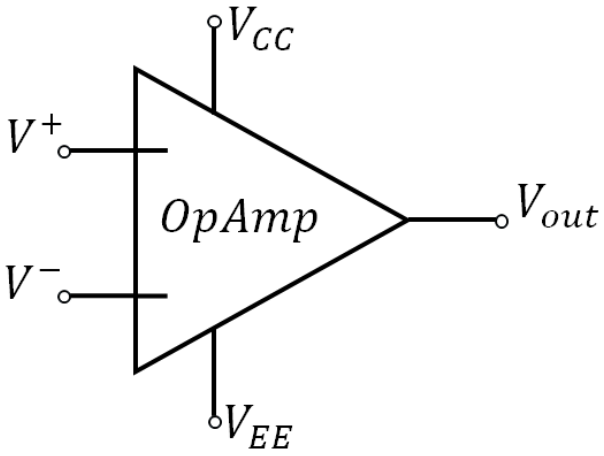

Figure 2.9: Schematic of the OpAmp.

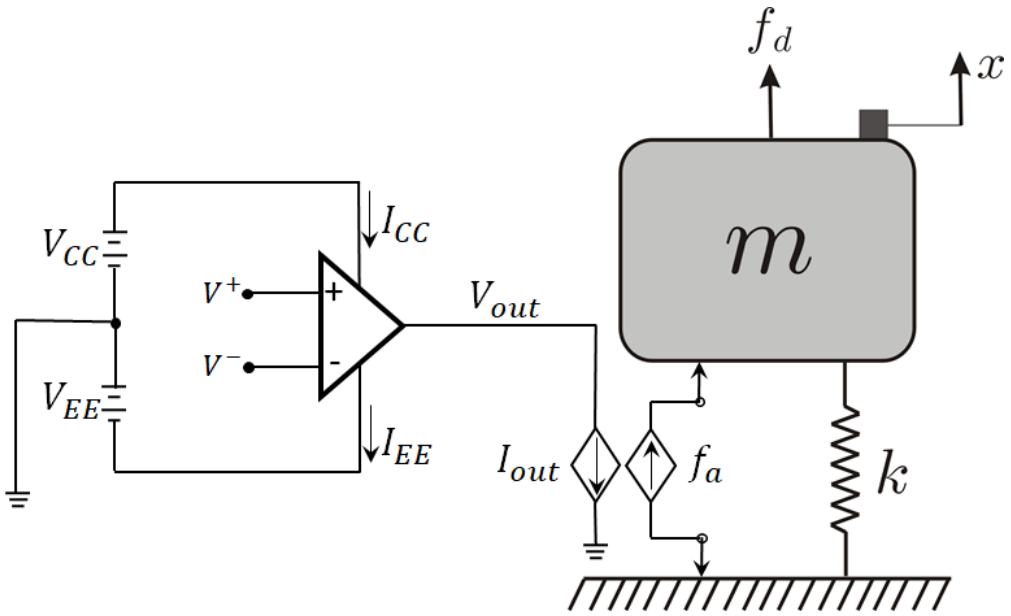

Figure 2.10: Schematic of the OpAmp connected to the electromagnetic transducer as an actuator.

quiescent current is equal to the current flowing inside the terminal of the supply ($I_Q = I_{EE} = I_{CC}$). Therefore, the corresponding power consumption can be obtained by the product of the quiescent current I_Q flowing from V_{CC} terminal to the V_{EE} terminal and the difference in potentials between the two terminals as:

$$P_Q = I_Q \times (V_{CC} - V_{EE}) \tag{2.25}$$

This power is always dissipative as long as the supply power is applied on the OpAmp even when there is no output current ($I_{out} = 0$). The second source of the power consumption is caused by the output current I_{out} which flows inside the transducer. Generally, the output current can be modeled as the source and sink. In the case of output source current, the current is flowing from V_{CC} to V_{out}. Thus, the power of the load can be written as:

$$P_{out} = P_{source} = I_{source} \times (V_{CC} - V_{out}) \tag{2.26}$$

And for the case of the output sink current, the current is flowing from V_{out} to V_{EE}. Subsequently, the power of the load is:

$$P_{out} = P_{sink} = I_{sink} \times (V_{out} - V_{EE}) \tag{2.27}$$

Therefore, the balance of the power only for the OpAmp can be considered as the summation of the quiescent power and the output power as:

$$P_{OpAmp} = P_Q + P_{source} = 2I_Q V_{CC} + I_{source} \times (V_{CC} - V_{out}) \tag{2.28a}$$
$$P_{OpAmp} = P_Q + P_{sink} = 2I_Q V_{EE} + I_{sink} \times (V_{out} - V_{EE}) \tag{2.28b}$$

It is possible to define the source I_{source} and the sink current I_{sink} as the function of the output current I_{out} based on its sign as:

$$if \quad I_{out} > 0 \rightarrow I_{source} = I_{out} \tag{2.29a}$$
$$if \quad I_{out} < 0 \rightarrow I_{sink} = -I_{out} \tag{2.29b}$$

By considering $V_{CC} = -V_{EE}$ and the above equations, the power of OpAmp can be re-written as:

$$P_{OpAmp} = 2I_Q V_{CC} + I_{out} \times (V_{CC} - V_{out}), \quad I_{out} > 0 \tag{2.30a}$$
$$P_{OpAmp} = 2I_Q V_{CC} - I_{out} \times (V_{out} + V_{CC}), \quad I_{out} < 0 \tag{2.30b}$$

After some manipulations, the above equation can be simplified as:

$$P_{OpAmp} = 2I_Q V_{CC} + |I_{out}|V_{CC} - V_{out}I_{out} \tag{2.31}$$

Interestingly, the above equation is align with the Eq. (2.24). The summation of first two terms in the right hand side of the equation shows the power generated by the power supply P_{supply} and the last term is equal to the power of the load $P_{load} = P_{out}$. The first term corresponding to quiescent power is always constant. However, different control strategies mainly changes the next two terms. From Eq. (2.1), the voltage and current can be written proportional to the velocity of the mass and the actuator force, respectively. Therefore, the output power of the amplifier can be obtained as:

$$P_{OpAmp} = 2I_Q V_{CC} + \frac{|f_a|}{T}V_{CC} + \dot{x}f_a \tag{2.32}$$

Depending on the type of controller, f_a and $\dot{x}$ are different, and subsequently, the instantaneous power could have only real part or both real and imaginary parts. The real part of this power is called the active power P_{ac} and the imaginary part is called the reactive power P_{re}. The active power assesses the dissipative behavior and the reactive power shows the difference between the kinetic and the potential energy. The active power is said dissipative if it has a positive value. Note that the reactive power exchanges between the transducer and the power supply and does not represent the dissipation aspect. In this study, we only interested in the dissipated power which causes self-heating. The first two terms are always positive real values. Therefore, by taking the half of the real part of the last term, the active power of the OpAmp can be computed in frequency domain as follows:

$$P_{OpAmp} = 2I_Q V_{CC} + \frac{|f_a(j\omega)|}{T}V_{CC} + \frac{1}{2}\Re(f_a(j\omega)\dot{x}(j\omega)) \tag{2.33}$$

In the following section, the power dissipation of the OpAmp, when the electromagnetic transducer is shunted with RC elements, is studied. In Section 2.3, $f_a(j\omega)$ and $\dot{x}(j\omega)$ has been already derived and they are not shown here again. According to the datasheet of the used OpAmp, the quiescent current is $I_Q = 3.2$mA and the voltage of the power supply is kept constant at $V_{CC} = 10$V. The active power of the OpAmp is presented in Figure 2.11 when the shunt elements are tuned according to the method of maximum damping. Clearly, the active power always possess a positive value in the whole frequency range which shows the system is dissipative. It can be seen that the maximum power dissipation appears around the resonant frequency due to the application of resonant shunt system. Subsequently, far from the resonance frequency, the amplitude of the power is only dominated by the quiescent power which is equal to 0.064Nm/s.

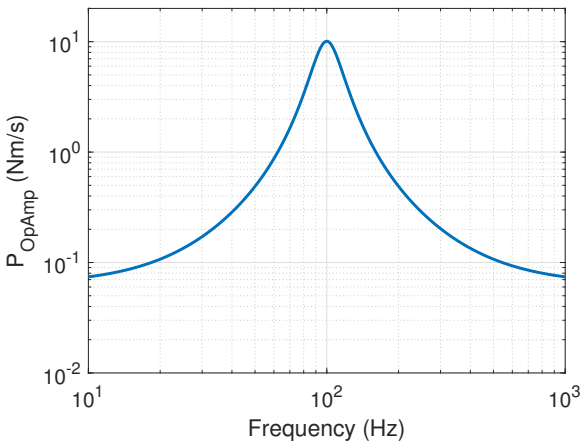

Figure 2.11: Power dissipation of the electromagnetic transducer when it is shunted with RC elements.

2.5 Conclusions

The passive shunt damper has been studied in this chapter. The RC shunt has been used in series to an electromagnetic transducer with an inductance L to make RLC circuit. The parameters of resistance and capacitance have been optimized based on two different criteria i.e. the method of maximum damping and the method of maximum power absorption.

It has been also shown that it is not always possible to realize the passive shunt elements including the resistor, and the capacitor in practice. A well-known alternative solution has been introduce to implement the shunt technique by means of the digital system where an operational amplifier (OpAmp) is required. Therefore, the digital shunt can be seen as an active control system. Because an external power source is required for the operation of the OpAmp, its power consumption has been derived and computed when the digital system is applied.

Chapter 3

Active Vibration Control

Contents

From Chapter 2, it can be concluded that the optimal closed-loop damping is $\eta_{opt} = T/(2\sqrt{kL})$ using electromagnetic shunt damper. This shows that the stiffness of the structure k as well as the coupling constant T and the inductance of the transducer L limit the maximum achievable damping obtained by the passive control system. Although the use of a negative inductance has been proposed to artificially reduce the inductance of the circuit and subsequently increase the maximum achievable damping ratio, the closed-loop system is conditionally stable [73, 74, 75].

Another limitation was to realize the RC circuit fully passively for some systems since the required impedance of the shunt elements was impossible to obtain in practice. Therefore, the shunt system has been implemented by means of the digital system. However, the price to pay was the required external power which consumes by the operational amplifier (OpAmp). In fact, the digital shunt can be seen as an active control system when the electromagnetic transducer is used as both sensor and actuator. Using an individual sensor combined with the electromagnetic transducer or the piezoelectric transducer as an actuator makes a configuration of an active control system which is able to improve the control performance. This chapter studies the use of different active control systems and evaluates the control performance in terms of the vibration attenuation, the stability, and the robustness to resonance uncertainty.

The choice of the active control configuration is highly dependent on the type of sensor and actuator. In this thesis, we are interested in two configurations. They include the force sensor collocated

with the force actuator as well as the displacement sensor collocated with the reactive fore actuator. In Section 3.1, the first configuration i.e. force sensor collocated with the force actuator is studied. In Sections 3.2 and 3.3, the second configuration i.e. the displacement sensor collocated with the reactive force actuator is studied for linear and nonlinear vibration, respectively.

3.1 Resonant force feedback control system

Integral-force-feedback (IFF) is a popular control law in active vibration damping of mechanical system when a force sensor is collocated with a force actuator. While it is simple, robust to resonance uncertainty and stable for any feedback gains, its efficiency is limited by system's parameters and in particular the stiffness ratio between the structure and the actuator. Therefore, the control authority decreases at high frequency resonances or when the actuator is weakly coupled to the structure. It has been shown that the use of double integrator with a real zero, named α-controller, can improve the control authority of a target mode. However, this technique like IFF cannot be easily implemented in practice because of low frequency saturation issue induced by significantly amplifying the low frequency content during the integration process.. The following section proposes a new control law, named resonant-force-feedback (RFF), based on a second order low pass filter to damp a target mode resonance. The mechanical analogy of the proposed system is first derived and then the parameters of RFF are optimized based on two methods i.e. maximum damping criterion and H_∞ optimization which consists in minimizing the settling time of the impulse response and the peak amplitude in the frequency domain, respectively. The control performance of RFF in terms of vibration attenuation, stability, and robustness is compared to IFF and α-controller.

3.1.1 Mathematical model and analysis

Fig. 3.1 shows the system under study which includes a SDOF oscillator with a mass m and a stiffness k combined with a force actuator F_a and a collocated force sensor F_s. The actuator possess an internal stiffness k_a which is in parallel with the main stiffness of the structure. The system is excited by a disturbance force F_d. When the active control is turned off, the SDOF is assumed to be undamped for the sake of simplicity. The governing equations of motion in Laplace domain

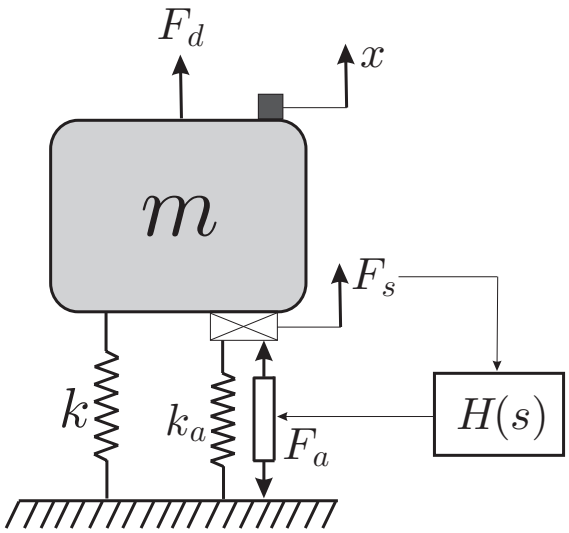

Figure 3.1: Mechanical diagram of the system under consideration including a SDOF system coupled with a force sensor and a force actuator.

Table 3.1: Optimal parameters of the system using IFF

Parameters	Maximum damping [76]	H_∞ [77]
g_i^{opt}	$\Omega_0\sqrt{\frac{\Omega_0}{\omega_0}}$	$\sqrt{\frac{\Omega_0^2+\omega_0^2}{2}}$
Optimized parameter	$\xi^{opt}=\frac{\Omega_0-\omega_0}{2\Omega_0}$	$\lvert\frac{x}{F_d}\rvert_{max}=\frac{1}{\frac{m}{4}(\Omega_0^2-\omega_0^2)}$

read:

$$(ms^2+k)x = F_d + F_s \tag{3.1a}$$

$$F_s = F_a - k_a x \tag{3.1b}$$

where s and x are the Laplace variable and the displacement of the mass. Therefore, the transfer function from the actuator to the sensor, when the feedback loop is open, can be derived as:

$$G = \frac{F_s}{F_a} = \frac{ms^2+k}{ms^2+k+k_a} \tag{3.2}$$

which contains a zero $\omega_0 = \sqrt{\frac{k}{m}}$, representing the resonance frequency of the system when the force sensor is removed, and a pole $\Omega_0 = \sqrt{\frac{k+k_a}{m}}$, representing the resonance frequency of the coupled system. In addition, the control force F_a is formed like:

$$F_a = -H(s)F_s \tag{3.3}$$

where $H(s)$ is the control law.

IFF

A classical control law to damp the resonance of the system is known as IFF which includes an integrator with the gain g_i as:

$$H(s) = \frac{g_i}{s} \tag{3.4}$$

The optimal value of the feedback gain has been already derived analytically based on the maximum damping criterion [76] and H_∞ optimization [77] as shown in Table 3.1. According to it, it can be concluded that the maximum achievable damping ξ_c^{opt} rapidly decreases and subsequently the minimal maximum of the response $\lvert\frac{x}{F_d}\rvert_{max}$ increases under two conditions. One is for high frequency resonance and the other one is when the actuator is weakly coupled to the structure which leads to a close location of the frequency of the pole Ω_0 and the zero ω_0.

α-controller

To improve the control authority, Chesné et al. [50] proposed a new control law which includes double integrator and a real zero as shown below:

$$H(s) = \frac{g_a(s+\alpha_a)}{s^2} \tag{3.5}$$

where g_a and α_a are its feedback gain and the tuning frequency of its zero. These parameters have been optimized based on the method of maximum damping [50] and H_∞ approach [11] as expressed in Table 3.2. It can be clearly concluded that for a primary system, α-controller provides a higher closed-loop damping ratio ξ^{opt} and subsequently a lower maximum amplitude of response $\lvert\frac{x}{F_d}\rvert_{max}$ than the classical IFF when the parameters are optimized based on the method of maximum damping and H_∞ approach, respectively.

RFF

In order to avoid a significant amplification of the low frequency content which can be induced by the IFF and the a-controller due to the pure integration, we propose another control law based on a second order filter like:

$$H(s) = \frac{g_f \omega_f^2}{s^2 + 2\xi_f \omega_f s + \omega_f^2} \tag{3.6}$$

where g_f is the feedback gain, ξ_f and ω_f are the damping ratio and the tuning frequency of the controller. In this case, the actuator is driven by an active damping force which is generated by making the signal proportional to the force applied to the structure resonate. By substituting Eq. (3.6) into Eq. (3.1), the driving point receptance of the system can be obtained as:

$$\frac{x}{F_d} = \frac{s^2 + 2\xi_f \omega_f s + \omega_f^2 + g_f \omega_f^2}{m\left((s^2+\omega_0)(s^2 + 2\xi_f \omega_f s + \omega_f^2 + g_f \omega_f^2) + (\Omega_0^2 - \omega_0^2)(s^2 + 2\xi_f \omega_f s + \omega_f^2)\right)} \tag{3.7}$$

In the reminder of this section, the following numerical values are used: m=1kg, k=k_a=1N/m, $k_a = 0.1k$. In the following sections, mechanical analogies for IFF, α-controller and RFF are first proposed and then two tuning laws based on maximum damping criterion and H_∞ theory are employed to optimize the parameters of RFF. These include the damping ratio ξ_f, the tuning frequency ω_f and the feedback gain g_f.

Mechanical analogy

The active mount of the system under consideration is schematically shown in Fig. 3.2a. Considering the Maxwell analogy, force and velocity in the mechanical domain are variables analogous to

Table 3.2: Optimal parameters of the system using α-controller

Parameters	Maximum damping [50]	H_∞ [11]
g_a^{opt}	$2\sqrt{\Omega_0^2 - \omega_0^2}$	$\sqrt{\frac{3(\Omega_0^2-\omega_0^2)}{2}}$
α_a^{opt}	$\frac{\omega_0^2}{2\sqrt{\Omega_0^2-\omega_0^2}}$	$\frac{3\omega_0^2-\Omega_0^2}{\sqrt{6(\Omega_0^2-\omega_0^2)}}$
Optimized parameter	$\xi^{opt} = \frac{\sqrt{\Omega_0^2-\omega_0^2}}{2\omega_0}$	$\lvert\frac{x}{F_d}\rvert_{max} = \sqrt{\frac{2\omega_0^2}{\Omega_0^2-\omega_0^2}}$

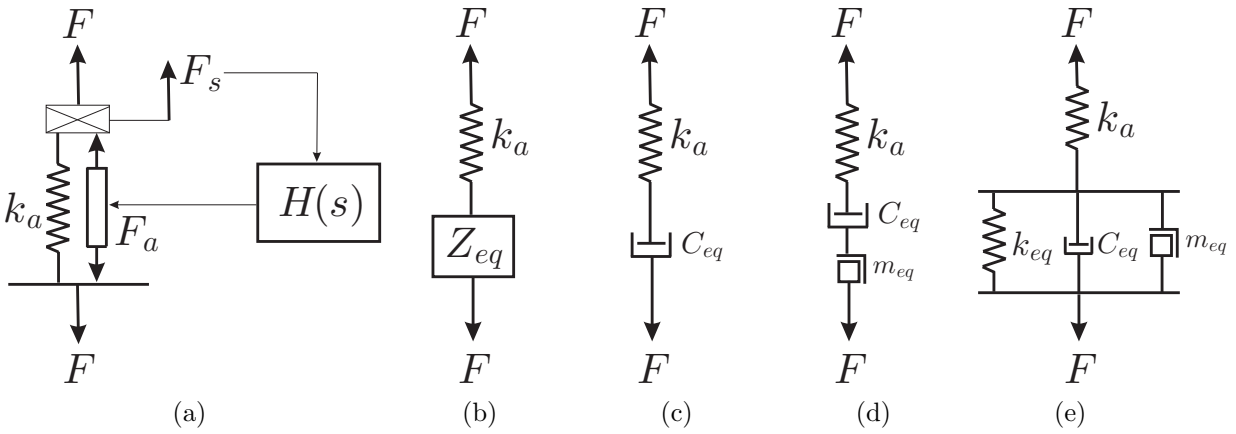

Figure 3.2: (a) Schematic of the active mount. (b) Its equivalent mechanical model. (c) The equivalent mechanical model when IFF is used. (d) The equivalent mechanical model when α-controller is used [11]. (e) The equivalent mechanical model when RFF is used.

voltage and current in the electrical domain, respectively. Therefore, its total mechanical impedance can be obtained by substituting Eq. (3.3) into Eq. (3.1) as:

$$Z_{T1} = \frac{F}{\dot{x}} = \frac{k_a}{s + s \times H(s)} \tag{3.8}$$

As presented in Fig. 3.2b, an equivalent mechanical system of the active mount can be exposed as an equivalent impedance Z_{eq} in series to an additional stiffness representing the internal stiffness of the actuator k_a. For such system, the mechanical impedance is given by:

$$Z_{T2} = \frac{F}{\dot{x}} = \frac{k_a}{s + \frac{k_a}{Z_{eq}}} \tag{3.9}$$

Therefore, the equivalent impedance is obtained by equating Eq. (3.8) and (3.9) as:

$$Z_{eq} = \frac{k_a}{s \times H(s)} \tag{3.10}$$

The equivalent impedance, when IFF is used, is calculated by substituting Eq. (3.4) into the above equation like:

$$Z_{eq}^{IFF} = \frac{k_a}{g_i} = C_{eq} \tag{3.11}$$

which presents an equivalent impedance of an viscous damper C_{eq}. As shown in Fig. 3.2c, the mechanical model of the active mount, when IFF is implemented, exhibits the same dynamic system as a relaxation isolator. Thus, the classical IFF can be seen as the active realization of the relaxation isolator. Similar study to realize this dynamic system with an electromagnetic transducer connected to a RL circuit has been introduced in [37].
To attain the equivalent impedance of α-controller, Eq. (3.5) is substituted into Eq. (3.10) as:

$$Z_{eq}^{\alpha} = \frac{k_a s}{g_a(s + \alpha_a)} = \frac{m_{eq} C_{eq} s}{m_{eq} s + C_{eq}} \tag{3.12}$$

which represents an equivalent impedance of an inertance m_{eq} in series to a viscous damping C_{eq}. In this case, the mechanical model of the active mount can be considered as tuned-inerter-damper (TID) as shown in Fig. 3.2d. Therefore, α-controller can be seen as the active realization of TID, i.e. ATID. ATID has been exclusively discussed in [11].
For RFF, the equivalent impedance is obtained by substituting Eq. (3.6) into Eq. (3.10) like:

$$Z_{eq}^{RFF} = \frac{k_a}{g_f \omega_f^2} s + \frac{2\xi_f k_a}{g_f \omega_f} + \frac{k_a}{g_f s} = m_{eq} s + C_{eq} + \frac{k_{eq}}{s} \tag{3.13}$$

which indicates an equivalent impedance of an inertance $m_{eq} = \frac{k_a}{g_f \omega_f^2}$ in parallel to a viscous damping $C_{eq} = \frac{2\xi_f k_a}{g_f \omega_f}$ as well as a stiffness $k_{eq} = \frac{k_a}{g_f}$ as shown in Fig. 3.2e. Clearly, it can be considered as an inerter-spring-damper system known as ISD. Thus, RFF can be seen as active realization of ISD. Note that ISD has been used in vibration isolation [78], vehicle suspension [79], railway vehicle suspension [80], aircraft landing gear suspension [81]. From Eq. (3.13), g_f, ξ_f and ω_f can be obtained as a function of m_{eq}, C_{eq} and k_{eq} as:

$$g_f = \frac{k_a}{k_{eq}}, \quad \xi_f = \frac{C_{eq}}{2\sqrt{m_{eq} k_{eq}}}, \quad \omega_f = \sqrt{\frac{k_{eq}}{m_{eq}}} \tag{3.14}$$

where ω_f and ξ_f can be seen as the natural frequency and the damping ratio of ISD, respectively. g_f also shows the stiffness ratio between k_a and k_{eq}. One sees that ISD behaves like a rigid body motion with infinite mass, damping and stiffness when $g \to 0$. Subsequently, it is no longer effective for vibration control and the coupled system resonates at Ω_0. For $g \to \infty$, all the parameters of ISD become zero. Since the stiffness k_a is placed in series to ISD, the whole branch becomes ineffective. Thus, the resulting resonance of the coupled system is the same as the primary system when the active mount is removed i.e. ω_0.

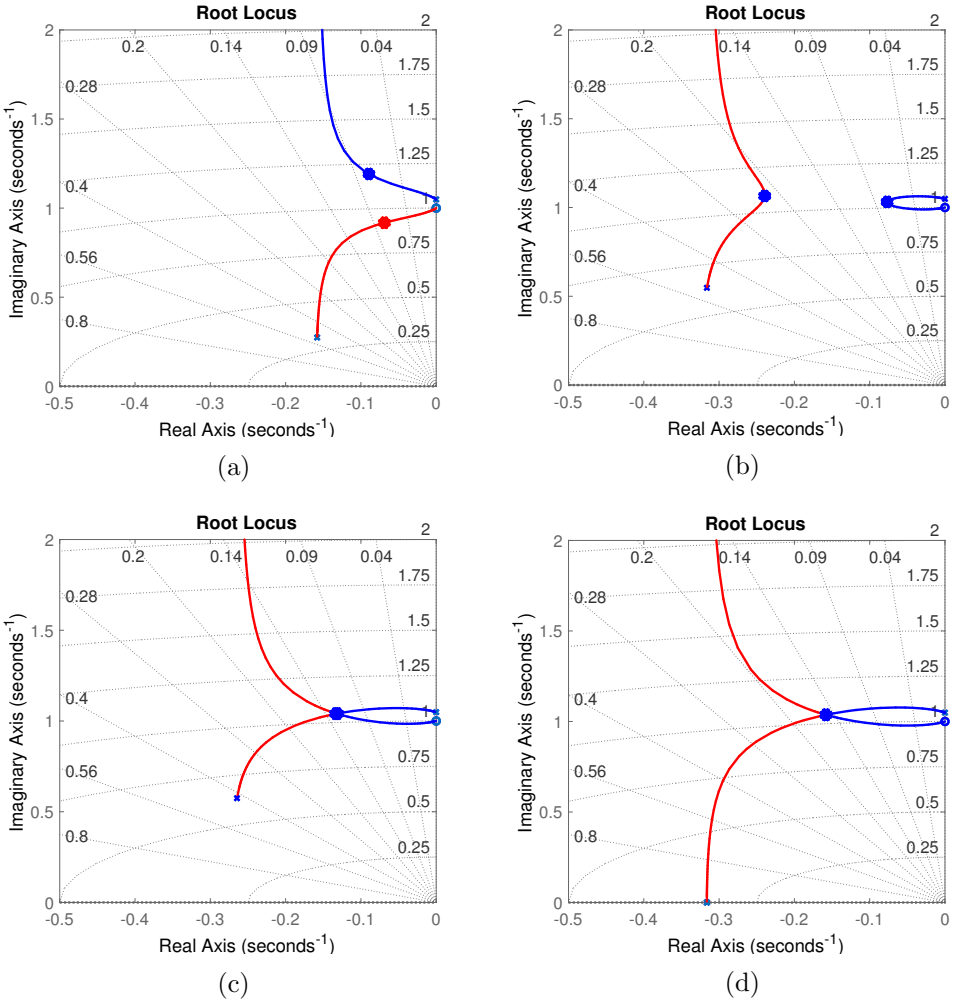

Figure 3.3: Typical root-locus of the system coupled with RFF when the tuning frequency and the damping ratio of RFF are set to (a) lower values than those of local optimal case, (b) higher values than those of local optimal case, (c) their local optimal case, (d) their optimal case. (• shows the closed-loop poles)

3.1.2 Maximum damping optimization of the absorber

In this section, the parameters of the controller are optimized based on the method of maximum damping which consists in minimizing the settling time of the impulse response. Fig. 3.3 shows the root-locus of the loop gain (i.e. $G \times H$) choosing different control parameters. One sees that the controller adds another set of poles to the resulting closed-loop system. Depending on the value of the feedback gain g_f, the closed-loop poles can move individually on two loops starting from the pole of the system as well as the pole of the controller. In addition, the location of the controller pole in the locus is a function of the damping ratio ξ_f and tuning frequency ω_f of the controller which leads to different shape of the loops. By comparing Fig. 3.3c with Figs. 3.3a and 3.3b, it can be concluded that the damping of the closed-loop system is locally maximized when the two loops intersect at one point. In this case, the closed-loop poles are merged at the intersection. It is possible to realize an identical closed-loop poles for different target damping by properly tuning the parameters of RFF. This can be seen from Fig. 3.3c and Fig. 3.3d that the controller which realizes equal closed-loop poles is not unique. However, there is only one controller which makes the loops as large as possible and this occurs when the controller pole is critically damped (i.e. $\xi_f^{opt} = 1$). It should be also noted that the closed-loop system is unconditionally stable for any

value of feedback gain, damping ratio and tuning frequency. Similar approach has been used to optimize the parameters of positive-position-feedback (PPF) control system in [82]. It is worth pointing out that the values of ω_f, ξ_f and g_f are taken arbitrarily to observe the different possible root locus curves in Fig. 3.3. Considering the values of ξ_f and ω_f corresponding to Fig. 3.3c as the local optimum ones, Fig. 3.3a shows a typical root locus of the system when a lower value of ξ_f or ω_f is taken. For a higher value of ξ_f or ω_f, the typical root locus of the system is shown in Fig. 3.3b.
The driving point receptance of the system when the two poles are merged is given by:

$$\frac{x}{F_d} = \frac{s^2 + 2\xi_f\omega_f s + \omega^2 + g_f\omega_f^2}{(s^2 + 2\xi_c\omega_c s + \omega_c^2)^2} \tag{3.15}$$

where ξ_c and ω_c are the damping ratio and the resonance frequency of the closed-loop system, respectively. The following equations are obtained by equating the characteristic polynomial coefficients of Eqs. (3.7) and (3.15).

$$4\xi_c\omega_c = 2\xi_f\omega_f \tag{3.16a}$$
$$(4\xi_c^2 + 2)\omega_c^2 = (g_f + 1)\omega_f^2 + \Omega_0^2 \tag{3.16b}$$
$$4\xi_c\omega_c^3 = 2\xi_f\omega_f\Omega_0^2 \tag{3.16c}$$
$$\omega_c^4 = g_f\omega_f^2\omega_0^2 + \omega_f^2\Omega_0^2 \tag{3.16d}$$

Substituting Eq. (3.16a) into Eq. (3.16c) considering $\xi_f = \xi_f^{opt} = 1$ leads to:

$$\omega_c = \Omega_0 \tag{3.17}$$

which means that the resonance frequency of the closed-loop system is the same as the resonance frequency of the system when the feedback loop is open. From Eq. (3.16a), the closed-loop damping ratio can be obtained as a function of tuning frequency of the controller as $\xi_c = \frac{\omega_f}{2\Omega_0}$. Therefore, by substituting it into Eqs. (3.16b) and (3.16d) and solving the resulting equations for the tuning frequency of the controller and the feedback gain, the corresponding optimal parameters of the controller can be derived as:

$$\omega_f^{opt} = \sqrt{\Omega_0^2 - \omega_0^2} \tag{3.18a}$$
$$g_f^{opt} = \frac{\Omega_0^2}{\Omega_0^2 - \omega_0^2} \tag{3.18b}$$

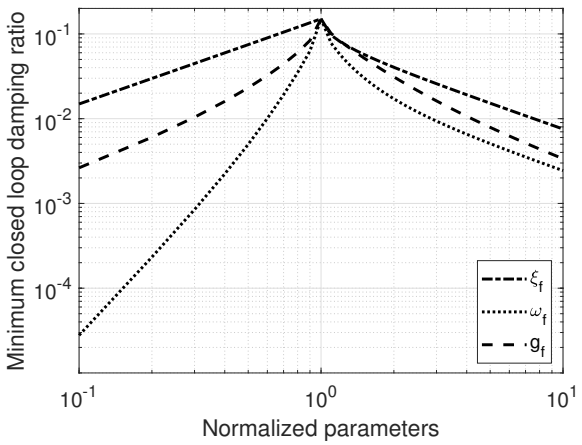

Figure 3.4: Minimum closed-loop damping ratio of the system against the variation of the parameters of RFF normalized with respect to their optimal parameters.

And subsequently the closed damping ratio can be obtained:

$$\xi_c^{opt} = \frac{\sqrt{\Omega_0^2 - \omega_0^2}}{2\Omega_0} \tag{3.19}$$

Figs. 3.4 presents the minimum closed-loop damping ratio of the system against the variation of parameters of RFF normalized with respect to their optimal values. Note that when one parameter changes, the other parameters are set to their optimal values. It can be clearly seen that only the optimal parameters provide maximum damping.

As it was already mentioned at the beginning of the section 3.1.2, the goal of the optimization is not only to maximize the closed-loop damping but also to minimize the settling time of the impulse response. Therefore, Fig. 3.5a shows the impulse response of the system for $\xi_f/\xi_f^{opt} : 1/1.3, 1, 1.3$ while the tuning frequency ω_f and the feedback gain g_f are set to their optimal values. Furthermore, the impulse response is demonstrated in Fig. 3.5b for $\omega_f/\omega_f^{opt} : 1/1.3, 1, 1.3$ when ξ and g_f are fixed at their optimal values. In addition, for $g_f/g_f^{opt} : 1/1.3, 1, 1.3$ when ξ_f and ω_f are kept at their optimal values, Fig. 3.5c illustrates the impulse response. It can be seen that only the optimal values of ω_f and g_f realize the minimum settling time. However, for the case of ξ_f, a lower value offers a better settling time. To better illustrate this issue, the settling time is shown in Fig.

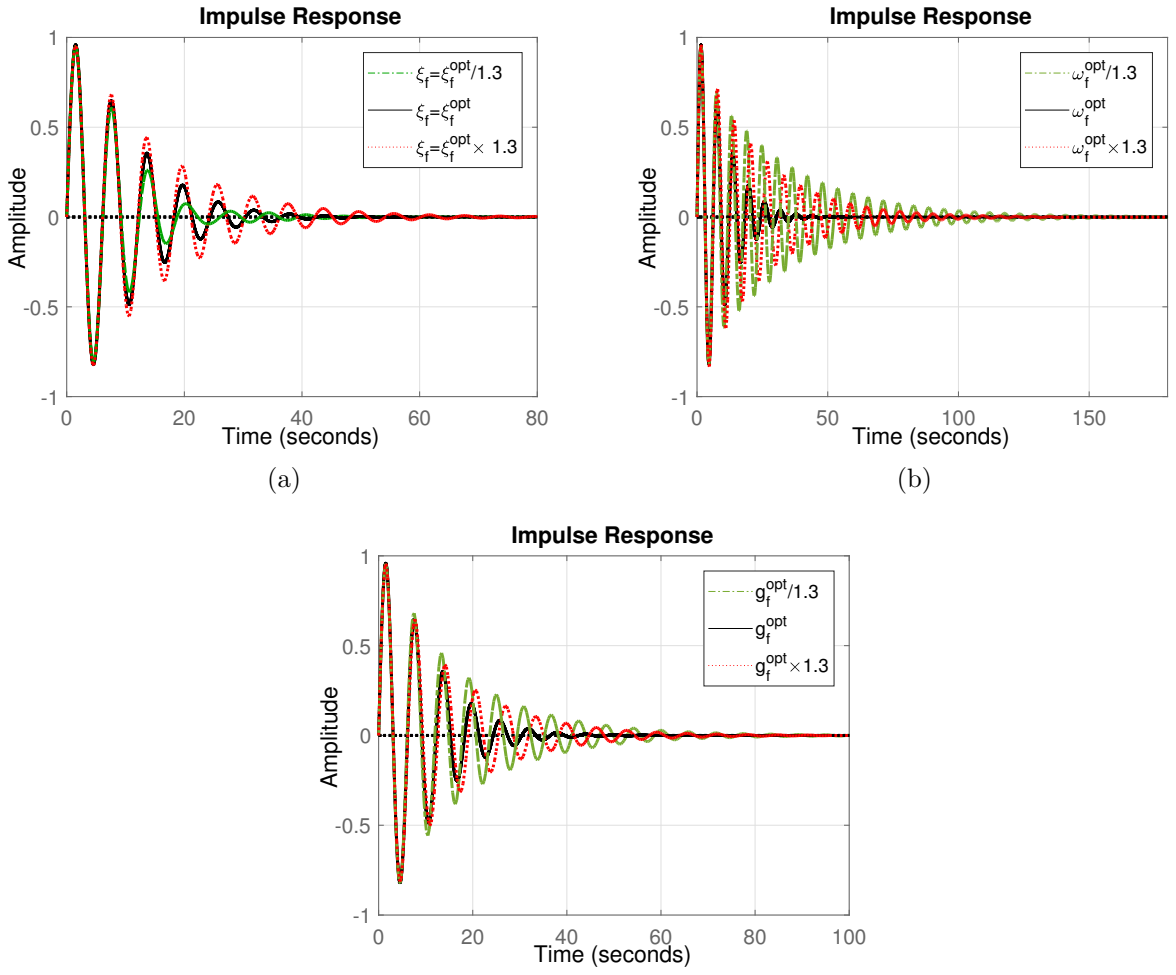

Figure 3.5: Impulse response of the coupled system with RFF for different values of (a) damping coefficient ξ_f, (b) tuning frequency ω_f and (c) feedback gain g_f.

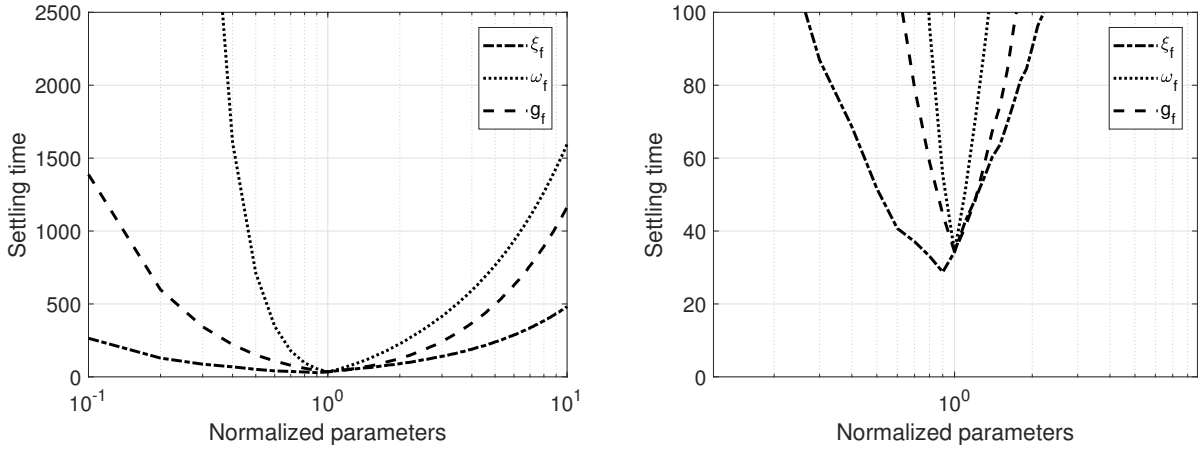

(a) (b)

Figure 3.6: (a) Settling time as a function of the variation of the parameters of RFF normalized with respect to their optimal values, (b) a zoom from 0 to 100 seconds.

3.6 when the parameters of RFF are varied. 15% reduction in the settling time happens when the damping ratio ξ_f is 10% lower than the optimal value. At this stage, it is not very clear the reason for not having minimum settling time with the maximum damping. Although, this can be related to the fact that the settling time can be dominated not only by the damping ratio but also by the resonance frequency of the system. It gets even more complicated to estimate since the resulting closed-loop system contains two poles with the same damping ratio but different resonance frequencies (according to Fig. 3.3a) when the damping ratio of RFF gets detuned to a lower value. The damping ratio and resonance frequency of both poles can affect the settling time. Therefore, a more careful analysis needs to be done in the future to provide more detail in this subject.

On the other hand, this phenomenon only happens when $\frac{k_a}{k} < 0.5$. For example when $\frac{k_a}{k} = 0.5$, the minimum closed-loop damping ratio and the settling time are plotted against the normalized parameters of RFF in Figs. 3.7a and 3.7b, respectively. Obviously, the optimal parameters not only realize the maximum damping but also the minimum settling time. Comparing the performance

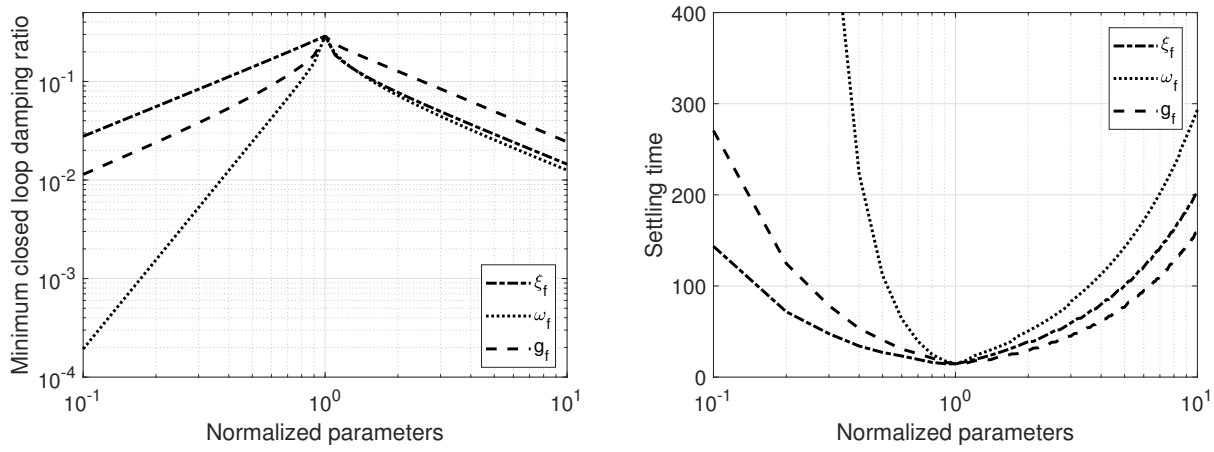

(a) (b)

Figure 3.7: Under the variation of the parameters of RFF normalized with respect to their optimal parameters when $\frac{k_a}{k} = 0.5$, (a) minimum closed-loop damping ratio and (b) settling time.

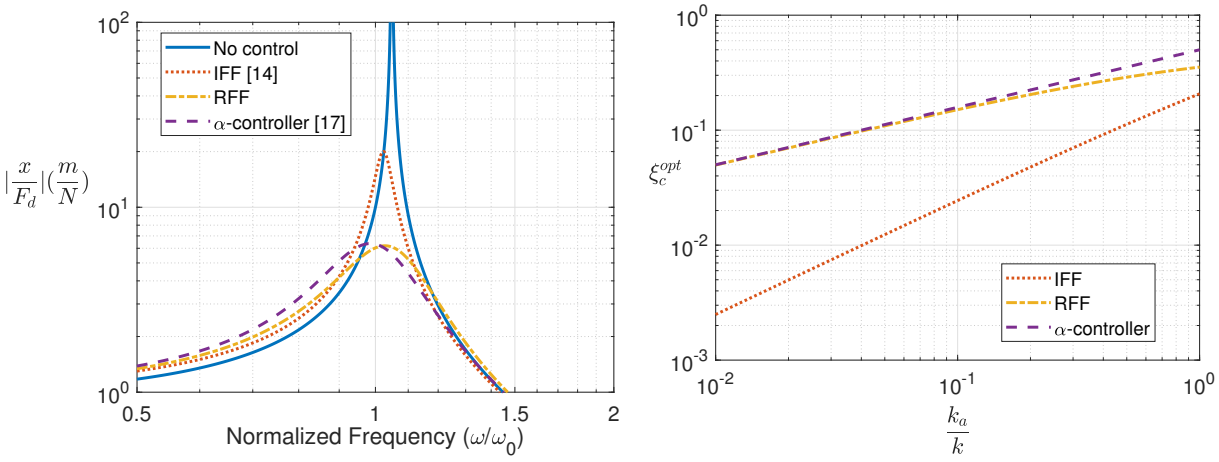

(a) (b)

Figure 3.8: When parameters of IFF, α-controller as well as RFF are optimized based on the method of maximum damping, (a) FRF of the the performance index with and without control systems for $k_a = 0.1k$, (b) optimal closed-loop damping coefficient ξ_c^{opt} under the variation of the stiffness ratio $\frac{k_a}{k}$.

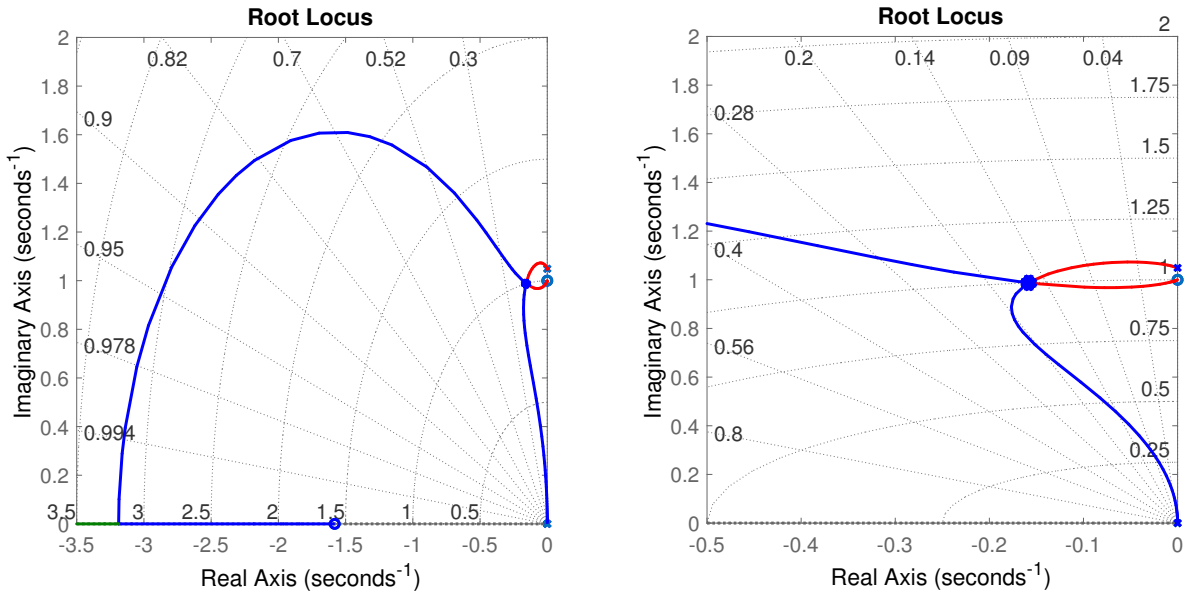

(a) (b)

Figure 3.9: (a) Root-locus of the system coupled with α-controller, (b) a zoom on a real axis from -0.5 to 0.

of the system in terms of the settling time and the minimum closed-loop damping ratio under deviations of the parameters of RFF from the optimal values (Figs. 3.4-3.7), it can be concluded that the performance of RFF is highly sensitive to the variation of the tuning frequency ω_f. In other words, it shows how robust RFF is under the resonance uncertainty which will be further discussed in Section 3.1.5.

Fig. 3.8a shows the FRF of the performance index with and without control systems. It also compares the performance of RFF with IFF [76] and α-controller [11] when they are optimized based on the method of maximum damping. In order to reveal the difference of using RFF in comparison to IFF and α-controller, Fig. 3.8b presents the evolution of the maximum closed-loop damping ratio

under the variation of the stiffness ratio ($\frac{k}{k_a}$). It is explicitly obvious that RFF and α-controller add more damping to the structure in comparison to the one with IFF. The out-performance occurs since both RFF and α-controller introduce an anti-resonance to the primary system allowing a better interaction between the actuator and the primary structure. Considering lightly damped structures where the primary system possess 1% or less damping ratio, it can be concluded that IFF is no longer effective when the stiffness ratio is lower than 5%. However in this case, RFF and α-controller can add at least 10 times greater damping ratio. Another interesting observation is that both RFF and α-controller provide a very close damping ratio especially when the stiffness ratio is low, i.e. $\frac{k_a}{k} < 0.2$. This can be seen by the root-locus of the system when α-controller is implemented as shown in Fig. 3.9 for $\frac{k_a}{k} = 0.1$. It shows that the maximum achievable damping ratio, which occurs when the two loops are interesting at one point, is about 15.8%; while RFF can realize 15.1% damping ratio according to Fig. 3.3d. More details on the root-locus of the system coupled with the α-controller under the deviation of its parameters can be found in [50]. Although the α-controller gives a slightly better control authority when $\frac{k_a}{k} > 0.2$, the difference is not major. For example, if $\frac{k_a}{k} = 1$, the closed-loop damping ratios provided by RFF and α-controller are 0.35 and 0.5, respectively. This slightly better damping ratio provided by α-controller affects the stability of the system in terms of phase margin which will be discussed in Section 3.1.5.

3.1.3 H_∞ optimization of the absorber

Another tuning method based on H_∞ optimization is used in this section to optimize the parameters of the controller. The optimization is known as an approximation of fixed-point theory which has been introduced by Den Hartog [64] to optimally design parameters of tuned-mass-damper (TMD) system. The optimization aims to minimize the response at the fixed-points. The fixed-points are defined as those frequencies where the magnitude of the deriving point receptance of the system is invariant with respect to the damping coefficient of the controller ξ_f. The magnitude of the frequency response of the driving point receptance is taken as the performance index and it is given by substituting $s = j\omega$ into Eq. (3.7) as:

$$
\begin{aligned}
|\frac{x}{F_d}| =& \frac{\sqrt{\omega^4 + (4\xi_f^2\omega_f^2 - 2g_f\omega_f^2 - \omega_f^2)\omega^2 + (g_f+1)\omega_f^4}}{m\sqrt{D_8\omega^8 + D_7\omega^7 + D_6\omega^6 + D_5\omega^5 + D_4\omega^4 + D_3\omega^3 + D_2\omega^2 + D_1\omega + D_0}} \qquad (3.20a)\\
D_8 =& 1; D_7 = D_5 = D_3 = D_1 = 0\\
D_6 =& 2(2\xi_f^4 - g_f - 1)\omega_f^2 - 2\Omega_0^2\\
D_4 =& (g_f+1)^2\omega_f^4 - (8\xi_f^2\Omega_0^2 - 2g_f(\Omega_0^2+\omega_0^2) - 4\Omega_0^2)\omega_f^2 + \Omega_0^4\\
D_2 =& (4\xi_f^2\Omega_0^4 - 2g_f\omega_0^2\Omega_0^2 - 2\Omega_0^4)\omega_f^2 - (2g_f^2\omega_0^2 + 2g_f(\Omega_0^2+\omega_0^2) + 2\Omega_0^2)\omega_f^4\\
D_0 =& (g_f\omega_0^2 + \Omega_0^2)^2\omega_f^4
\end{aligned}
$$

The fixed-point frequencies are obtained by differentiating the above equation with respect to the damping coefficient ξ_f and equating the derivative to zero, which yields:

$$\Omega_1 = \frac{1}{\sqrt{2}}\sqrt{(g_f+1)\omega_f^2 + \Omega_0^2 - \sqrt{(g_f+1)^2\omega_f^4 - 2g_f\omega_0^2\omega_f^2 - 2\Omega_0^2\omega_f^2 + \Omega_0^4}} \qquad (3.21a)$$

$$\Omega_2 = \frac{1}{\sqrt{2}}\sqrt{(g_f+1)\omega_f^2 + \Omega_0^2 + \sqrt{(g_f+1)^2\omega_f^4 - 2g_f\omega_0^2\omega_f^2 - 2\Omega_0^2\omega_f^2 + \Omega_0^4}} \qquad (3.21b)$$

$$\Omega_3 = 0 \qquad (3.21c)$$

The third fixed-point Ω_3 is neglected in the following process as it is basically invariant with respect to the parameters of RFF. The optimal value of the tuning frequency ω_f is defined as the one which realizes equal performance at the fixed-point frequencies. This can be obtained by

substituting Eqs. (3.21)a and (3.21)b into Eq. (3.20) and equating the resulting expressions for a $\xi_f = 0$, which yields:

$$\omega_f^{opt} = \frac{\Omega_0}{\sqrt{g_f + 1}} \tag{3.22}$$

The performance index at fixed-points does not change for any value of the damping coefficient through the whole frequency range. Therefore, the optimal value of the damping ratio ξ_f is obtained by passing the performance index horizontally through the fixed-points. Two optimal damping coefficients corresponding to two fixed-points can be obtained as:

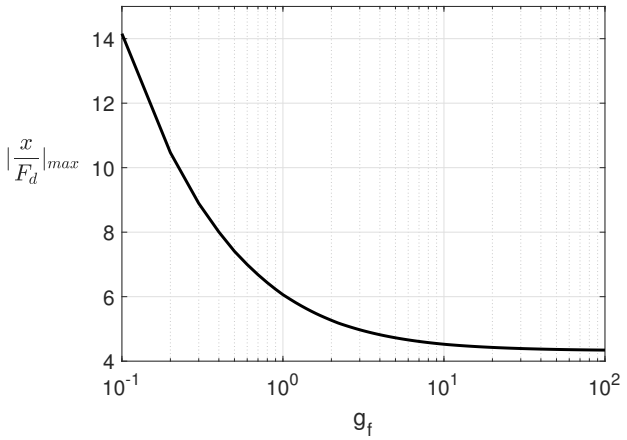

(a)

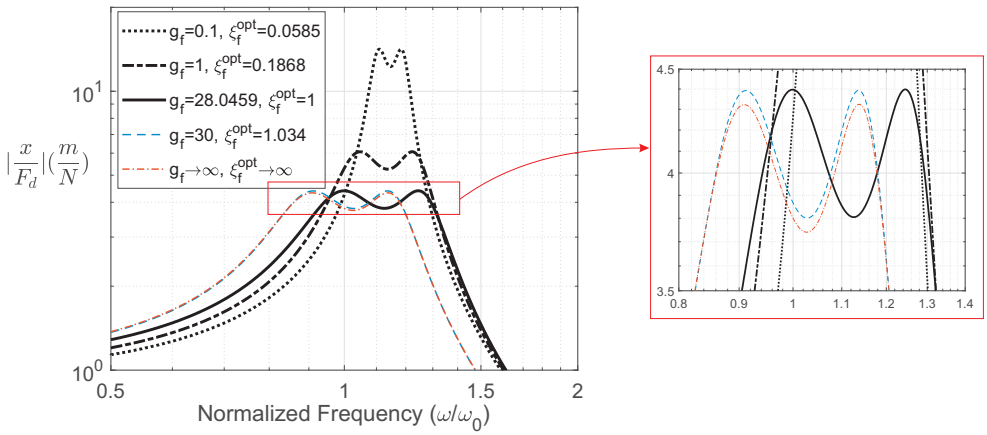

(b)

Figure 3.10: (a) Maximum amplitude of response against the feedback gain g_f. (b) FRF of the performance index for different values of the feedback gain g_f when the other parameters follow their optimal values.

$$\xi_{f1} = \frac{\sqrt{H_1 g_f \left(H_2(g_f+1) - H_1 g_f + 2\sqrt{H_1 g_f \left(-2H_2(g_f+1) + (2(g_f+1))\Omega_0^2 + H_1 g_f\right)}\right)}}{2\sqrt{2H_2(g_f+1)\Omega_0^2 + H_1 H_2 g_f - 4H_1 g_f \Omega_0^2}} \tag{3.23a}$$

$$\xi_{f2} = \frac{\sqrt{H_1 g_f \left(H_2(g_f+1) + H_1 g_f + 2\sqrt{H_1 g_f \left(2H_2(g_f+1) + (2(g_f+1))\Omega_0^2 + H_1 g_f\right)}\right)}}{2\sqrt{2H_2(g_f+1)\Omega_0^2 + H_1 H_2 g_f + 4H_1 g_f \Omega_0^2}} \tag{3.23b}$$

$$H_1 = \Omega_0^2 - \omega_0^2$$
$$H_2 = \Omega_2^2 - \Omega_1^2$$

In practice, the optimal value of the damping is considered by taking the quadratic average of the two obtained damping ratio Eqs. (3.23)a and (3.23)b:

$$\xi_f^{opt} = \sqrt{\frac{\xi_{f2}^2 + \xi_{f1}^2}{2}} \tag{3.24}$$

The optimal value of the feedback gain g_f still needs to be obtained. Fig. 3.10a illustrates the maximum amplitude of the response against the feedback gain g_f when the tuning frequency ω_f and the damping ratio ξ_f are set to their optimal values. It can be clearly seen that the maximum amplitude of response starts to decrease by increasing g_f. However, it stops decreasing after a certain value of a feedback gain which can be introduced as its optimal value. Fig. 3.10b shows the frequency-response-function (FRF) of the performance index for five different values of the feedback gain $g_f : 0.1, 1, 28.0459, 30, \infty$ when the other two parameters (ω_f and ξ_f) follow their optimal values. One sees that the optimal parameters of the damping ratio ξ_f^{opt} and tuning frequency ω_f^{opt} can realize equal peak for each value of the feedback gain g_f. In addition, the performance index indeed decreases with an increase in the feedback gain until the damping ratio reaches the critical damping. By increasing the feedback gain more, the resonance of the system is shifted slightly to a lower value with a negligible change in the amplitude of response. Therefore, the minimum feedback gain g_f, which realizes the minimal maximum amplitude of response, is defined as the optimal feedback gain. This occurs when the damping coefficients reaches the critical value. By equalizing Eq. (3.24) to one and solving the resulting equation, the optimal value of the feedback gain is given by:

$$g_f^{opt} = \frac{\Omega_0^2 + 7\omega_0^2 + \sqrt{64\omega_0^4 + 112\omega_0^2(\Omega_0^2 - \omega_0^2) + 97(\Omega_0^2 - \omega_0^2)^2)}}{6(\Omega_0^2 - \omega_0^2)} \tag{3.25}$$

Fig. 3.11a illustrates FRF of the performance index with and without control systems to compare the vibration attenuation brought by IFF, α-controller and RFF when they are tuned based on H_∞ optimization. It can be seen that the maximum amplitude of the response associated with RFF or α-controller is more than four times lower than the one with IFF. This plot is also interesting because it demonstrates that both α-controller and RFF realize equal peak with slightly different frequencies. To better understand the difference between the performance of the control laws, Fig. 3.11b presents the maximum amplitude of the performance index as a function of the stiffness ratio when parameters are tuned based on H_∞ optimization. It is clearly visible that RFF and α-controller always offer a better amplitude reduction especially when the coupling between the actuator and the structure is low (i.e. $\frac{k}{k_a} < 0.1$). For example, RFF or α-controller is able to reduce the amplitude of response 10 times lower than the one with IFF when the stiffness ratio is about 2%. An additional observation from this plot is that the vibration attenuation brought by RFF and α-controller is very close to each other especially for $\frac{k_a}{k} < 0.5$. For high stiffness ratio, the difference gets slightly larger such that when $\frac{k_a}{k} = 1$, the maximum amplitude of response is 1.23 and 1.41 with the application of RFF and α-controller, respectively.

It is worth pointing out that the application of RFF results in a dynamically softer system because of a higher static response with respect to that of control-off. This can be justified using the mechanical analogy of RFF shown in Fig. 3.2e. At low frequency, RFF behaves like two stiffness (i.e. k_a and k_{eq}) which are placed in series with each other. In this case, the stiffness of the branch is equal to $\frac{k_a}{1+g_f}$ which is lower than k_a.

It is also interesting to see how sensitive the performance of the system is when RFF is detuned. Fig. 3.12a shows the FRF for five different damping ratios as $\xi_f/\xi_f^{opt} : 0, 0.25, 1, 4, \infty$, while the other parameters are set to their optimal values. The fixed-points can be seen at two frequencies where all the curves are interesting. For $\xi_f < \xi_f^{opt}$, two resonances with higher peaks appear in the vicinity of the primary one; whereas, only one resonance peak can be seen when $\xi_f > \xi_f^{opt}$. It is aligned with the RFF's mechanical analogy shown in Fig. 3.2e. According to Eq. (3.14) when $\xi_f \to 0$, the equivalent damping approaches the zero value ($\equiv C_{eq} \to 0$) while the equivalent inertance and the stiffness are non-zero value ($\equiv m_{eq} \neq 0$ and $k_{eq} \neq 0$). This means that RFF adds another undamped DOF to the system. However, $C_{eq} \to \infty$ when $\xi_f \to \infty$ as well. Therefore, RFF is no longer effective and the system resonates at the resonance frequency of the primary system ($\equiv \Omega_0$). The performance degradation of RFF under the variation of the tuning frequency ω_f is demonstrated in Fig. 3.12b for five different values as: $\omega_f/\omega_f^{opt} : 0, 0.75, 1, 1.33, \infty$, when ξ_f and g_f are set to their optimal values. Moreover, to see how the performance is degraded when the feedback gain is detuned, the FRF is plotted for five different values as: $g_f/g_f^{opt} : 0, 0.5, 2, \infty$ accompanied by fixing the other parameters to their optimal values. RFF gets detuned in the same way by the variation of the tuning frequency or the feedback gain such that the one peak increases accompanied by decreasing the other one. When $\omega_f \to 0$, it is equivalent to infinite value of the inertance and the damping ($\equiv m_{eq}, C_{eq} \to \infty$). Furthermore, when $g_f \to 0$, all the equivalent parameters go to infinite value ($\equiv m_{eq}, C_{eq}, k_{eq} \to \infty$). In both cases, similar to $\xi_f \to \infty$, RFF is no longer effective and the system keeps resonating at the resonance frequency of the primary system ($\equiv \Omega_0$). On the other hand when $\omega_f \to \infty$, RFF degrades to a non-zero value stiffness ($\equiv k_{eq} \neq 0$) causing a reduction in the resonance frequency since the equivalent stiffness is placed in series to the stiffness of the actuator. The total stiffness of the branch (Fig. 3.2e) is now equal to $\frac{k_a}{1+g_f}$. In the case of $g_f \to \infty$, the impedance of RFF becomes zero such that no force will pass

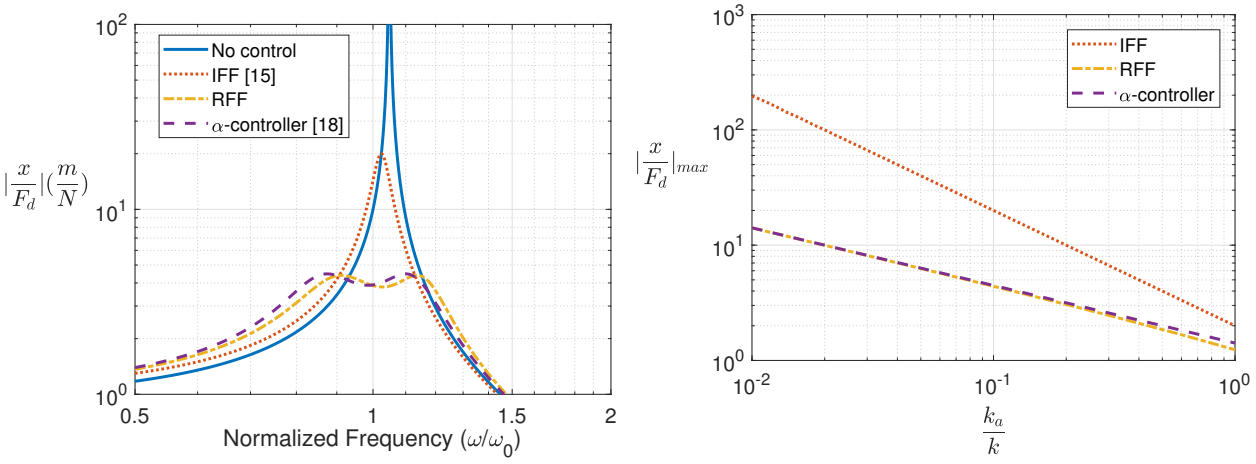

(a) (b)

Figure 3.11: When parameters of IFF, α-controller as well as RFF are tuned based on H_∞ optimization, (a) FRF of the performance index with and without control systems for $k_a = 0.1k$, (b) maximum amplitude of the performance index under the variation of the stiffness ratio $\frac{k_a}{k}$.

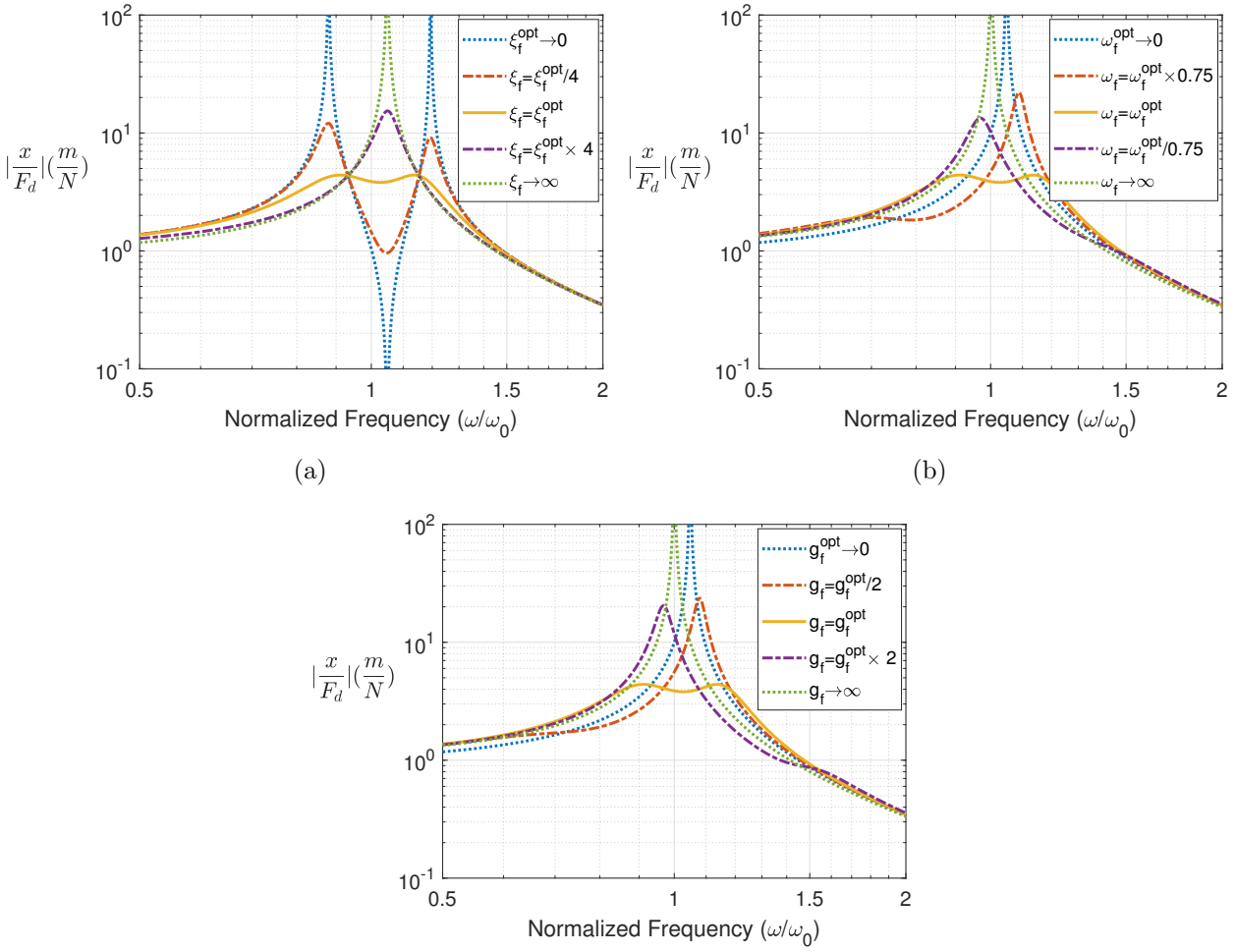

Figure 3.12: FRF of the performance index for different values of (a) the damping ratio ξ_f, (b) tuning frequency ω_f and (c) feedback gain g_f when the other parameters are set to their optimal values.

through the branch (Fig. 3.2e) as if it is removed from the system. Hence, the resonance frequency of the system is equal to the resonance frequency of the primary system when the force sensor is taken away ($\equiv \omega_0$). It is worth pointing out that the amplitude of response is more sensitive to the tuning frequency than the others because the peaks get detuned rapidly by slightly deviating from its optimum.

3.1.4 Control effort

It has been shown in the previous section that both RFF and α-controller provide almost the same control authority to the system. The difference between them can be expressed in the terms of the control effort. To do so, the actuator force with respect to the input disturbance force is taken as the performance function. This performance function can be obtained using Eqs. (3.1) and (3.3) as:

$$\frac{F_a}{F_d} = \frac{k_a H(s)}{(ms^2+k)(1+H(s))+1} \tag{3.26}$$

By substituting Eq. (3.5) and Eq. (3.6) into the above equation,respectively, the performance function for α-controller and RFF can be obtained as follow:

$$\frac{F_a}{F_d} = \frac{k_a g_a(s+\alpha)}{(ms^2+k)(s^2+g_a(s+\alpha))+s^2} \tag{3.27a}$$

$$\frac{F_a}{F_d} = \frac{k_a g_f \omega_f^2}{(ms^2+k)(s^2+2\xi_f\omega_f s+\omega_f^2+g_f\omega_f^2)+s^2+2\xi_f\omega_f s+\omega_f^2} \tag{3.27b}$$

Figs. 3.13a and 3.13b show the FRF of the actuator force when parameters are optimized according to the method of maximum damping and H_∞ approach, respectively. It can be clearly seen that α-controller requires a higher actuator force than that of RFF. In addition, the maximum actuator force corresponding to α-controller is 2.67 and 2.54 greater than that of RFF when the parameters are tuned according to the method maximum damping and H_∞ approach, respectively. In other words, the amount of current needs to be delivered to the actuator for α-controller is higher than that of RFF and subsequently it consumes more power.

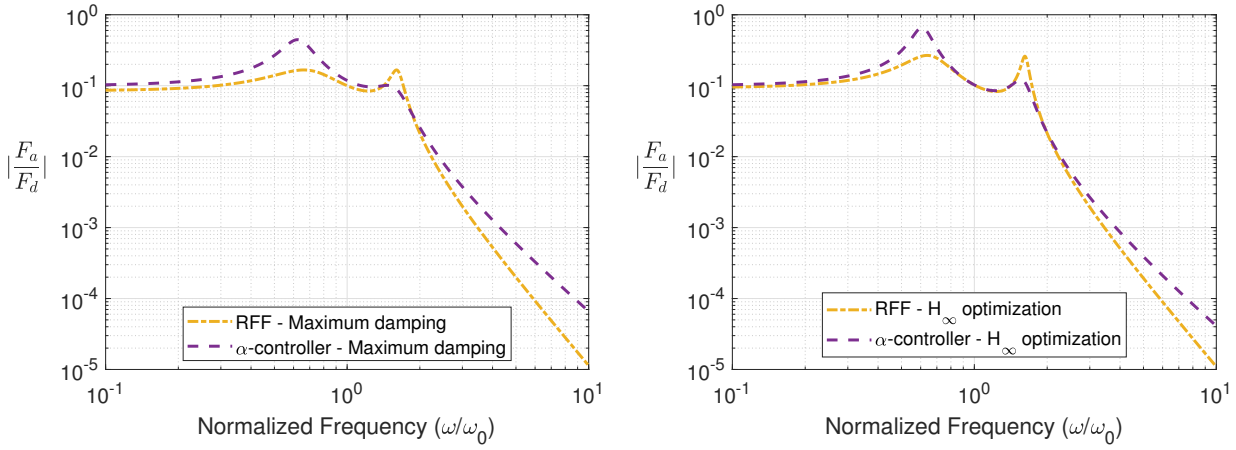

(a) (b)

Figure 3.13: FRF of the actuator force, (a) when the parameters are optimized according to the method of maximum damping, (b) when the parameters are tuned based on H_∞ optimization

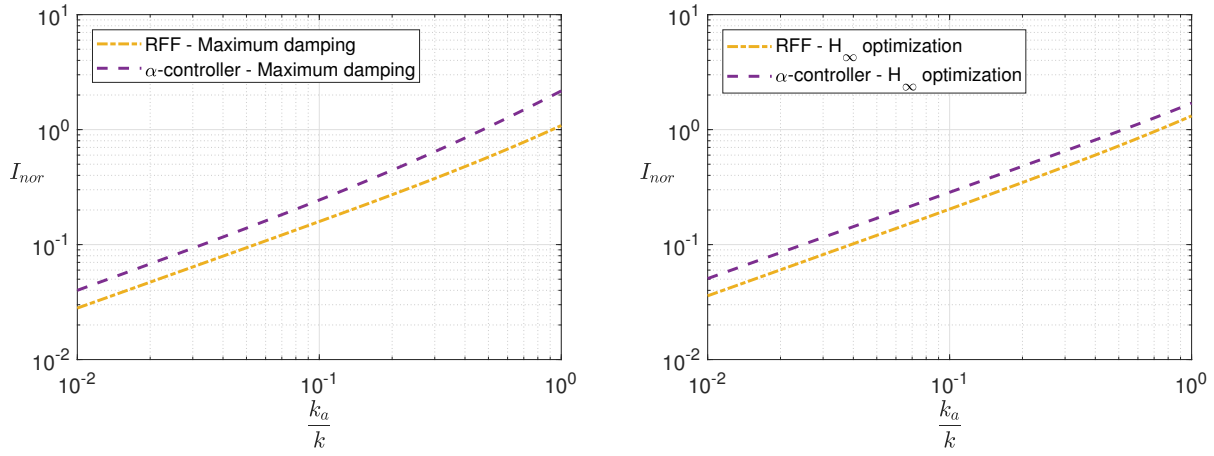

(a) (b)

Figure 3.14: Normalized root mean square value of the actuator force I_{nor} versus the variation of the stiffness ratio $\frac{k_a}{k}$ (a) when the parameters are optimized according to the method of maximum damping, (b) when the parameters are tuned based on H_∞ optimization

According to Figs. 3.13a and 3.13b, no matter which optimization criterion is used, two peaks appear in the magnitude of the force around the resonance frequency of the system for both RFF and α-controller. At the first peak, RFF requires less force than α-controller while it is the other way around at the second peak. In addition, the magnitude of actuator force contains a non-zero constant value at low frequency. It is worthwhile noting that this low frequency force interacts on the stiffness of the structure leading to a dynamically softer system as it has been already observed in the previous section from Figs. 3.8a and 3.11a where the static response has increased. For both optimization criteria, α-controller requires a higher actuator force than that of RFF at low frequency. Therefore, other than the power needs to be given to the actuator for reducing the resonance peak, an amount of current needs to be provided for the actuator for the low frequency force. Since α-controller requires more force at low frequency than RFF, low frequency force has a big impact on the total power consumption of the control system. Even at high frequency, the control force corresponding to α-controller is higher than that of RFF, although it can be neglected because of more than three order of magnitude difference compared to the low frequency force. It is clear that a criterion, which is able to consider the actuator force over the frequency-band of interest ($\pm\infty$), is required to compare RFF with α-controller. H_2 norm measures the energy of the actuator force through the whole frequency range. Consequently, H_2 norm is proposed for further comparison and it is assessed as follows [72]:

$$||F_a||_2 = \sqrt{\frac{1}{2\pi}\int_{-\infty}^{\infty} F_d(\omega)\left|\frac{k_a H(j\omega)}{(-m\omega^2+k)(1+H(j\omega))+1}\right|^2 d\omega} \tag{3.28}$$

where $F_d(\omega)$ is the power spectral density of the input disturbance force. For the case of white noise excitation force, it is constant as a function of the frequency, i.e. $f_d(\omega) = f_d$. Therefore, the H_2 norm can be simplified as:

$$||F_a||_2 = \sqrt{\frac{F_d}{2\pi}\int_{-\infty}^{\infty}\left|\frac{k_a H(j\omega)}{(-m\omega^2+k)(1+H(j\omega))+1}\right|^2 d\omega} \tag{3.29}$$

In other words, the above equation represents the root-mean-square (RMS) value of the actuator force. Then, its normalized I_{nor} is defined to highlight the ratio of the RMS of the actuator force to the excitation force with a uniform spectral density like:

$$I_{nor} = \sqrt{\frac{\pi}{F_d}}\,||F_a||_2 = \sqrt{\int_0^{\infty}\left|\frac{k_a H(j\omega)}{(-m\omega^2+k)(1+H(j\omega))+1}\right|^2 d\omega} \tag{3.30}$$

Figs. 3.14a and 3.14b present I_{nor} under the variation of the stiffness ratio when parameters are optimized according to the method of maximum damping and H_∞ approach, respectively. Two observations can be made on this plot. One sees that α-controller always requires a higher actuator force than RFF especially when the stiffness ratio increases. In addition, the actuator force of RFF when its parameters are tuned based on H_∞ optimization is greater than that of RFF when its parameters are optimized based on the method of maximum damping. However, this is not the case for α-controller. For a vary low stiffness ratio $\frac{k_a}{k} << 0.1$, it slightly requires less actuator force when its parameters are optimized based on the method of maximum damping. It is the opposite for high value of the stiffness ratio $\frac{k_a}{k} >> 0.1$.

3.1.5 Stability and Robustness analysis

Stability analysis

It is always important to estimate the gain margin and the phase margin of a control system even if it is unconditionally stable like RFF. Enough margins could avoid an instability of the

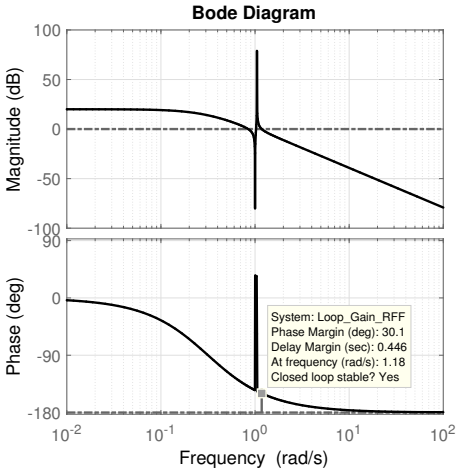

(a)

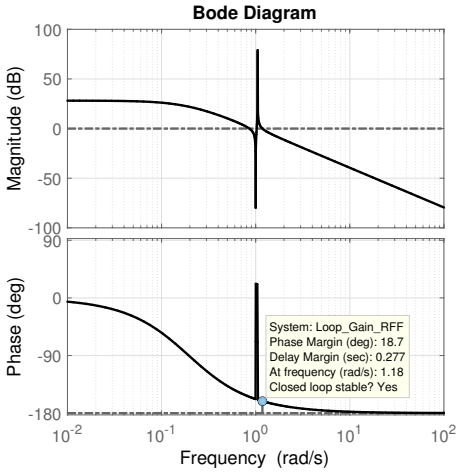

(b)

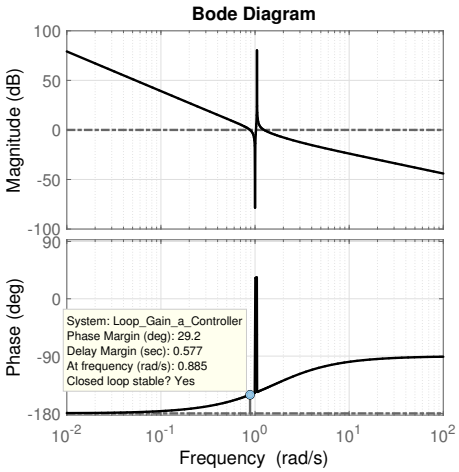

(c)

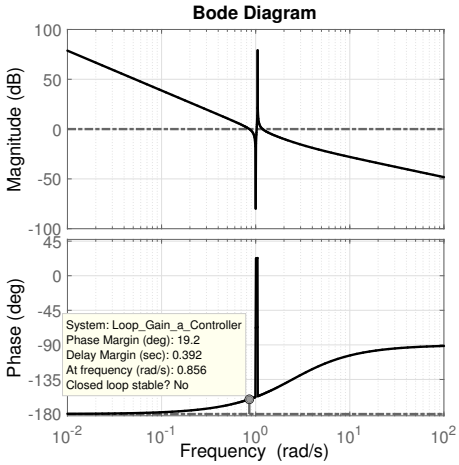

(d)

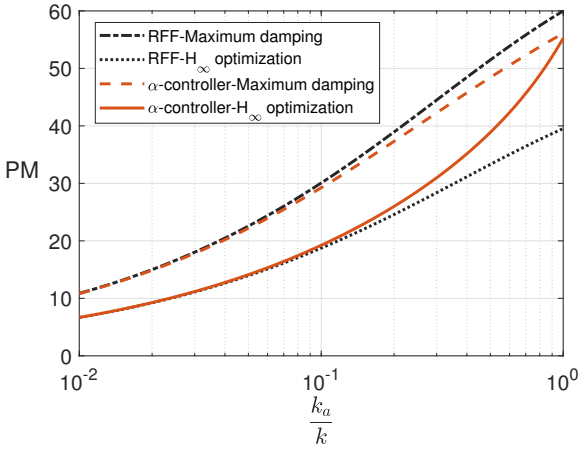

(e)

Figure 3.15: The bode diagram of the loop-gain ($G \times H$) when the parameters of RFF are tuned according to (a) the method of the maximum damping as well as (b) H_∞ optimization and when the parameters of α-controller are tuned according to (c) the method of the maximum damping as well as (d) H_∞ optimization. (e) Minimum phase margin with respect to the stiffness ratio when the parameters are set to their optimal values.

system in practical implementation. The bode diagrams of the loop-gain (i.e. $G \times H$) are shown in Figs. 3.15a and 3.15b when RFF is tuned according to the method of maximum damping and H_∞ optimization, respectively. The minimum stability margin is also highlighted in the figures. Clearly, the gain margin is infinity and the phase margin is 30.1° and 18.7° according to the method of maximum damping and H_∞ optimization, respectively. Furthermore, the loop-gain of the system when α-controller is implemented is shown in Figs. 3.15c and 3.15d when the parameters are optimized based on the maximum damping and the H_∞ methods, respectively. Like RFF, the gain margin is infinity. However, the minimum phase margin is 29.2° and 19.2° considering the method of maximum damping and H_∞ criterion, respectively. Those bode diagrams are obtained for a certain value of the stiffness ratio i.e. $\frac{k_a}{k} = 0.1$. The evolution of the minimum phase margin when the stiffness ratio $\frac{k_a}{k}$ is varied and the parameters of RFF and α-controller follow their optimal values is demonstrated in Fig. 3.15e. According to it, three important observations are made. First,

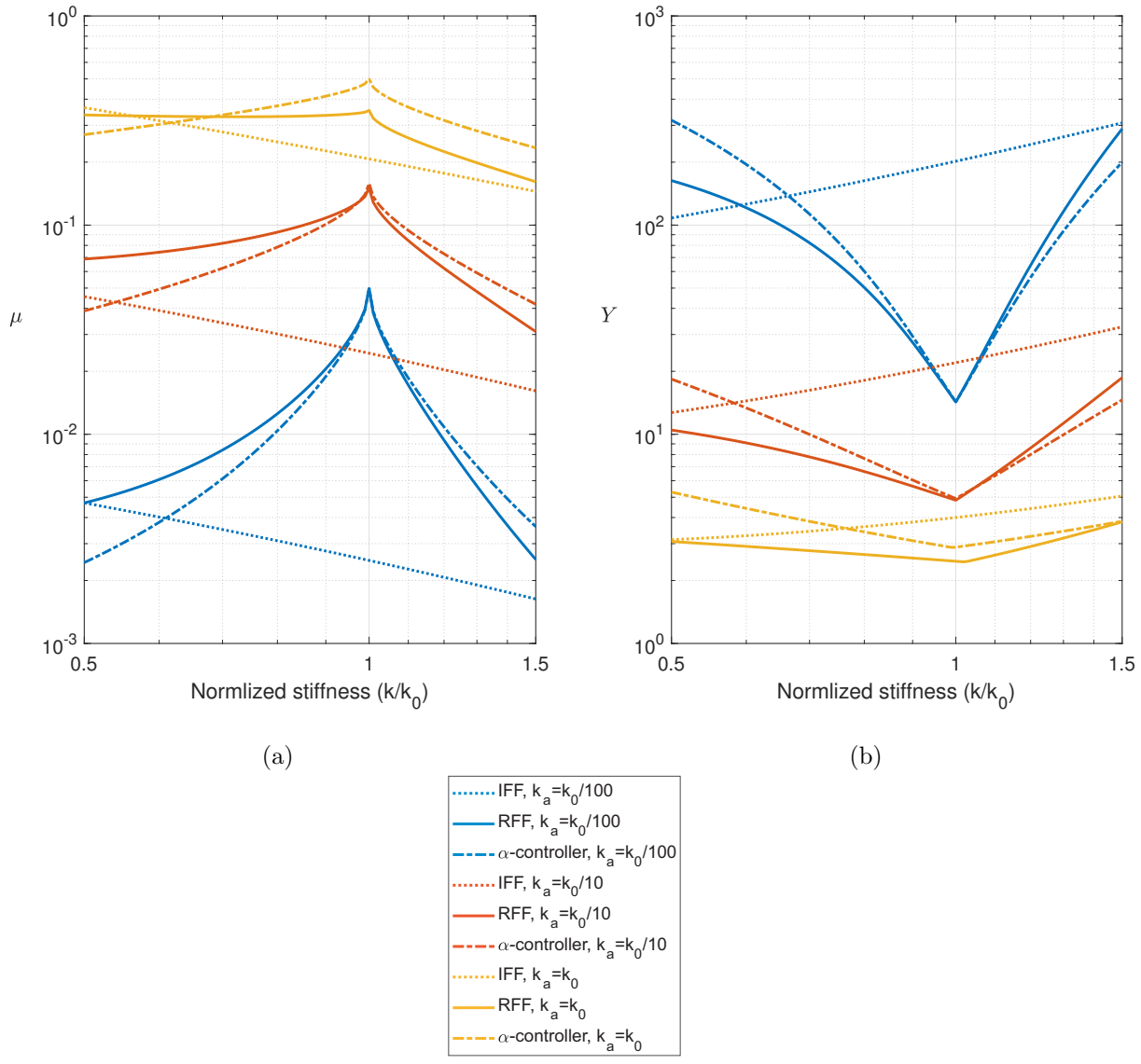

Figure 3.16: Under the variation of the stiffness k of the primary system while the parameters of the controller are kept constant at their optimal values for the specified stiffness ratios i.e. k_a/k_0 : $0.01, 0.1, 1$, (a) closed-loop damping coefficient μ of the performance index and (b) normalized maximum amplitude Y of the performance index with respect to the static response.

the method of maximum damping always offers a better phase margin than that of H_∞ approach. Furthermore, the minimum phase margin decreases by reducing the stiffness ratio. Noted that the classical IFF maintains an infinite gain margin and 90° phase margin for any value of the feedback gain. It can be concluded that the better control performance obtained by RFF or α-controller than IFF, as explained in Section 3.1.1, comes at the expense of a degradation in the phase margin. Moreover, Fig. 3.15e is connected to Figs. 3.8b and 3.11b. In Fig. 3.8b, it has been shown that α-controller gives a slightly better control performance in terms of the closed-loop damping ratio than RFF for high value of the stiffness ratio. This out-performance is reflected directly in the minimum phase margin shown in Fig. 3.15e. It is the other way around when the parameters are tuned according to H_∞ optimization. According to Figs. 3.11b and 3.15e, the better control performance provided by RFF in terms of the amplitude reduction comes at the price of a lower phase margin compared to that of α-controller.

Robustness analysis

What follows is a robustness study of IFF, α-controller, and RFF under the stiffness uncertainty. To check the robustness of the systems based on the method of maximum damping, the minimum damping ratio of the closed-loop system, named μ, is shown in Fig. 3.16a under the variation of the stiffness of the primary system k normalized with respect to the initial value $k = k_0 = 1$. In addition, the normalized maximum amplitude of the response with respect to its static response (i.e. $Y = (k + k_a)|\frac{x}{F_d}|_{max}$) is considered for the robustness analysis of the systems designed based on H_∞ optimization. Fig. 3.16b shows Y against $\frac{k}{k_0}$. In both figures, the robustness is evaluated for three different stiffness ratio $k_a/k_0 : 0.01, 0.1, 1$ while the corresponding optimal parameters of RFF, α-controller, and IFF are tuned for $k = k_0$ and kept constant. For $k < k_0$, it is interesting that the closed-loop damping μ realized by IFF started to increase and subsequently the maximum amplitude of response at the frequency of resonance decreases with respect to the static response. This is because the distance between pole and zero in the open-loop transfer function increases which subsequently leads to a higher control performance even if the feedback gain is constant. In addition, the robustness of RFF and α-controller are generally degraded for any changes in the stiffness of the primary system since the resonance of the control systems has been perfectly tuned for the initial stiffness k_0. It has been already shown in Figs. 3.5b and 3.12b that any changes in the tuning frequency of RFF ω_f can significantly affect the control performance. On the other hand, the robustness of RFF and α-controller depend on the stiffness ratio $\frac{k_a}{k_0}$ such that the degradation rate of the control performance decreases with increasing in the stiffness ratio $\frac{k_a}{k_0}$. It should be noted that despite the loss of efficiency under the variation of the stiffness (i.e. $\frac{k}{k_0} = [0.6, 1.5]$), the performance of RFF is still superior to that of IFF, which is an appealing feature of RFF. It can be also observed that RFF can tolerate a higher level of uncertainty than α-controller when $k < k_0$.

3.2 Positive position feedback control system

Positive position feedback is an attractive control law for the control of plants having no high frequency roll-off. The tuning of the parameters of the positive position feedback to obtain the desired closed-loop performance is quite challenging. We present a technique to design the positive position feedback controller with the optimal damping. The technique is demonstrated on a single degree-of-freedom system. The poles of the positive position feedback are tuned using the method of maximum damping, which states that the maximum damping is achieved when both closed-loop poles of the system are merged. The parameters of the positive position feedback are dependent on the desired target damping in the closed-loop system. However, arbitrary choice of target damping results in high response at the frequencies lower than the tuning frequency. The optimal value of the target damping is obtained by minimizing the H_2 norm of the closed-loop transfer function of the system. The influence of the various parameters of the positive position feedback on the

closedloop response of the system is also studied. Finally, the experiments are conducted to verify the effectiveness of the proposed technique.

3.2.1 Mathematical modeling and H_2 optimization

An undamped single degree-of-freedom (DOF) system with a mass m, and a stiffness k, is considered as the primary structure (Figure 3.17). It is excited by an external force f_d. The active control system consists of an absolute displacement sensor x, mounted on the mass, the PPF controller and an actuator f_a. The governing equations of the motion are written as:

$$m\ddot{x} + kx = f_d + f_a \tag{3.31a}$$

$$f_a = g_f u \tag{3.31b}$$

and the dynamics of the controller read:

$$\ddot{u} + 2\xi_f \omega_f \dot{u} + \omega_f^2 u = \omega_f^2 x \tag{3.32}$$

where u, ξ_f, ω_f and g_f are the control signal, the damping ratio, the frequency and gain of the controller, respectively. The above equations are normalized with respect to the dimensionless time $\tau = \omega_0 t$ where $\omega_0 = \sqrt{\frac{k}{m}}$ as:

$$x_1'' + x_1 = f + \beta x_2 \tag{3.33}$$

$$x_2'' + 2\xi\alpha x_2' + \alpha^2 x_2 = \alpha^2 x_1 \tag{3.34}$$

where the normalized parameters are considered as follow:

$$x_1(\tau) = x(t), x_2(\tau) = u(t), \Omega = \omega/\omega_0,$$

$$f = \frac{1}{k} f_d, \beta = \frac{1}{k} g_f, \alpha = \frac{\omega_f}{\omega_0}, \xi = \xi_f \tag{3.35}$$

By transforming Eqs. (3.33) and (3.34) to the Laplace domain, the transfer function of the closed-loop system from the normalized input f and normalized displacement of the mass x_1 can be derived as:

$$\frac{x_1}{f} = \frac{s^2 + 2\xi\alpha s + \alpha^2}{(s^2+1)(s^2 + 2\xi\alpha s + \alpha^2) - \alpha^2\beta} \tag{3.36}$$

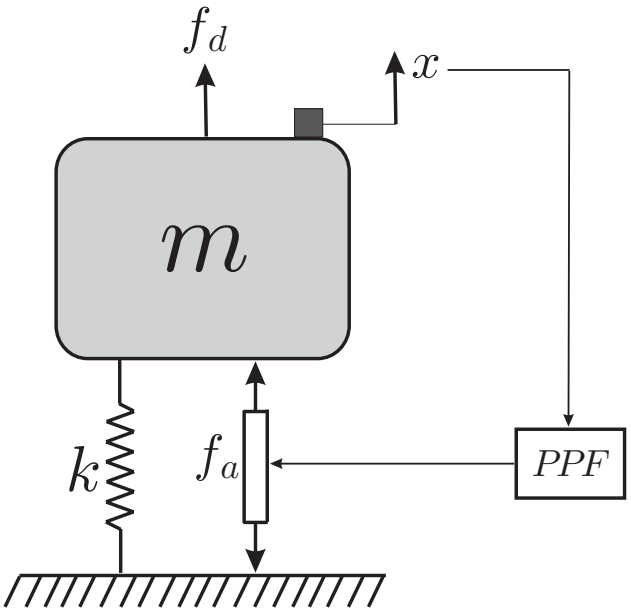

Figure 3.17: Schematic of the system under consideration consisting of single degree-of-freedom oscillator combined with the active control part

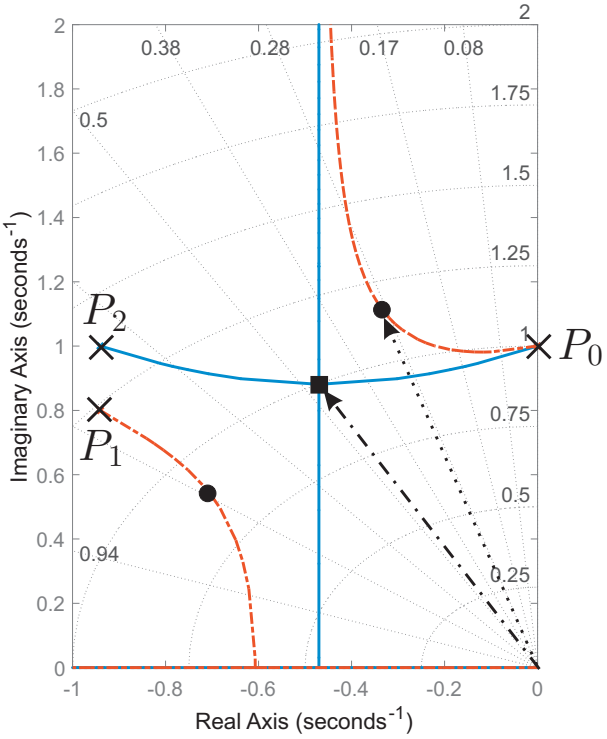

Figure 3.18: Root-locus curves for two different PPF controllers (P_0 is the pole of the primary system, •: closed-loop poles when the pole of the PPF is placed at P_1, ■: closed-loop poles when the pole of the PPF is placed at P_2).

where $s = j\Omega$ is the Laplace variable.
According to Eq. (3.36), the transfer function of the closed-loop system has two independent poles. The method of maximum damping is used to tune the pole of the PPF properly. It states that the best pole of the PPF is at the location where both resulting closed-loop poles have an equal damping ratio. This can be easily seen in Figure 3.18 for two different locations of the controller poles. The pole of the PPF is placed at P_1 at first attempt. The value of the closed-loop damping is about 30% as shown by the dotted arrow line. The right and the left loops are intersecting at one point when the pole of the PPF is modified to P_2. The corresponding damping ratio in this case increases to more than 45%. More details on this will be given in the Section 3. By considering ω_c and η as the frequency and damping ratio corresponding to the poles of the closed-loop system, the frequency response function of the closed-loop system can be simplified as:

$$\frac{x_1}{f} = \frac{s^2 + 2\xi\alpha s + \alpha^2}{(s^2 + 2\eta\gamma s + \gamma^2)^2} \tag{3.37}$$

where $\gamma = \omega_c/\omega_0$. The following equations are obtained by equating the polynomial coefficients of the denominator of the fraction on the right hand side of Eqs. (3.37) and (3.36).

$$4\eta\gamma = 2\alpha\xi \tag{3.38a}$$
$$(4\eta^2 + 2)\gamma^2 = (\alpha^2 + 1) \tag{3.38b}$$
$$4\eta\gamma^3 = 2\alpha\xi \tag{3.38c}$$
$$\gamma^4 = \alpha^2 - \alpha^2\beta \tag{3.38d}$$

Interestingly, from Eq. (3.38a) and Eq. (3.38c), it can be concluded that γ has to be equal to one in order to have unique and non-trivial solutions. This implies that the resonance frequency of the

closed-loop system should be the same as the resonance frequency of the primary system.

$$\omega_c = \omega_0 \tag{3.39}$$

The set of Eq. (3.38) is now simplified to three sub equations. However, there are still four unknown variables namely α, β, ξ and η. This results in an under-determined system of equations. This is because the number of PPF controllers which can provide the merged poles in the closed-loop response is not unique. In order to transfer the system of equations from under-determined to a determined system, one of the variable is set free. It is meaningful to consider the damping of the closed-loop response η as the free variable. In such a case, the controller parameters α, β and ξ are obtained for a particular value of η in such a way that the poles of the closed-loop response are merged. As a consequence, Table 3.3 lists the controller parameters as a function of the target damping, η.

Table 3.3: Parameters of the controller as a function of target closed-loop damping derived using maximum damping criterion

Parameters	Values
α	$\sqrt{4\eta^2+1}$
β	$\frac{4\eta^2}{4\eta^2+1}$
ξ	$\frac{2\eta}{\sqrt{4\eta^2+1}}$

Therefore, the closed-loop transfer function, $\frac{x_1}{f}$, can be rewritten as:

$$\frac{x_1}{f} = \frac{s^2 + 4\eta s + 4\eta^2 + 1}{(s^2 + 2\eta s + 1)^2} \tag{3.40}$$

At low frequency, the magnitude of $\frac{x_1}{f}$ can be approximated to $4\eta^2 + 1$. This means that the active damping comes at the price of the magnification of the response at low frequency, i.e. a degradation of the static stiffness. This implies that PPF controller softens the structure for a higher value of target damping. In the view of the vibration control design, this can be a major problem. The optimal value of the damping, which minimizes the energy of the system when subjected to Gaussian white noise input, is obtained using H_2 optimization.

The square of the H_2 norm of the closed-loop transfer function can be expressed as [72]:

$$||H||_2^2 = \int_{-\infty}^{\infty} S_0(\omega)\, |y|^2\, \omega_0 d\Omega \tag{3.41}$$

where $S_0(\omega)$ is the power spectral density of the input signal and y is the transfer function between the perturbation and the output of the system at a given location and in a given direction. In the present study, y corresponds to x_1/f. In the case of white noise excitation, $S_0(\omega)$ is constant as a function of frequency ($S_0(\omega) = S_0$). Therefore, the square of H_2 norm is simplified as:

$$||H||_2^2 = S_0\omega_0 \int_{-\infty}^{\infty} |y|^2\, d\Omega \tag{3.42}$$

The minimization of the variance of the response quantity is therefore equivalent to minimizing the H_2 norm of the transfer function:

$$PI = \int_{-\infty}^{\infty} |y|^2\, d\Omega \tag{3.43}$$

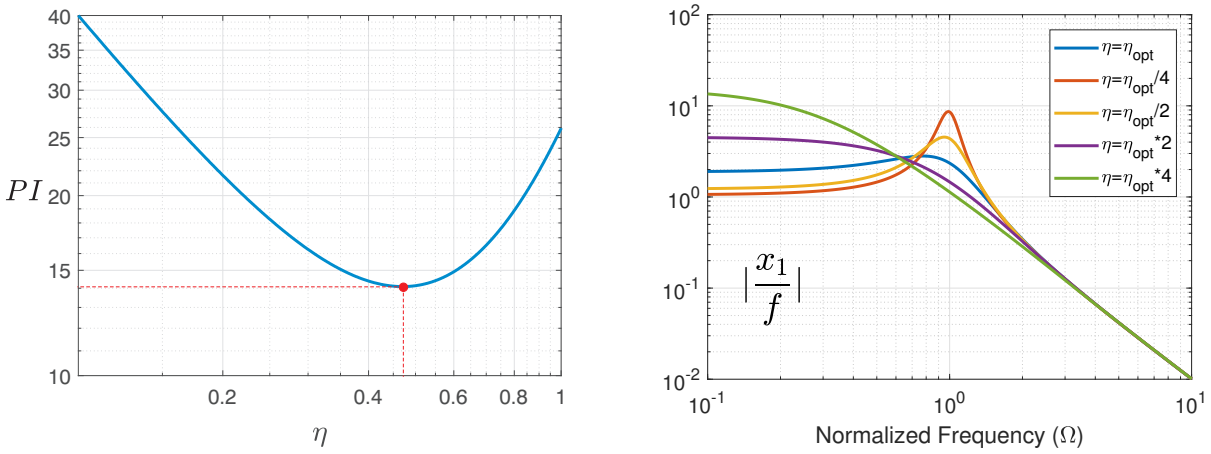

(a) (b)

Figure 3.19: a) H_2 norm of the controlled system for increasing the damping ratio of the closed-loop function η. b) Frequency response function of the the closed-loop system for different value of the target damping η

According to [72], the analytical solution to the integral (Eq. (3.43)) is in the form of:

$$\begin{aligned} PI &= \pi \frac{N_1 + N_2 + N_3 + N_4}{D_1} \\ N_1 &= (\frac{B_0^2}{C_0})(C_2C_3 - C_1C_4) \\ N_2 &= C_3(B_1^2 - 2B_0B_2) \\ N_3 &= C_1(B_2^2 - 2B_1B_3) \\ N_4 &= (\frac{B_3^2}{C_4})(C_1C_2 - C_0C_3) \\ D_1 &= C_1(C_2C_3 - C_1C_4) - C_0C_3^2 \end{aligned} \tag{3.44}$$

when $y(\Omega)$ is in general form as:

$$y(\Omega) = \frac{-B_3\Omega^3 - B_2\Omega^2 + B_1\Omega + B_0}{C_4\Omega^4 - C_3\Omega^3 - C_2\Omega^2 + C_1\Omega + C_0} \tag{3.45}$$

By equating Eq. (3.40) and the above equation to obtain B_i and C_i coefficients and using the analytical expression (Eq. (3.44)), the performance index can be defined as:

$$PI = \pi \frac{16\eta^4 + 12\eta^2 + 5}{4\eta} \tag{3.46}$$

Clearly, the optimal value of the damping at which the H_2 norm is minimized can be calculated by differentiating Eq. (3.46) with respect to the damping η, and equating the derivative to zero:

$$\frac{d(PI)}{d\eta} = \pi \frac{48\eta^4 + 12\eta^2 - 5}{4\eta^2} = 0 \tag{3.47}$$

which yields:

$$\eta_{opt} = 0.4702 \tag{3.48}$$

Interestingly, the optimal value of the target damping is constant for all primary systems. Figure 3.19a shows the H_2 norm (Eq. (3.42)) as a function of the closed-loop damping ratio η. Amplitude

reduction around the resonance frequency is responsible for the decreasing H_2 norm from 0 to 47.02% of the target damping ratio. However for higher damping ratio η, the increased magnitude at low frequency becomes more dominant than the amplitude reduction around the resonance. This can be seen in the frequency response shown in Figure 3.19b for five different values of the target damping defined as $\eta/\eta_{opt} : 1, 1/4, 1/2, 2, 4$.

3.2.2 Influence of the PPF parameters

In the following section, P_0 and P_1 are defined to be the pole of the primary system and the pole of the optimal PPF, respectively. The closed-loop pole when the optimal PPF is implemented is also shown by ■.

The damping ratio of the PPF (ξ)

Figure 3.20a shows the root-locus for various values of the damping ratio of the PPF (ξ). Here, the other parameters of the controller α and β are set to the optimal values. In this section, P_2 and P_3 are specified to be the poles of the PPF when $\xi = 0.5\xi_{opt}$ and $\xi = 2\xi_{opt}$, respectively. In addition, • and ▲ indicate the closed-loop poles when $\xi = 0.5\xi_{opt}$ and $\xi = 2\xi_{opt}$, respectively. The locus consists of two loops, starting respectively from the pole of the primary system and the pole of the PPF. One of the loops goes to real axis and the other one goes to infinity. If $\xi < \xi_{opt}$, both closed-loop poles have less damping ratio than for the optimal case. In this case, one pole has higher and the other one has lower frequency than the resonance frequency of the primary system.

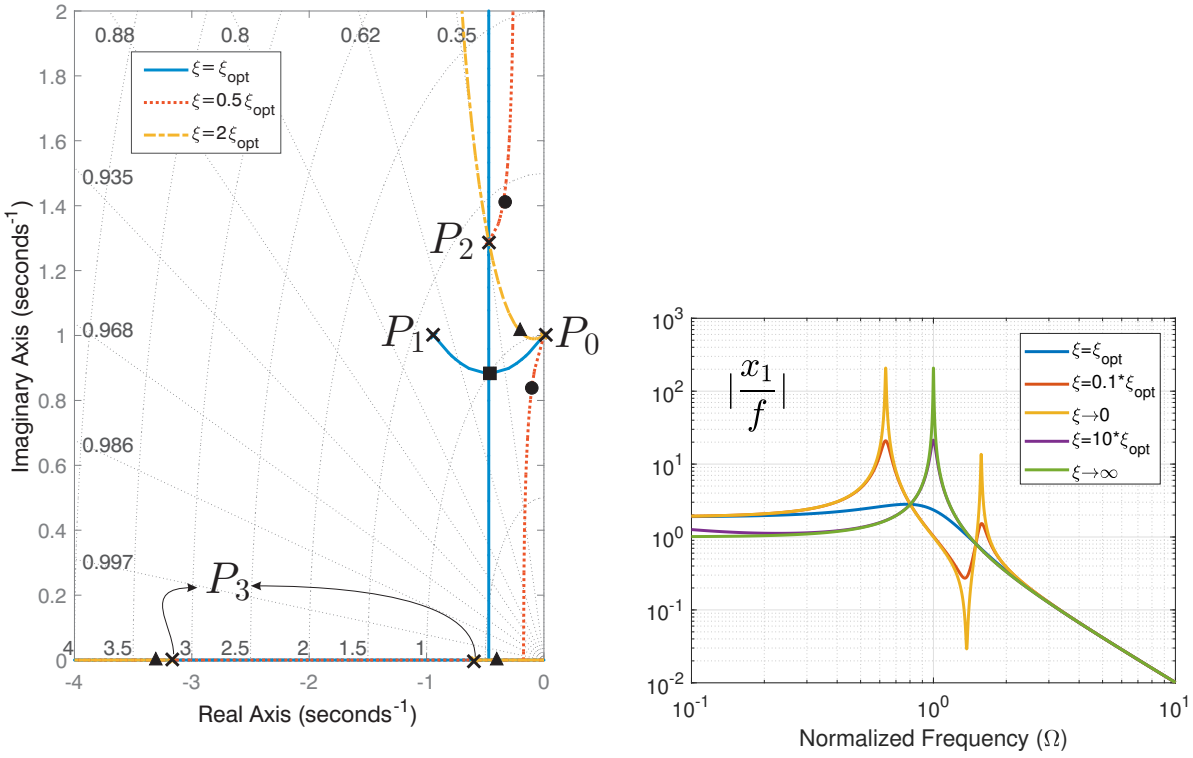

(a) (b)

Figure 3.20: a) Root-locus for three different values of the damping ratio ξ (P_0: pole of the primary system; P_1: pole of the PPF and ■: closed-loop poles when $\xi = \xi_{opt}$; P_2: pole of the PPF and •: closed-loop poles when $\xi = 0.5\xi_{opt}$; P_3: pole of the PPF and ▲: closed-loop poles when $\xi = 2\xi_{opt}$). b) Frequency response of the controlled system for different values of the damping ratio ξ

If $\xi > \xi_{opt}$, one pole is more damped than the other one. The heavily damped pole is placed close to the pole of the controller. Therefore, the pole/zero cancellation occurs because the zero of the closed-loop function (Eq. (3.36)) is the pole of the controller. As a consequence, the performance of the controller is degraded and especially it is no longer effective if $\xi \to \infty$. It is worth pointing out that the value of the H_2 norm for $\xi = 0.5\xi_{opt}$ and $\xi = 2\xi_{opt}$ is about 29% and 21% greater than the optimum one, respectively.
It is meaningful to examine the performance of the PPF on the frequency response for different values of the damping ratio ξ. Figure 3.20b shows the frequency response for five different damping ratios defined as $\xi/\xi_{opt} : 1, 0.1, 0, 10$ and ∞. One sees that all the curves are intersecting at two frequencies which are called fixed points. For the damping ratios lower than the optimal value, the primary resonance is transformed into one anti-resonance and two new resonances appear in the vicinity of the old one. An interesting point here is that the increased magnitude of the response at low frequencies disappears when the value of the damping increases ($\xi > \xi_{opt}$). Explicitly, the coupled system behaves like the primary system with no additional damping when $\xi \to \infty$.

The frequency of the PPF (α)

The root-locus plots for three different values of the frequency of PPF are compared in Figure 3.21a. In this case, the other control parameters (ξ and α) are set to the optimal values. In this case, P_2

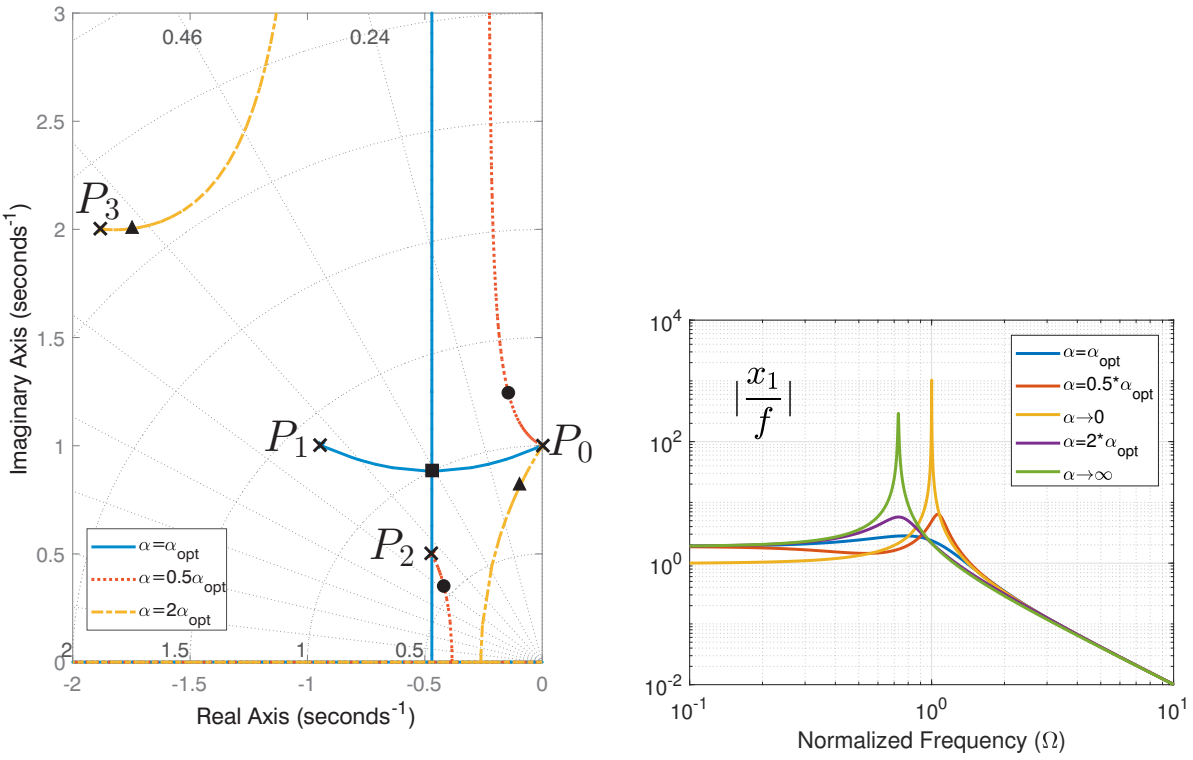

(a) (b)

Figure 3.21: a) Root-locus for three different values of the frequency of the PPF α (P_0: pole of the primary system; P_1: pole of the PPF and ■: closed-loop poles when $\alpha = \alpha_{opt}$; P_2: pole of the PPF and •: closed-loop poles when $\alpha = 0.5\alpha_{opt}$; P_3: pole of the PPF and ▲: closed-loop poles when $\alpha = 2\alpha_{opt}$). b) Frequency response of the controlled system for different values of the frequency of the PPF α.

and P_3 are ascertained to be the poles of the PPF when $\alpha = 0.5\alpha_{opt}$ and $\alpha = 2\alpha_{opt}$, respectively. Furthermore, • and ▲ demonstrate the closed-loop poles when $\alpha = 0.5\alpha_{opt}$ and $\alpha = 2\alpha_{opt}$, respectively. If $\alpha \neq \alpha_{opt}$, one of the closed-loop poles is more damped than the other one. The heavily damped pole is less effective than the other pole because of the pole/zero cancellation as discussed in section 3.2.2. It can be seen in Eq. (3.36) that if $\alpha \to 0$, the PPF could no longer add any damping to the system. Also, if $\alpha \to \infty$, the pole of the PPF becomes ineffective in the terms of adding damping to the system. However, the other pole moves on the branch which goes toward the origin. This modifies the frequency of the pole to a slightly lower value. It should be noted that the H_2 norm for $\alpha = 0.5\alpha_{opt}$ and $\alpha = 2\alpha_{opt}$ is 46% and 80% greater than the optimum one, respectively.

Figure 3.21b depicts the frequency response for five different values of α. The evidence of the performance degradation can be seen when $\alpha \to 0$. In this case, the controlled response has the same dynamic behavior as the primary system with no damping. Two important observations are made when the frequency of the controller is larger than its optimal value. First, no more degradation of the static stiffness can be observed in the low frequency response of the system. Second, it results in a dynamically softer system. It is because the controller behaves like a positive constant gain in this case. This constant value amplifies the feedback signal which is positively proportional to the displacement. Consequently, it reduces the stiffness and the resonance frequency of the structure.

The feedback gain (β)

It is worth pointing out that the system remains stable even if the changes in the damping ξ or the frequency α of the controller are significant. However, it is not the case for the feedback gain β. In order to check the stability, the Routh-Hurwitz stability criterion is used. For this purpose, consider A_0, A_1, A_2, A_3 and A_4 as the corresponding coefficients of Laplace variable in the denominator of Eq. (3.36) from s^0 to s^4, respectively. This criterion states that the poles of the Eq. (3.36) have negative real parts if and only if the following conditions are satisfied:

$$A_0, A_1, A_2, A_3, A_4 > 0 \tag{3.49a}$$

$$A_2A_3 - A_1A_4 > 0 \tag{3.49b}$$

$$A_1A_2A_3 - A_1^2A_4 - A_0A_3^2 > 0 \tag{3.49c}$$

It can be derived that the system is stable if and only if the feedback gain β is considered as:

$$0 < \beta < 1 \tag{3.50}$$

The designed optimal value of the feedback gain β_{opt} is equal to 0.4693 which ensures the stability of the system. The corresponding root-locus for three different values of the feedback gain are shown in Figure 3.22a. The damping ratio ξ and the frequency α are set to the optimal values. In this section, P_2 and P_3 are the poles of the PPF when $\beta = 0.5\beta_{opt}$ and $\beta = 2\beta_{opt}$, respectively. Moreover, • and ▲ show the closed-loop poles when $\beta = 0.5\beta_{opt}$ and $\beta = 2\beta_{opt}$, respectively. If $\beta < \beta_{opt}$, the heavily pole located closed to the pole of the controller becomes less effective because of the pole/zero cancellation explained in section 3.2.2. Especially, Eq. (3.36) evidences that, if $\beta \to 0$, the controller is no longer effective to increase the damping of the system. If $\beta > \beta_{opt}$, the heavily damped pole can improve the damping of the closed-loop response. However, this pole moves directly toward the origin which makes the system softer. The value of the H_2 norm for $\beta = 0.5\beta$ and $\beta = 2\beta$ increases 45% and 292% with respect to the optimum case, respectively. Another interesting result is shown in the frequency response of the controlled system (Figure 3.22b) for five different values of the feedback gain. The control effectiveness degrades in terms of the resonance peak by decreasing the feedback gain. The more vibration attenuation of the resonance peak comes at the expense of the increased static stiffness when $\beta \approx 1$. This has been already discussed as a major problem in the previous section.

3.2.3 Experimental validation

As shown in Figure 3.23, the experimental setup used to test the optimal proposed controller is a cantilever beam with the dimensions 455mm, 40mm and 3mm as length, width and thickness, respectively. The resonance of interest is the first bending mode of the beam. According to the first mode shape, the maximum displacement occurs at the free-end of the beam. Thus, a voice-coil actuator is placed there and an eddy-current sensor is fixed next to the actuator in order to measure the displacement motion. A *dSPACE MicroLabBox* is used for the purpose of both the data acquisition as well as control system. The whole control scheme is designed first inside the graphical *SIMULINK* environment of *MATLAB* and then compiled. The compiled file is downloaded onto the *ControlDesk* environment of *dSPACE* software, which is connected directly to the *MicroLabBox* hardware, to be executed in real time. The control scheme is updated at a sampling frequency of 10 kHz while the measured data is also recorded at the same sampling frequency. A current amplifier (ADD-45N) is used to drive the voice coil actuator.
Although the obtained formulas are strictly valid for an undamped primary system, they can fairly be used to specify the parameters of controllers for lightly damped structures as well. The beam shown in Figure 3.23 behaves like a lightly damped structure when the voice coil actuator is not mounted. The damping ratio in this case is 0.8%. However, it becomes 8% when the actuator is mounted. This is because of the dissipation of the energy caused by the eddy current inside of the electromagnetic transducer. A negative damping force is implemented actively to compensate the undesired damping of the actuator. Displacement feedback with a positive derivative operator is

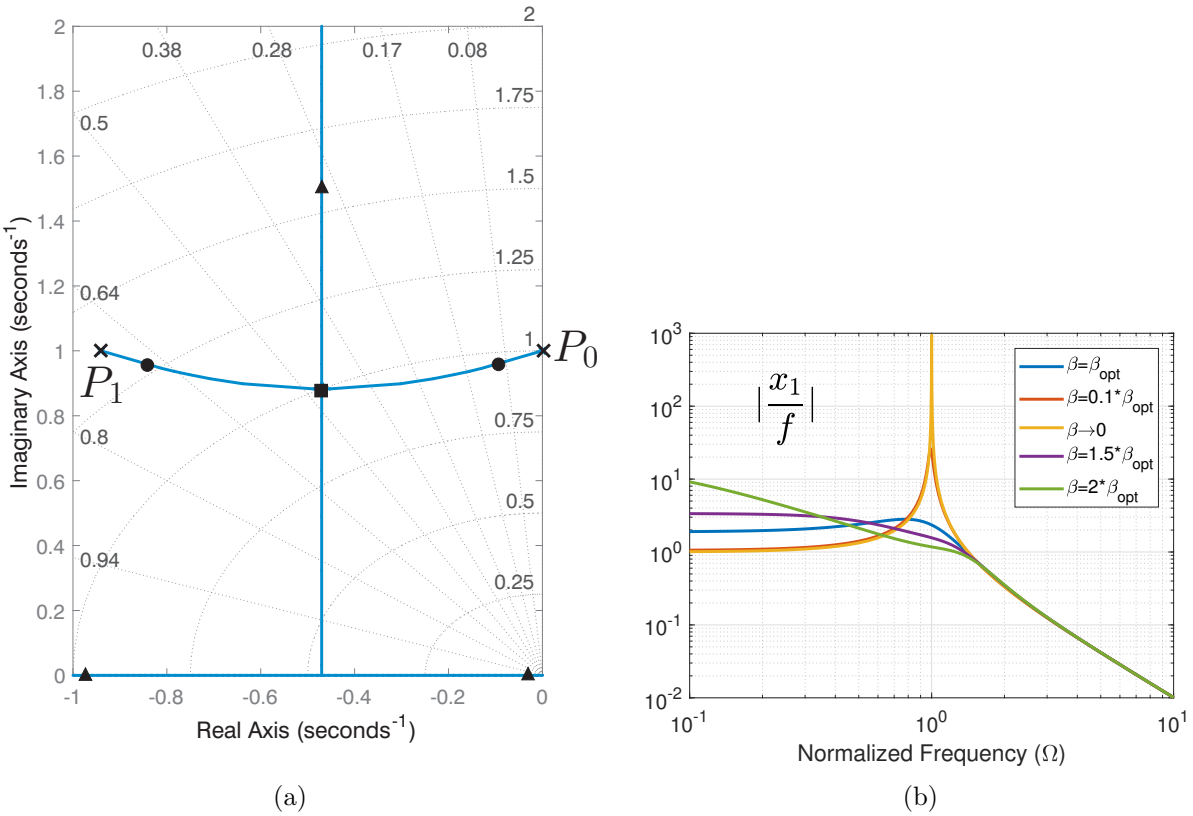

(a) (b)

Figure 3.22: a) Root-locus for three different values of the feedback gain β (P_0: pole of the primary system; P_1: pole of the PPF; ■: closed-loop poles when $\beta = \beta_{opt}$; •: closed-loop poles when $\beta = 0.5\beta_{opt}$; ▲: closed-loop poles when $\beta = 2\beta_{opt}$). b) Frequency response of the controlled system for different values of the feedback gain β.

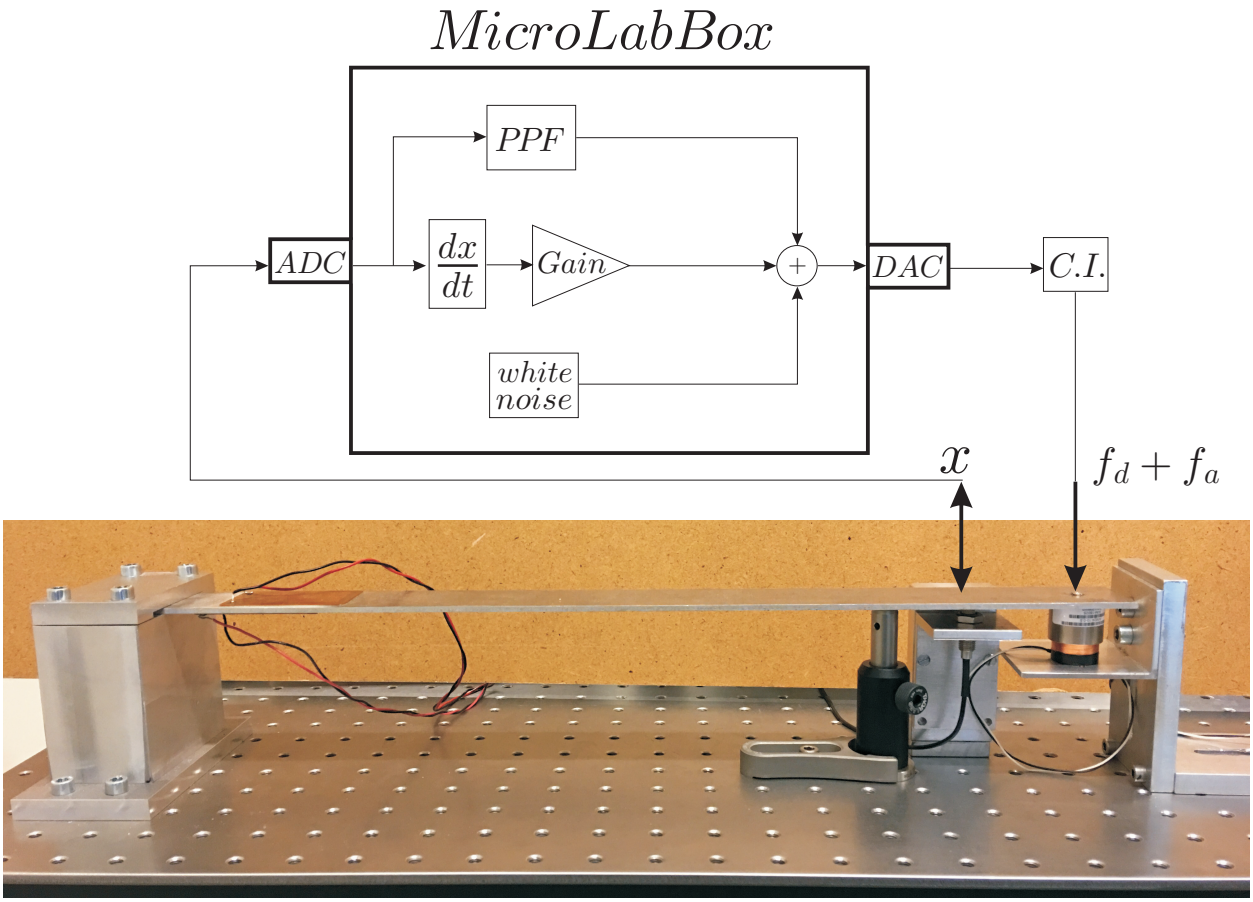

Figure 3.23: Picture of the test benchmark used to test the proposed controller. Cantilever beam, clamped at one end, and equipped with an voice coil actuator and eddy-current sensor at the other end. (ADC: Analog-to-Digital-Converter; DAC: Digital-to-Analog-Converter; C.I.: Current-Injector)

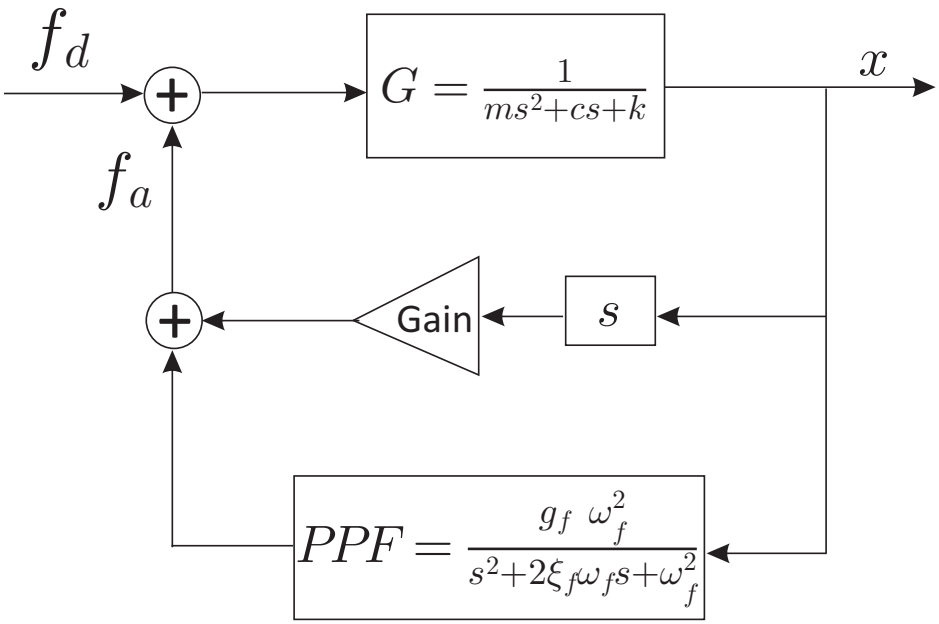

Figure 3.24: Block diagram of the controller architecture (G: primary system; c: damping of the primary system)

used to add the negative damping in the system. The configuration scheme for the experimental study is shown in Figure 3.23. A white noise generator is employed to excite the structure from 0Hz to 100Hz by using the same actuator in the setup. It also applies the control force. Furthermore, simulations are carried out to examine the performance of the designed optimal controller numerically. The block diagram of the control architecture is shown in Figure 3.24.

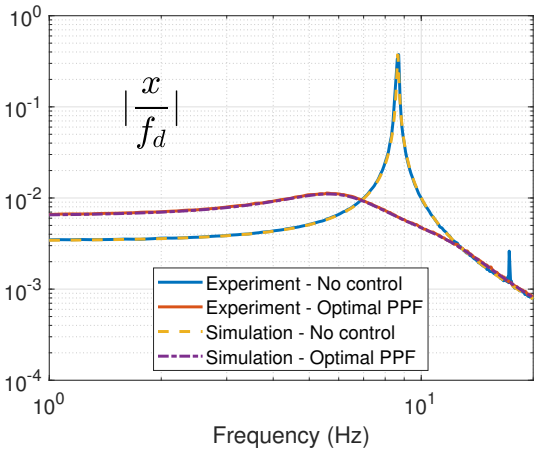

Figure 3.25: Frequency response functions from the disturbance force to the displacement of the eddy current sensor obtained from the simulations and experiments with and without optimal PPF controller

Figure 3.25 shows the frequency response functions from the disturbance force (the white noise) to the displacement of the eddy-current sensor. It also compares the simulations and the experiments without control and with the optimal PPF. The value of the stiffness and the resonance obtained by matching one degree of freedom system to the experimental result are 295N/m and 8.65Hz, respectively. The effective structural damping after addition of negative damping is found to be 0.45%. An interesting observation is that the experimental result shows a good agreement with the simulations. The maximum amplitude of the coupled response is reduced almost 33 times

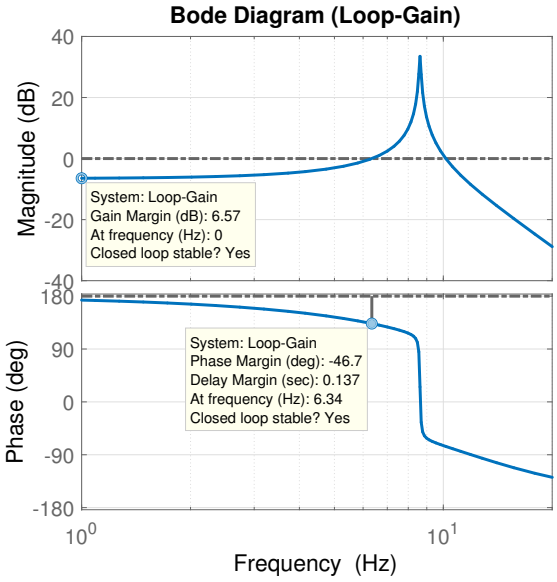

Figure 3.26: Bode diagram of the loop-gain for the designed optimal PPF controller (○: gain margin; ●: phase margin)

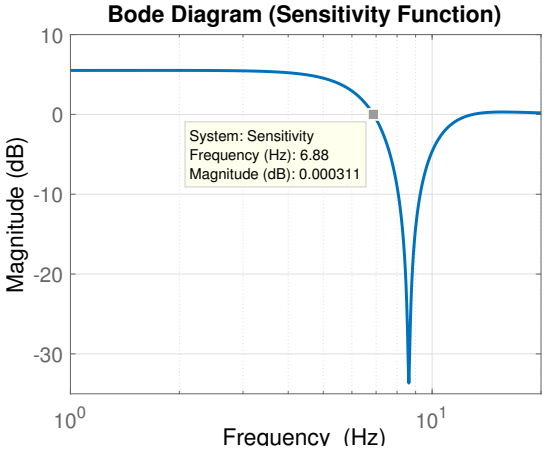

Figure 3.27: Sensitivity curve for the designed optimal PPF controller (■: Crossover)

compared to the primary system. Also, amplification of the response at low frequencies is only about 88% which is not detrimental. As an important consequence, the result confirms that the obtained formula is also valid for lightly damped structure.
To better understand the stability of the closed-loop system in terms of the phase and the gain margins, the loop-gain of the system is also shown in Figure 3.26. It is obtained by multiplying the primary system to the designed optimal controller (Eq. (3.51a)). According to the figure 3.26, the phase is always bounded between 180deg and -180deg in the entire frequency range, which ensures the stability of the closed-loop system. The gain margin is 6.57dB obtained when the phase touches the 180deg at 0Hz. Furthermore, the minimum phase margin is -46.7deg where the magnitude of response touches the 0dB line.

$$Loop - Gain : -G \times PPF \tag{3.51a}$$

$$Sensitivity : \frac{1}{1 - G \times PPF} \tag{3.51b}$$

The sensitivity function (Eq. (3.51b) is also depicted in Figure 3.27. As it is expected, the controller amplifies the disturbance of the system below the crossover frequency i.e. when the magnitude of response intersects the 0dB line. This leads to increasing the static stiffness of the system. After the crossover frequency, the controller reduces the disturbance especially around the resonance frequency where the maximum reduction occurs. At high frequency, the controller is no longer effective.

3.3 Nonlinear Positive Position Feedback (NPPF)

Appendix B investigates the potential of using a nonlinear positive position feedback controller (NPPF) for vibration mitigation of a Duffing oscillator. The proposed controller is designed based on the principle of similarity which states that anti-vibration devices should be governed by the same equations as those of the host structure. Closed-form expressions for the H_∞ optimal control parameters that minimize the maximal response of the structure are firstly derived for the linear positive position feedback (LPPF) controller and then extended to the nonlinear counterpart. The harmonic balance method is employed to approximate the analytical solutions. Numerical simulations are presented to show the performance of LPPF and NPFF. In this section, experimental tests are performed to validate the proposed control strategy.

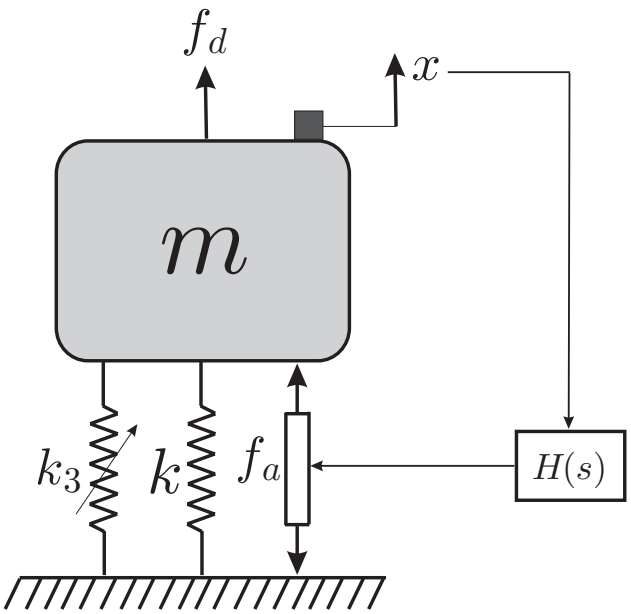

Figure 3.28: The scheme of the system under consideration

3.3.1 A review of modeling and H_∞ optimization

The system under investigation is shown in Figure 3.28. The structure is modeled as an undamped single degree of freedom system, defined through a lumped mass m, a linear spring k, and a cubic spring k_3 . It is excited by a harmonic force $f_d = F_d cos(\omega t)$. A force actuator is placed in parallel to the passive mount. The control loop is implemented by feeding the displacement of the lumped mass m through the nonlinear controller $H(x)$ to drive the actuator. The governing equations of the system read:

$$m\ddot{x} + kx + k_3x^3 = F_d cos(\omega t) + f_a \tag{3.52}$$

$$f_a = g_f H(x) \tag{3.53}$$

where f_a is the actuating force proportional to the driving signal, g_f represents the feedback gain and $H(x)$ is the nonlinear controller. The NPPF controller is designed based on the principle of similarity, and consequently a cubic term is included in the linear PPF controller, yielding:

$$\ddot{u} + 2\xi_f\omega_f\dot{u} + \omega_f^2 u + \kappa u^3 = x \tag{3.54}$$

where $u = h(x)$, ξ_f, ω_f and κ are controller parameters. In order to come to a more general formulation, the following parameters are introduced to normalize the system's governing equations:

$$\tau = \omega_0 t, \omega_0 = \sqrt{\frac{k}{m}}, \alpha = \frac{\omega_f}{\omega_0}, \beta = \frac{g_f}{k\omega_0^2}, y_1 = \frac{kx}{F_d}, y2 = \frac{k\omega_1^2 u}{F_d}, \delta = \frac{k_3 F_d^2}{k^3}, \mu = \frac{\kappa k}{k_3\omega_0^6} \tag{3.55}$$

The equations of motion with normalized parameters can then be written as:

$$y_1'' + y_1 + \delta y_1^3 - g y_2 = cos(\Omega\tau) \tag{3.56}$$

$$y_2'' + 2\alpha\mu y_2' + \mu^2 y_2 + \delta\beta y_2^3 = y_1 \tag{3.57}$$

where Ω is the normalized frequency defined as $\Omega = \frac{\omega}{\omega_0}$. It is shown that the forcing amplitude appears only in the expression of the nonlinear coefficients. The H_∞ optimization criterion is employed to optimize the controller $H(x)$ aiming to minimize the maximum magnitude of the frequency response of the system under consideration. In this context, the magnitude of the normalized driving point receptance $|y_1|$ is taken as the performance index. The optimal parameters of the controller are listed in Table 3.4. They are obtained as a function of the normalized feedback gain β. Appendix B presents more detail for the derivation of optimal parameters.

Table 3.4: Optimal parameters of NPPF

Parameters	Values
ξ_{opt}	$\sqrt{\frac{3\beta}{4(2-\beta)}}$
α_{opt}	1
μ_{opt}	$2\beta - \frac{9}{16}\beta^2 + O(\beta^3)$

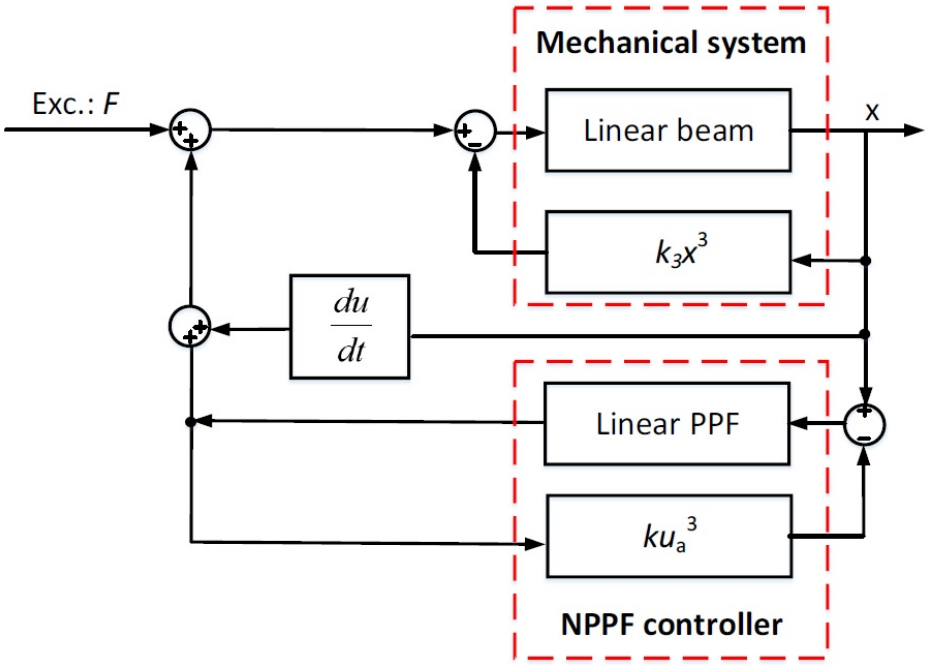

Figure 3.29: The configuration scheme for the experimental study.

3.3.2 Experimental validation

The same experimental setup as the one used in Section 3.2.3 is used here to validate the LPPF and NPPF controllers. However, the cantilever beam is dynamically a linear system. As for the nonlinear cubic spring of the Duffing oscillator, it was realized in an artificial way by feeding back the tip displacement of the cantilever beam through a cubic function to drive the voice coil actuator. The nonlinear cubic stiffness k_3 was therefore artificially set to 2×10^8 N/m^3. With this configuration, it is also possible to simulate nonlinear forces for other applications by applying the corresponding force profiles to the actuator. The configuration scheme for the experimental study is depicted in Figure 3.29. As seen, the input signal applied to the voice coil actuator comprises four contributions: (i) the disturbance force, (ii) the cubic spring force, (iii) the negative damping force which was set to $g_{neg} = 0.6$, and (iv) the control force. It is noted that the control force delivered by the NPPF controller is calculated in a way similar to that for implementing the 'artificial' Duffing oscillator, where the output of the LPPF compensator is fed through a cubic function and then negatively superposed with the displacement signal (sensor output) in order to form the corresponding nonlinear input signal for the LPPF compensator.

Experimental results in a linear regime of motion

The first set of experiments was conducted to test the validity of the optimal control parameters for the LPPF controller. The cubic branches in Fig. 7 for the primary Duffing oscillator and the NPPF controller were deactivated such that the system dynamically behaves in a linear fashion. During

the tests, a white noise signal was applied to excite the beam in the vicinity of its first bending motion at 8.6 Hz. The duration of the measurement was set to 200 s. Figure 3.30a plots the transfer function between the disturbance force and the measured tip displacement, where the parameter ξ is varied from 1/100 to 100 times the theoretical optimum value. In this case, the other parameters of controller such as $\alpha_{opt} = 1$, and $\beta = 0.05$ are kept constant. Figure 3.30b investigates the effect of the feedback gain β on the frequency response of the driving point receptance, where the parameters ξ and α were set to their optimal values as given in Table 3.4. As seen, the obtained experimental results are in accordance with the theoretical analysis shown in Appendix B. The parameters of the LPPF controller can be tuned to minimize the maximum response of one structural mode in a fashion analogous to that of TMDs. The effectiveness of the LPPF controller at the optimal tuning is also verified to be dependent upon the feedback gain. However, as it was already emphasized in Appendix B, the price to pay for this superior performance is the amplification of the response at low frequency. This is because the LPPF controller turns to a proportional controller at low frequency where its control effectiveness is to reduce the effective stiffness of the system thus leading to the low frequency amplification side effect. Figure 3.30a and Figure 3.30b are to be compared with Figure B.1 and Figure B.2, respectively.

Experimental results in nonlinear regime of motion

The potential of the LPPF and NPPF controllers for damping the Duffing oscillator is experimentally explored in this section. A sine sweep signal is applied as the disturbance to excite the beam. The sine sweep is bounded between 4Hz and 15Hz with a sweeping rate of 0.02Hz/s.
The control effectiveness of the LPPF controller for vibration mitigation of the Duffing oscillator is examined first. Figure 3.31a plots the time history of the tip displacement normalized to the level of the excitation force which is varied from 4 to 16.5 mN, while Figure 3.31b depicts the envelope of the normalized response which thus can be equivalently considered as the driving point receptance, hereafter also referred to as the experimental performance index. Note that the corresponding normalized nonlinear coefficient δ for different levels of the excitation force can be calculated according to Eq. (3.55). As can be seen, the observed experimental results agree well with the theoretical analysis shown in Appendix B, that is, the LPPF controller is only effective for weakly nonlinear systems. In addition, a jump phenomenon associated with positive cubic springs is experimentally observed which indicates the existence of the fold bifurcations of the system motion.

Next, the validity of the nonlinear control gain μ is experimentally examined by repeating the same tests as conducted for Figure B.3, where the coefficient of the cubic term of the NPPF controller κ is varied over a range from 1/4 to 4 times the theoretical optimum value. The optimal value of κ is equal to $\kappa_{opt} = 1.8283 \times 10^{15}$ and its dimensionless counterpart is $\mu = \mu_{opt} = 0.099$. The corresponding experimental results are shown in Figure 3.32, which again agree well with the theoretical analysis i.e. the resonance peaks of equal amplitude are obtained with the derived optimal setting of κ.

The control performance of the LPPF and NPPF controllers is experimentally compared for the same feedback gain $g_f = 39000$ (normalised gain $\beta = 0.05$) and the excitation level $F_d = 16.5$mN ($\delta = 0.003$), which is shown Figure 3.33. It can be seen that the detuned control performance with the LPPF controller in terms of the H_∞ norm is retrieved by the NPPF controller as predicted in Figure B.3b.

The investigation of the NPPF controller is continued with different levels of the excitation force ranging from 8 to 27 mN. The experimental results are presented in Figure 3.34a and 3.34b. It can be seen that the control performance with the NPPF controller is maintained for a larger range of excitation force amplitudes compared to the LPPF controller (the corresponding dimensionless nonlinear coefficient is still equal to $\mu_{opt} = 0.099$). However, when the disturbance was increased

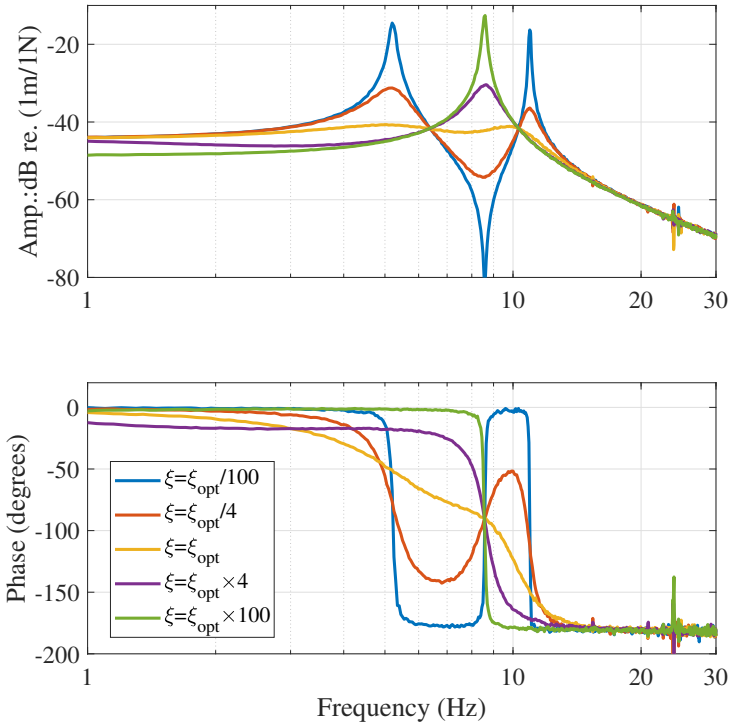

(a)

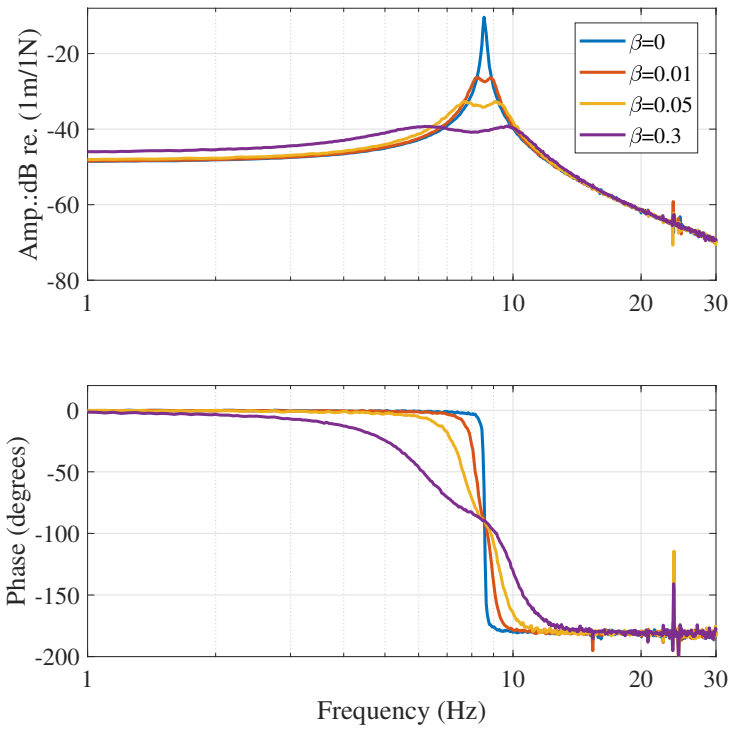

(b)

Figure 3.30: a) The frequency response of deriving point receptance for different values of the damping ratio ξ when the LPPF controller is applied. b) The frequency response of deriving point receptance for different values of the feedback gain β when the LPPF controller is applied.

to 27 mN, the response of the system is modulated around 10 Hz, which indicates that system might fall into the regime of quasiperiodic motions. In order to confirm this, a sinusoidal excitation was used instead, where the frequency varied from 9.7 Hz to 10.2 Hz and the amplitude was set to 27 mN. The evolution of the time series of the normalised system response with respect to the excitation frequency is shown in Figure 3.34c. It can be seen that the system response below 10.1 Hz exhibits more than one frequency component under a sinusoidal excitation, which is a clear sign of the quasiperiodic oscillations. At 10.2 Hz, the maximum amplitude of the system response suddenly decreases and the quasiperiodic motion disappears. Back to the experimental performance index curve associated with this excitation amplitude as shown in Figure 3.34b, the results observed can be understood as follows: the system response follows the main frequency response curve until the first Neimark-Sacker bifurcation point located at around 9.7 Hz, then it continues to undergo some quasiperiodic motions between 9.7 Hz and 10.1 Hz and finally the response jumps down to the main frequency response curve instead of continuing to approach the second Neimark-Sacker bifurcation point along the same branch. This trend corresponds well with the numerical investigation as shown in Figure B.4b for the case.

3.4 PPF vs Digital Shunt

In Section 2.4, it has been shown that an operational amplifier (OpAmp) is required for the implementation of the active control system. Since the OpAmp consumes the external energy for its operation, the power dissipation of the OpAmp has been derived accordingly (Eq. (2.33)). In addition, this power dissipation has been computed for the digital electromagnetic shunt.

In this section, the power dissipation of the OpAmp is obtained when the positive position feedback (PPF) as an active control system is implemented following the same procedure explained in

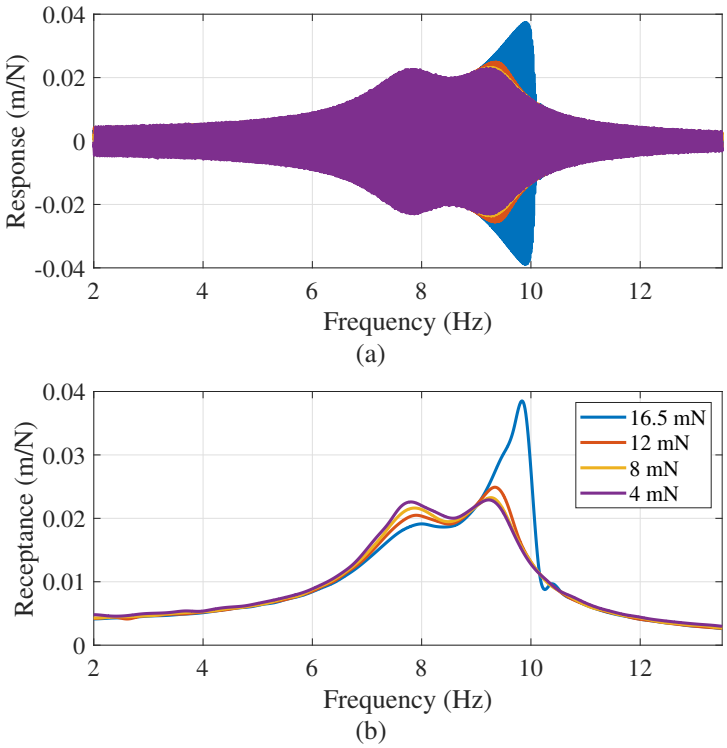

Figure 3.31: Measurement of the tip displacement normalised to the excitation level when the LPPF controller is applied: (a) time history signals and (b) its envelope

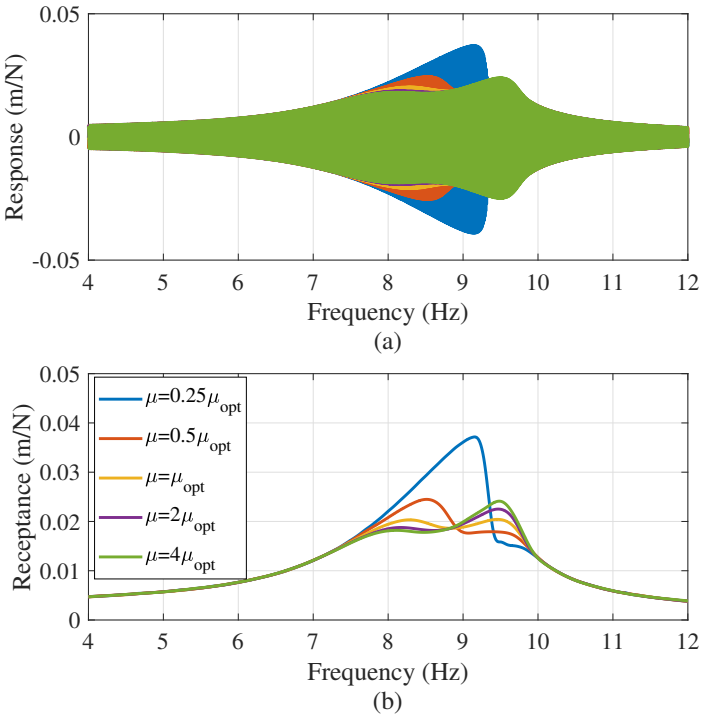

Figure 3.32: Measurement of the tip displacement normalised to the excitation level when the NPPF controller with different values of is applied: (a) time history signals and (b) its envelope

,

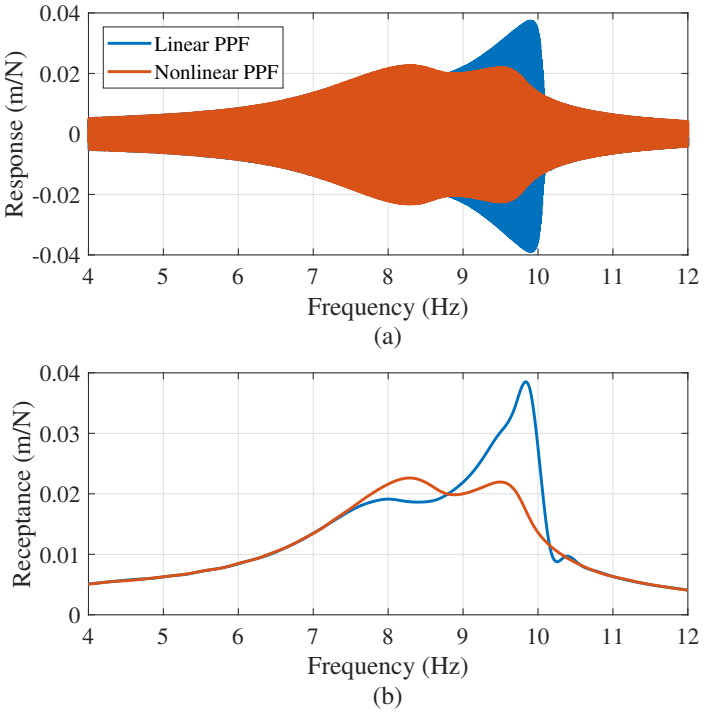

Figure 3.33: Experimental performance index obtained with the optimal LPPF and NPPF controllers for the same level of excitation $F_d = 16.5$ mN and feedback gain $g_f = 39000$

Section 2.4. In doing so, the force and velocity of the system can be written in frequency domain according to the set of Eq. 3.31 as follow:

$$f_a(j\omega) = -\frac{g_f \omega_f^2}{-\omega^2 + 2\xi_f \omega_f j\omega + \omega_f^2} G(j\omega) f_d(j\omega) \tag{3.58}$$

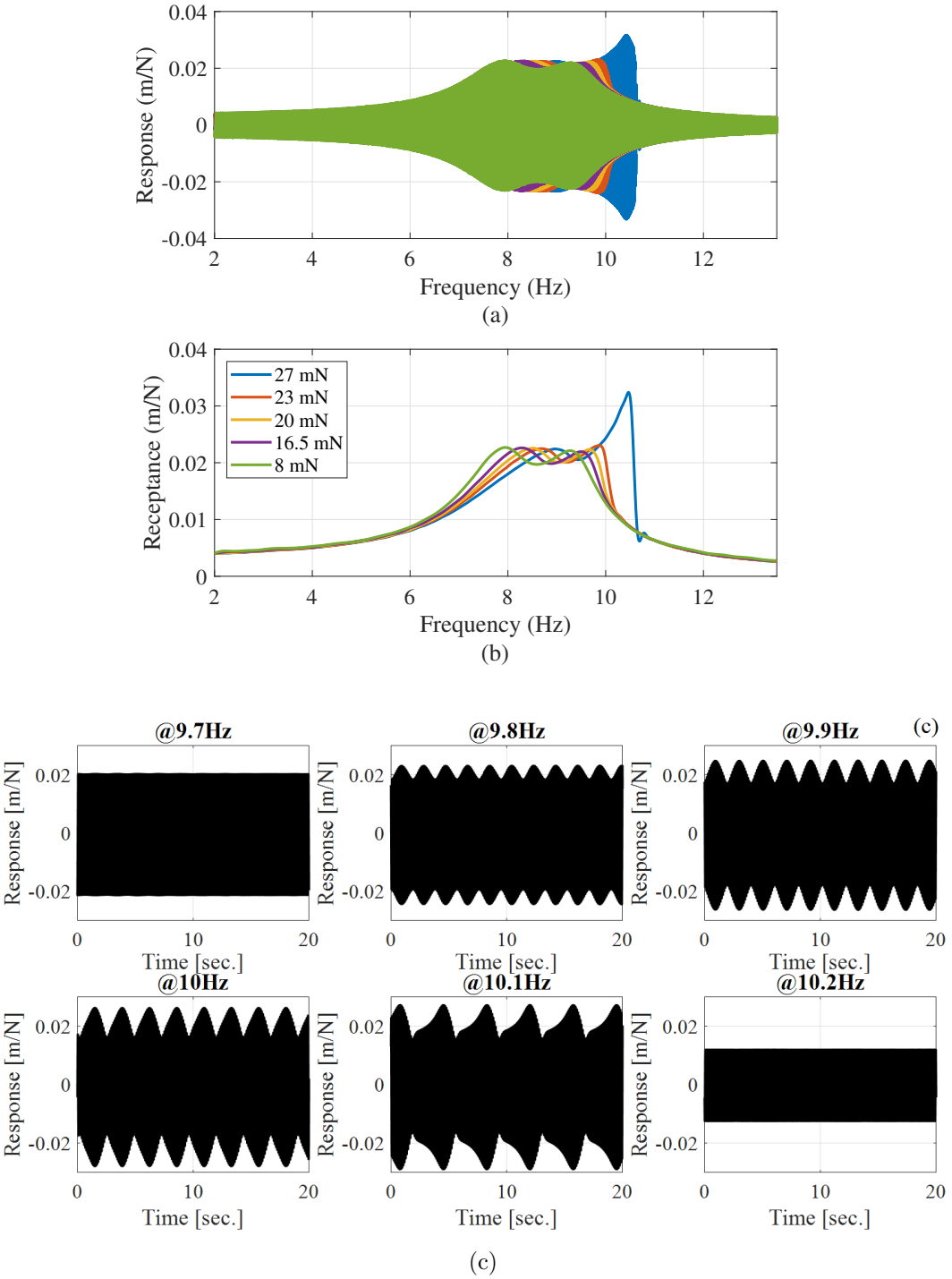

Figure 3.34: Measurement of the tip displacement normalised to the excitation level when the optimal NPPF controller is applied: (a) time history signals, (b) its envelope and (c) time series with sinusoidal excitations

and

$$v(j\omega) = (j\omega)G(j\omega)f_d(j\omega) \tag{3.59}$$

where $G(j\omega)$ is:

$$G(j\omega) = \frac{x(j\omega)}{f_d(j\omega)} = \frac{-\omega^2 + 2\xi_f\omega_f j\omega + \omega_f^2}{(-m\omega^2 + cj\omega + k)(-\omega^2 + 2\xi_f\omega_f j\omega + \omega_f^2) - g_f\omega_f^2} \tag{3.60}$$

By substituting Eqs. (3.58)-(3.61) into Eq. 2.33, the active power of the OpAmp can be written in frequency domain after some manipulations as:

$$\begin{aligned} P_{OpAmp}(j\omega) = 2I_Q V_{CC} &+ \left| \frac{g_f\omega_f^2}{(-m\omega^2 + cj\omega + k)(-\omega^2 + 2\xi_f\omega_f j\omega + \omega_f^2) - g_f\omega_f^2} \right| \cdot |f_d(j\omega)|^2 \\ &+ \frac{1}{2} \left| \frac{\sqrt{2\xi_f g_f \omega_f}\omega_f\omega}{(-m\omega^2 + cj\omega + k)(-\omega^2 + 2\xi_f\omega_f j\omega + \omega_f^2) - g_f\omega_f^2} \right|^2 \cdot |f_d(j\omega)|^2 \end{aligned} \tag{3.61}$$

Figure 3.35 compares the active power of the OpAmp when the digital electromagnetic shunt and

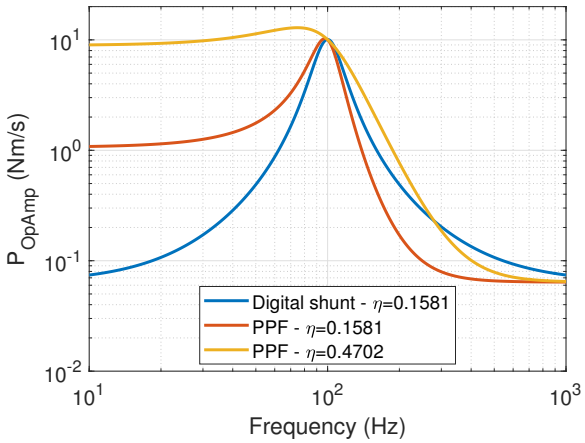

Figure 3.35: Power dissipation of the the electromagnetic transducer when it is shunted with RC elements and when it is used as active control system for PPF.

PPF are implemented. Note that the parameters of the primary system (i.e. mass m and stiffness k) and the OpAmp are tuned to the values which have been chosen in Section 2.4. According to the Table 3.3, it is possible to tune the parameters of PPF such that the desired closed loop damping ratio is realized. In the figure, PPF has been tuned first such that the same closed loop damping ratio as the one obtained by electromagnetic shunt damper (i.e. $\eta = 0.1581$) is achieved. In this case, low frequency power for PPF is higher than that of the digital shunt. While after the resonance frequency, the power for PPF starts to decrease faster than that of the digital shunt. The key parameter to reveal the differnec between the power dissipation of the PPF compared to

Table 3.5: H_2 norm of the active power of the OpAmp when different active control strategies are implemented.

Controller	H_2 norm
Digital shunt, η=0.1581	994.55
PPF, η=0.1581	994.45
PPF, η=0.4702	2955.30

that of the digital shunt is the H_2 norm of the power. The H_2 norm mainly shows the power dissipation over the frequency range of intereset ($\pm\infty$). However, the H_2 norm possess an infinite value since the high frequency power has a nonzero value due to the quiescent power. By neglecting the quiescent power, the H_2 norm of the power is listed in Table 3.5. From the table, it is interesting to conclude that H_2 norm of the power is almost the same when the PPF and the digital shunt are tuned to realize the same closed loop damping ratio.

Although $\eta = 0.1581$ is the maximum closed loop damping ratio that can be achieved by the shunt system, PPF can still provide a higher value of the closed loop damping ratio. In Section 3.2.1, the optimal PPF has been defined as the one that provides $\eta = 0.4702$ closed loop damping ratio. Figure 3.35 shows the power dissipation for the optimal PPF. In this case, both low and high frequency power of the PPF are higher than that of the digital shunt. The H_2 norm of the power is also computed in this case and shown in the Table 3.5. The H_2 norm of the power is much higher than that of the digital shunt system. It should be also noted that the active power, when PPF is applied, is always positive in the whole frequency range showing that the power is dissipative.

3.5 Conclusions

In Section 3.1, a new resonant control system based on the force feedback configuration, named RFF, has been proposed and optimally designed to overcome performance limitations of the classical integral-force-feedback (IFF) when a resonance of a structure is targeted. It has been shown that RFF can be seen as an active realization of an inerter-spring-damping (ISD) system which can also be used for vibration damping, vibration isolation and suspension systems in different applications. Then, its equivalent mass, damping and stiffness have been derived. The controller possess three unknown parameters including the damping coefficient, tuning frequency and feedback gain. These parameters have been optimized according to two different tuning laws i.e. the method of maximum damping and H_∞ optimization. The closed-form expressions of these parameters have been obtained for a single-degree-of-freedom (SDOF) system. It has been shown that second order filter as the control law in the feedback loop from the force sensor to the force actuator leads to the design of an absorber with an excellent performance. Therefore, the control authority of a target mode can be significantly increased using RFF in comparison to IFF. In addition, since α-controller is another control law to offer a better control performance than the classical IFF, the performance of RFF has been evaluated in comparison to that of α-controller in terms of the vibration mitigation and the control effort. Although both techniques provide almost the same control authority, RFF requires less actuator force than α-controller. Therefore, RFF can be considered as a low energy consumption technique to enhance the vibration mitigation of flexible structures using force feedback. It has been also demonstrated in the robustness analysis that RFF brings a superior performance to that of IFF up to almost 50% changes in the stiffness of the primary system while IFF can tolerate a higher level of uncertainty.

It is interesting to note that RFF can be used for vibration isolation under a base excitation. This is proposed as future work.

In Section 3.2, an easy to implement optimal positive position feedback (PPF) control procedure has been proposed, analyzed and experimentally implemented. The trade-off between the amplitude reduction at the resonance frequency and the amplification of response at the frequencies lower than tuning frequency has been highlighted and used to optimize the PPF controller. To this end, the position of the poles of the closed-loop system is determined using the maximum damping criterion. Then, the parameters of the PPF controller could be expressed as a function of the target damping in the closed-loop system. The optimal value of the target damping was evaluated using H_2 optimization. It has also been demonstrated, through sensitivity analysis, that the performance

of the system degrades if the parameters of the PPF are deviated from the optimal values. From the experimental tests, we could observe that the obtained formula can be effective to calculate the optimal PPF for lightly damped primary system as well. The extension of the proposed optimal PPF to damping several modes of the primary structure is the topic of future work.

In Section 3.3, the nonlinear PPF (NPPF) controller was used to damp the vibration of Duffing oscillator, experimentally. Note that the proposed NPPF is numerically introduced and studied in Appendix B. In fact, the NPPF controller is built upon the classical linear PPF (LPPF) controller but a cubic term is included according to the principle of similarity. It is shown that the LPPF controller is only effective for weakly nonlinear systems in terms of vibration mitigation, while the NPPF controller could hold the control efficiency for a relatively large range of forcing amplitudes. However, the NPPF controller can be also detuned for very strongly nonlinear regimes. This is because inherently nonlinear dynamical instabilities such as isolas cannot be eliminated by the proposed controller.

In Section 3.4, the power dissipation of the OpAmp when PPF is implemented has been studied. The power dissipation has been derived first and then, the corresponding result has been compared to that of the digital shunt. The main interesting conclusion was the fact the higher control performance realized by active control systems comes at the price of higher level of power consumption required for the OpAmp.

Chapter 4

Hybrid Vibration Control

Contents

It has been shown in Chapter 2 that shunting electromagnetic devices with electrical networks can be used to damp vibrations. These absorbers have however limitations that restrict the control performance, i.e., the total damping of the system and robustness versus parameter variations. On the other hand, the electromagnetic devices are widely used in active control techniques as an actuator. Although the active control systems, as presented in Chapter 3, can provide the high control performance, they mainly suffer from two main shortcomings: 1) the power consumption required for the actuator and 2) the lack of fail-safe property which means the ability of providing vibration damping even when the external power source is distorted. Therefore, it is proposed to design hybrid control systems by combining the passive electromagnetic shunt damper with the active control systems. The objectives of the hybrid control system are: 1) increasing the control performance compared to the passive one, 2) reducing the power consumption compared to the active one, and 3) possessing a fail-safe behavior. In this chapter, two different configurations for the hybridization of the passive resonant shunt with an active control are considered (Figure 4.1). In the first configuration shown in Figure 4.1a, the electromagnetic transducer is connected in series with RC elements and an active voltage source. The active voltage source is proportional to the velocity of the structure. The total voltage across the transducer (V) is then obtained by the summation of the active input voltage (V_{in}) and the voltage across the RLC circuit. Furthermore in the second configuration shown in Figure 4.1b, the electromagnetic transducer is connected in series with the RC circuit, and the active current source is in parallel with the shunting elements. Considering this configuration, the total current flowing in the transducer (I_t) is given by the algebraic sum of the input active current (I_{in}) and the current flowing inside the RC shunt circuit ($I_s = \dot{q}$) like $I_t = I_s - I_{in}$.

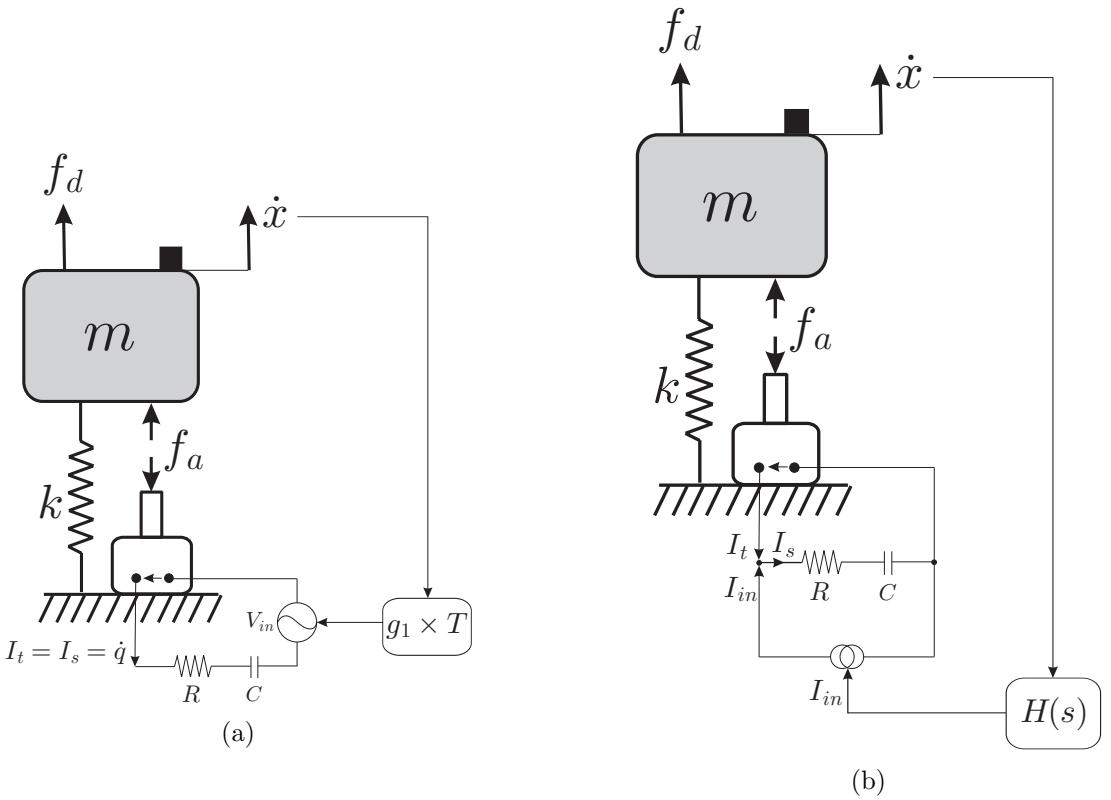

Figure 4.1: Schematic of a SDOF oscillator attached to an hybrid control system consisting of an electromagnetic transducer connected to the passive RC shunt (a) in series with an active voltage source and (b) in parallel with an active current source

4.1 Hybrid electromagnetic shunt damper with an active voltage source

Considering the active voltage source, the electrical portion of the governing equations are modified as:

$$L\ddot{q} + R\dot{q} + \frac{1}{C}q + V_{in} = T\dot{x} \tag{4.1a}$$

$$V_{in} = -g_1 T\dot{x} \tag{4.1b}$$

By substituting Eq. (4.1b) into Eq. (4.1a), it can be seen that the active voltage source directly affects the effective coupling constant of the transducer. Therefore, the actuator force is proportional to the current with a new coupling constant T^*. It is assumed that the transducer is ideal and there is a perfect balance between the electrical energy and the mechanical energy which means that there is no energy to be stored in the transducer [25]. According to the energy conservation principle [83], the variation of the stored energy is the sum of the external power input and the internal power generation. This concept can be written for the electromagnetic transducer in the presence of the active voltage source when there is no shunt as:

$$dW = Vdq + f_a dx = T(1 + g_1)\frac{dx}{dt}idt + T^* idx \tag{4.2}$$

where d and W are the differential operator and the stored energy, respectively. By equating the above equation to zero, T^* can be obtained as:

$$T^* = T(1 + g_1) \tag{4.3}$$

Figure 4.2 shows the root locus of the system, shunted with a RC circuit and the active voltage source in series, for the variation of feedback gain g_1. One sees that the system is stable because the poles are always placed in the left half plane of the locus for all values of the feedback gain g_1. The locus has two complex poles and two zeros at the origin. By increasing the value of the feedback gain g_1, one pole goes toward the origin and the other one goes to infinity. It makes the system have two different resonances in the vicinity of the primary ones with the lower values of the damping than the damping of the passive control system. According to the Eq. (2.10b), the optimal values of the resistance R is proportional to the coupling constant of the transducer. Considering the new constant of the transducer (Eq. (4.3)), the optimal value of the resistance can be modified as:

$$R^*_{opt} = \frac{2T}{\sqrt{kC_{opt}}}(1 + g_1) \tag{4.4}$$

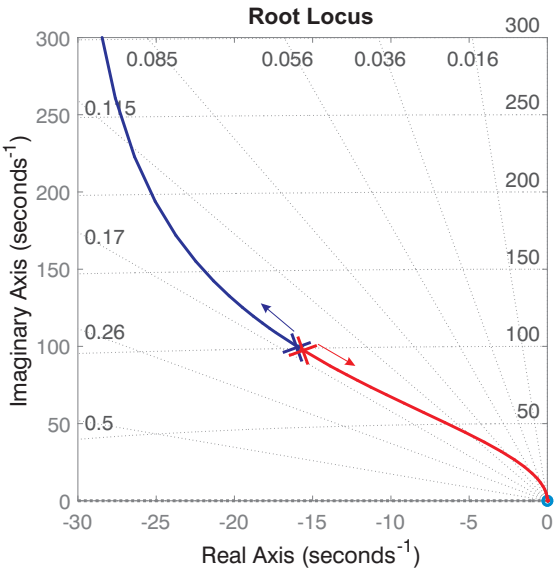

Figure 4.2: Root-locus of the system shunted with RC circuit combined with active voltage source

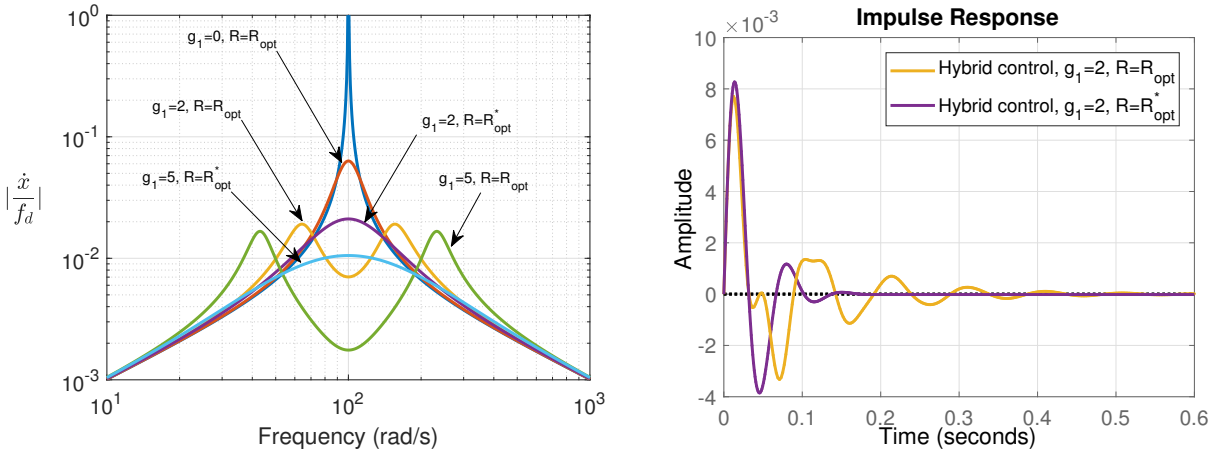

(a) (b)

Figure 4.3: With the application of the passive control system combined with the active voltage source, (a) the frequency response of the system for different values of the feedback gain g_1 as well as the resistance R and (b) the impulse response with and without the correction of the resistance R

Figure 4.3a compares the frequency response of the system with the passive control system combined with the active voltage source for two different values of the feedback gain g_1. For each value of g_1, the result is shown with and without correction of the resistance R according to Eq. (4.4) and Eq. (2.10b), respectively. By updating the value of the resistance in this case, more energy can be dissipated in the resistor which leads to increase the damping of the system. A larger value of resistance is required by the application of the active voltage source than the purely passive system. In order to have a fail-safe and optimum design, the value of resistance should be changed to the lower one when the active control is turned off. For a specific value of the feedback gain g_1, the impulse response is shown in Figure 4.3b when the value of the resistance R is modified based on Eq. (4.4). It can be seen that the exponential time-decay rate is maximized by updating the value of the resistance.

Similar studies have been already published for piezoelectric transducers when an active control is used to enhance the electromechanical coupling constant and subsequently improve significantly the passive piezoelectric shunt damping [10, 55, 58].

4.2 Hybrid electromagnetic shunt damper with an active current source

In the previous section, we could see that the performance is increased when the resistance of the passive shunt elements changes in proportion to the enhanced coupling constant. In this case (i.e. increased value of the resistor), the system has a weak fail-safe behavior because the passive control system is not optimally tuned when the active voltage source is turned off. More details on the performance degradation of the passive control system in terms of both magnitude of response and time decay rate can be seen in Figure 2.4 when a higher value of the resistance is chosen. What follows is the study of the hybrid control system using an active current source.

The equations of motion with the application of the active current source read:

$$m\ddot{x} + kx = f_d + f_a \tag{4.5a}$$

$$f_a = -TI_t = -T(\dot{q} + I_{in}) \tag{4.5b}$$

$$V = L(\ddot{q} + \dot{I}_{in}) + R\dot{q} + \frac{1}{C}q = T\dot{x} \tag{4.5c}$$

The transfer function of the system from the active current (I_{in}) to the velocity of the mass ($\dot{x}$) is obtained as:

$$G(s) = \frac{\dot{x}}{I_{in}} = \frac{T(Rs + \frac{1}{C})}{(ms^2 + k)(Ls^2 + Rs + \frac{1}{C}) + T^2 s^2} \tag{4.6}$$

The root locus of the system i.e. $G(s)H(s)$ when direct velocity feedback ($H(s) = -\frac{g_2}{T}$) is used as the active control law is shown in Figure 4.4a for the variation of the feedback gain. It can be seen that even for low gains, the root locus passes through the imaginary axis and can create instabilities. This is due to the absence of a zero between the pole of the passive shunt damper and the primary pole of the structure which are placed right next to each other. A simple alternative control law is proposed to ensure the stability of the closed loop system. The controller is still using the absolute velocity of mass, however, the filter is now defined as:

$$H(s) = -g_2 \frac{Ls^2 + Rs + \frac{1}{C}}{T(Rs + \frac{1}{C})} \tag{4.7}$$

The real pole of the controller cancels the zero of the loop gain ($G(s)H(s)$) and the pair of complex zeros interacts with the pole of the system. The system is unconditionally stable by the application

of the active current source because the closed-loop poles are always in the left half plane. Notice that, in order to avoid a constant component in the feedback loop, a high pass filter at very low frequency and a low pass filter at very high frequency should be added to the controller. These filters do not change the controller behavior for the flexible modes. When the feedback gain g_2 is zero, both poles of the system are placed right at the same locations thanks to the optimally design of the passive control system (Chapter 2). By increasing the feedback gain, the closed-loop damping ratio also increases. One of the pole moves on the upper branch (green branch) and the other one moves on the lower branch (blue branch). According to the method of maximum damping, the optimal feedback gain g_2^{opt} can be obtained when the two loops are intersecting at point 'A' which is shown in Figure 4.4b. Considering $\lambda = g_2\omega_0/k$, the closed-loop transfer function from the normalized disturbance force f to the normalized velocity $\dot{x}_1$ is obtained as:

$$\frac{\dot{x}_1}{f} = \frac{s(s^2 + 2\sqrt{\beta}s + 1)}{(s^2 + \lambda s + 1)(s^2 + 2\sqrt{\beta}s + 1) + \beta s^2} \tag{4.8}$$

When the two poles of the system have the same damping μ and normalized resonance frequency δ, the closed-loop transfer function can be re-written as:

$$\frac{\dot{x}_1}{f} = \frac{s(s^2 + 2\sqrt{\beta}s + 1)}{(s^2 + 2\mu\delta s + \delta^2)^2} \tag{4.9}$$

The following equations are obtained by equating the polynomial coefficients of the denominator of the fraction on the right hand side of Eqs. (4.8) and (4.9):

$$4\mu\delta = 2\sqrt{\beta} + \lambda \tag{4.10a}$$

$$4\mu^2\delta^2 + 2\delta^2 = 2\sqrt{\beta}\lambda + \beta + 2 \tag{4.10b}$$

$$4\mu\delta^3 = 2\sqrt{\beta} + \lambda \tag{4.10c}$$

$$\delta^4 = 1 \tag{4.10d}$$

The optimal value of the normalized tuning frequency δ is obtained from Eq. (4.10d) as:

$$\delta_{opt} = 1 \tag{4.11}$$

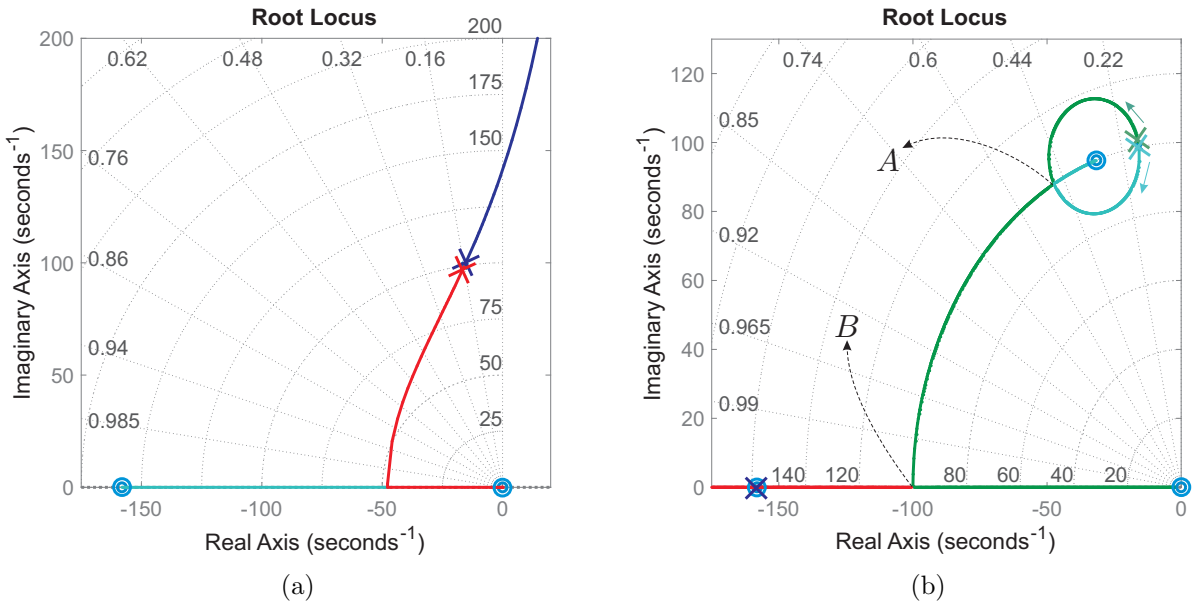

(a) (b)

Figure 4.4: Root-locus of the system shunted with RC circuit combined with active current source using (a) direct velocity feedback ($H(s) = \frac{g_2}{T}$) or (b) Eq. (4.7) for the active control law

which shows that the closed-loop system has the same resonance frequency as the resonance frequency of the primary one. The optimal value of the normalized feedback gain can be realized by substituting the damping ratio μ obtained from Eq. (4.10a) and Eq. (4.11) into Eq. (4.10b):

$$\lambda_{opt} = 4\sqrt{\beta} \tag{4.12}$$

which yields:

$$g_2^{opt} = 4\frac{T}{\omega_0}\sqrt{\frac{k}{L}} \tag{4.13}$$

It should be mentioned that the parameters of the passive RC circuit do not change. This results in a perfect fail-safe behavior because the passive control system is still optimally tuned to provide η_{opt} damping when there is no active current in the actuator. Figure 4.5a compares the frequency response of the passive control system combined with the active current source for two different values of the feedback gain g_2. The optimal value is first used for the feedback gain $g_2^{opt} = 126.49$ (shown as point 'A' in Figure 4.4b) and then it is increased to $g_2 = 200$ when a closed-loop pole touches the real axis (shown as point 'B' in Figure 4.4b) and the other one merges with the zero. In this case, the zero cancels one of the poles and the other one adds damping to the system. This gain ($g_2^{opt*} = 200$) can be defined as the second optimal value. Although it might slightly improve the settling time (Figure 4.5b) in comparison with the one corresponding to the first optimal value, the power consumption will drastically increase (more details will be discussed in the next section) and the actuator might be saturated. For more than this value of the gain, the settling time is no longer minimized although it might realize lower magnitude of response than the magnitude of response obtained with the optimal values of the feedback gain. It should be mentioned that the active current source behaves like a direct-velocity-feedback (DVF) which is able to damp several modes as well. This topic is proposed for future studies.

In the present study, the ideal voltage and current sources have been considered to build the hybrid configurations. Basically, an ideal voltage source is supposed to have no internal impedance and an ideal current source is supposed to have an infinite internal impedance [84]. However, this is not the case for practical voltage and current sources. Therefore, the internal impedance of the sources can change the total impedance of the shunt when the active control is turned off. This may result in a problem in fail-safe behavior for practical implementation of the hybrid control system. This will be more discussed in the future works.

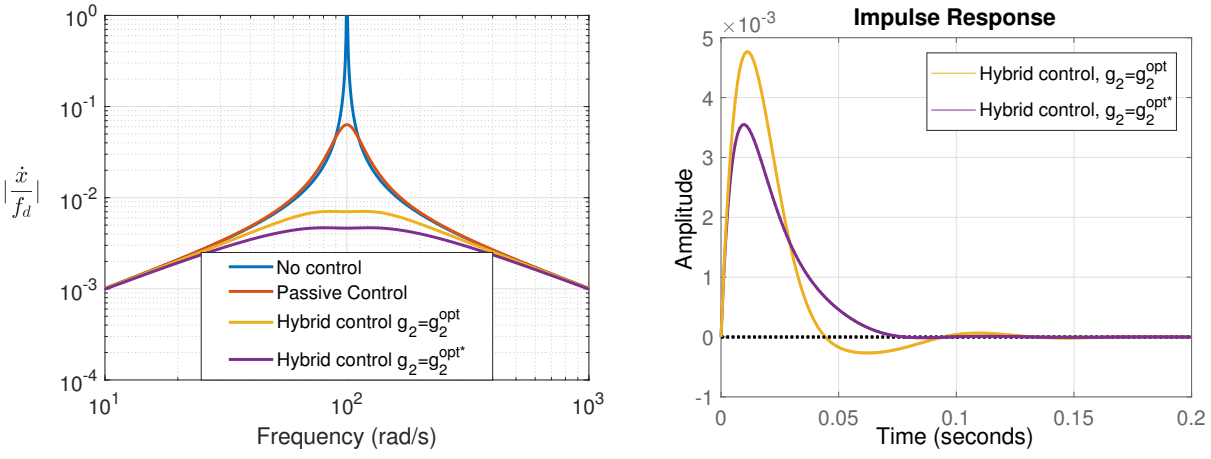

(a) (b)

Figure 4.5: With the application of the passive control system combined with the active current source, (a) the frequency response and (b) the impulse response of the system for two different values of the feedback gain g_2

4.3 Powerflow analysis

In the previous section, it has been shown that the hybrid control system can improve the control performance of the system in terms of the amplitude of response at the resonance frequency. A question may arise here is what is the main advantage of using a hybrid control system compared to a purely active control system. To answer this question, it is proposed to analyze the powerflow between the device and the primary structure due to the fact that an active control system requires an external power source for its operation. The power which flows at the interface of the structure and the actuator device can be written as:

$$P(s) = F_{aa}(j\omega) \times \dot{x}^*(j\omega) \tag{4.14}$$

where P, F_{aa} and $\dot{x}$ are the power, the control force applied by the active control system, and the velocity of the mass, respectively. The superscripts $''*''$ represents the complex conjugate transpose. The real part of P is called the active power which corresponds to the dissipative behavior and the imaginary part is named the reactive power which corresponds to the energy exchanging between the device and the structure [85]. The average active power P_{ac} and the reactive power P_{re} can be written as:

$$P_{ac} = \frac{1}{2}\Re(P(j\omega)) = \frac{f_d^2}{2}\Re(G_f(j\omega) \times G_{cl}(j\omega) \times G_{cl}^*(j\omega)) \tag{4.15a}$$

$$P_{re} = \frac{1}{2}\Im(P(j\omega)) = \frac{f_d^2}{2}\Im(G_f(j\omega) \times G_{cl}(j\omega) \times G_{cl}^*(j\omega)) \tag{4.15b}$$

where $G_f(j\omega)$ and $G_{cl}(j\omega)$ are the frequency response function from the velocity of the structure to the control force and the frequency response function from the input force disturbance to the velocity. The expressions for G_f and G_{cl} are given in Table 4.1. The result which is obtained in this section is based on a unit forcing amplitude.

Table 4.1: The expressions for G_f and G_{cl} for different control configurations

Parameters	G_{cl}	G_f
Hybrid control-Voltage source	$\frac{(j\omega)(-L\omega^2+(1+g_1)Rj\omega+\frac{1}{C})}{(-\omega^2+k)(-L\omega^2+(1+g_1)Rj\omega+\frac{1}{C})-(g_1+1)^2T^2\omega^2}$	$-\frac{g_1(g_1+2)T^2(j\omega)}{-L\omega^2+(1+g_1)Rj\omega+\frac{1}{C}}$
Hybrid control-Current source	$\frac{(j\omega)(-L\omega^2+Rj\omega+\frac{1}{C})}{(-\omega^2+g_2j\omega+k)(-L\omega^2+Rj\omega+\frac{1}{C})-T^2\omega^2}$	$-g_2$
DVF	$\frac{j\omega}{-\omega^2+g_3j\omega+k}$	$-g_3$

Considering a constant value of the closed-loop damping (=0.47), Figure 4.6a compares the active and reactive power for purely active control system and the hybrid control systems using active voltage source and current source, separately. The value of the closed-loop damping ratio (= 0.47) is chosen arbitrary to see the general trend of the active power and the reactive power through a large frequency range. DVF is used for the purely active control system. One can be observed that the active power for all configurations is always positive through the entire frequency range. This means that the device does not deliver energy in the system and it is *hyperstable*. The reactive power for the hybrid control system when the active voltage source is applied is positive before the resonance frequency and negative after that. This shows the amount of energy exchanged between the structure and the transducer. The total of positive and negative reactive power is almost zero.

Targeting any closed-loop damping, the integral of the active power through the entire frequency range changes for any configurations. Therefore, the mean square value of the active power is considered as the performance index. It can be written as [71]:

$$E[|P_{ac}|] = \int_{-\infty}^{\infty} \frac{|f_d(\omega)|^2}{2} |G_f(j\omega) \times G_{cl}(j\omega) \times G_{cl}^*(j\omega)| \, d\omega \tag{4.16}$$

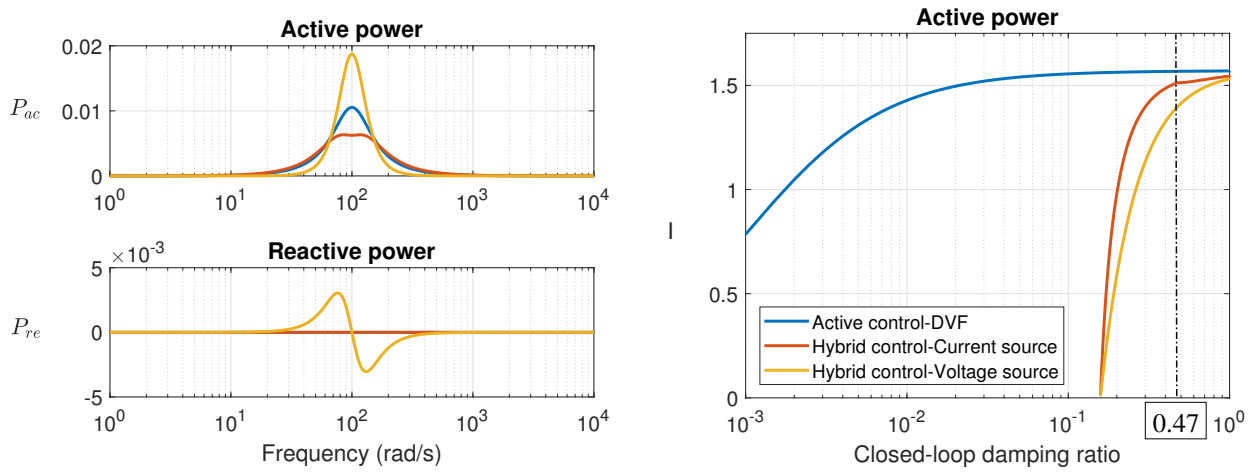

(a) (b)

Figure 4.6: Comparison between the purely active control system (DVF) and the Hybrid control systems, (a) active and reactive power for a specific closed-loop damping ratio (= 47%), (b) the normalized mean square value of the active power I versus the closed-loop damping ratio. (Dash-dotted line shows the 0.47 damping ratio)

where $|f_d(\omega)|^2$ is the power spectral density of the input disturbance force. For the case of white noise excitation force, it is constant as a function of frequency as ($f_d(\omega) = f_d$). Therefore, the mean square value of the power can be simplified as:

$$E[|P_{ac}|] = |f_d|^2 \int_{-\infty}^{\infty} \frac{1}{2} |G_f(j\omega) \times G_{cl}(j\omega) \times G_{cl}^*(j\omega)| \, d\omega \tag{4.17}$$

The normalized mean square value I is defined to represent the ratio of the active power to the excitation force with a uniform spectrum density like:

$$I = \frac{E[|P_{ac}|]}{|f_d|^2} = \int_0^{\infty} |G_f(j\omega) \times G_{cl}(j\omega) \times G_{cl}^*(j\omega)| \, d\omega \tag{4.18}$$

Figure 4.6b compares the performance index I as a function of the closed-loop damping ratio. One sees that the active power is zero for 16% damping ratio and below. This value of the damping is realized by the passive control system according the considered parameters of the system which is defined in Section 3.1.1. While there is no external power required to realize 16% damping ratio by the passive control system, a similar purely active control system requires a large amount of external power. In addition, the active power for the hybrid control systems is always less than the purely active control system. However, for high values of the closed-loop damping, the active power for the hybrid configurations is close to the active power for the purely active control system. The is because most of the work is done by the active portion of the hybrid systems.

4.4 Robustness analysis

The aim of this section is to analyze the robustness of the designed hybrid control systems compared to the purely passive control system. It is particularly focused on the uncertainty of the resonant frequency. To this end, the resonance frequency of the structure changes from ten times lower value to ten times higher value than the resonance frequency of the primary system while the parameters of the controllers are kept constant. The active part of both hybrid control systems is tuned in such a way that the closed-loop system is critically damped, i.e. the closed-loop damping ratio is equal to one, for the primary system ($\omega_0 = 100 rad/s$).

Figure 4.7 shows the closed-loop damping ratio against the resonance frequency of the system. One sees that the performance of the passive control system degrades sharply by changing the resonance frequency of the system. The active voltage source improves the damping of the system around the primary resonance frequency. It can still provide more than 30% damping ratio in the closed-loop system for even 50% changes in the resonance frequency. Furthermore, it can be concluded from Figure 4.7 that the active current source makes the system incredibly robust. If $\omega < \omega_0$, the corresponding hybrid control system can still provide critical damping in the closed-loop system. Moreover, if $\omega > \omega_0$, the control performance degrades slowly. For instance, the controlled system realizes more than 50% damping ratio when the resonance frequency is two times greater than the primary resonance frequency.

4.5 Conclusions

The hybridization of a passive electromagnetic shunt damper with an active control systems has been proposed and analyzed in details. The RC shunt has been used in series with an electromagnetic transducer as the passive control system. Both the active voltage source in series with RC elements and the active current source in parallel with it have been proposed for the hybrid configurations. It has been demonstrated that the system "electromagnetic device + active voltage source" can be seen as an equivalent transducer with an enhanced coupling constant T; equivalence formulae have been presented. In this case, it has been illustrated that the optimal value of the resistance R is modified to a larger value as a function of the feedback gain g_1 in order to improve the damping of the system. In addition, it has been shown that the active current source behaves like a DVF. In this case, the feedback gain g_2 has been optimized based on the method of maximum damping while there is no need to change the parameters of the passive RC circuit. The fact that R does not need to be changed in this configuration is a major advantage compared to the implementation of the active voltage source, as it is much easier to implement a fail-safe system. Moreover, the power consumption has been highlighted to compare the hybrid control systems and purely active control system (using DVF). As a consequence, it has been presented that both hybrid control systems can improve the control performance of the purely passive system while it has less power consumption in comparison with the purely active control system. The designed

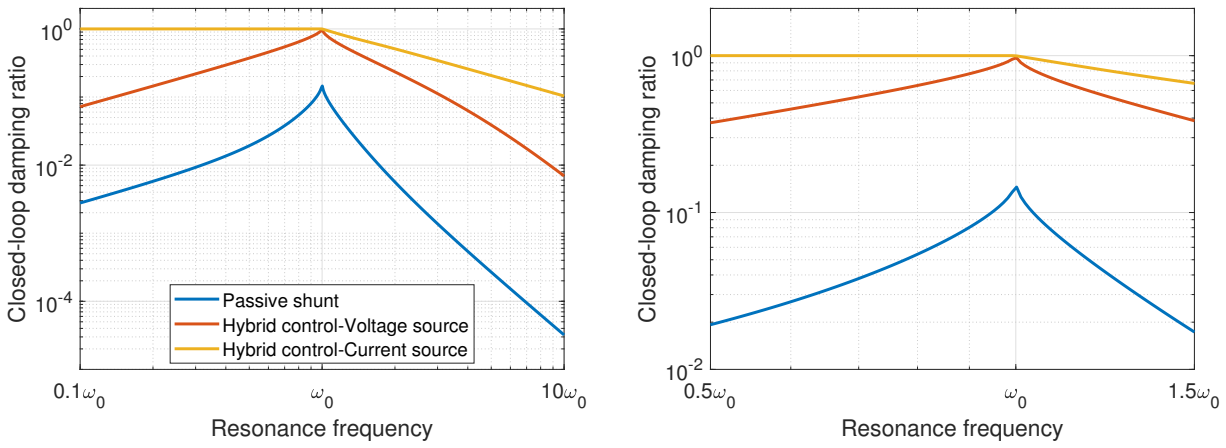

Figure 4.7: (a) Closed-loop damping ratio versus the variation of the resonance frequency when the control parameters are kept constant and tuned to provide the critical damping for the primary system i.e. $\omega = \omega_0$, (b) details near $\omega = \omega_0$

configurations reinforce the robustness of the system because they can sustain a higher level of uncertainty. In particular, the active current source makes the system significantly robust because it can realize critical damping even when the resonance frequency is lower than tuning frequency.

Chapter 5

Vibration Control of Bladed Structures

Contents

The purpose of this chapter is to study the vibration control of bladed structures. In particular, vibration control of the bladed drum which is known as the BluM is of interest. The model of the BluM from different views are shown in Figure 5.1. Due to the complexity of the structure, it is challenging to directly design vibration control systems for the BluM. Therefore, it is proposed to consider the bladed rail which is geometrically simpler than the BluM but exhibits the same dynamic behavior, qualitatively. In doing so, this chapter first review the dynamic behavior of the BluM both numerically and experimentally. Then, the bladed rail is accordingly designed and manufactured.

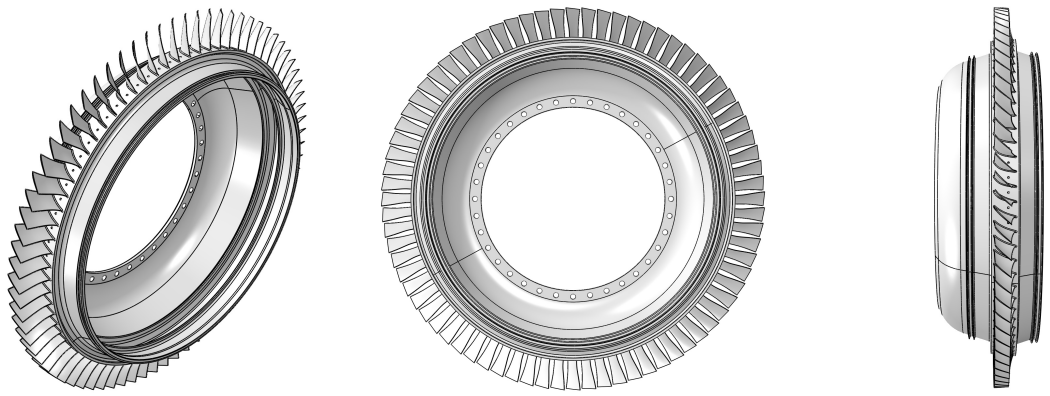

(a) (b) (c)

Figure 5.1: The model of the BluM from a) the general view, b) the front view, and c) the side view.

5.1 The BluM

5.1.1 Dynamics of the BluM

Numerical simulations and experimental tests are conducted in the following section to give a better insight about the vibration characteristics of the BluM. The first set of experiment has been carried out on the real application which is shown in Figure 5.2a. According to Figure 5.2c, the BluM is excited by a hammer while the velocity of the tip of a blade is measured by a laser vibrometer. The FRF of the system from the hammer to the laser is shown in Figure 5.2b. The frequency of the figure is normalized with respect to the first resonance frequency of the first family. Three main characteristics of the BluM can be seen from the figure. They include i) the low internal damping because of high amplification of response around the resonance frequencies, ii) the high modal density resonances corresponding to the first mode family, and iii) the single resonances, which are separated from others, corresponding to the resonances of the drum part.

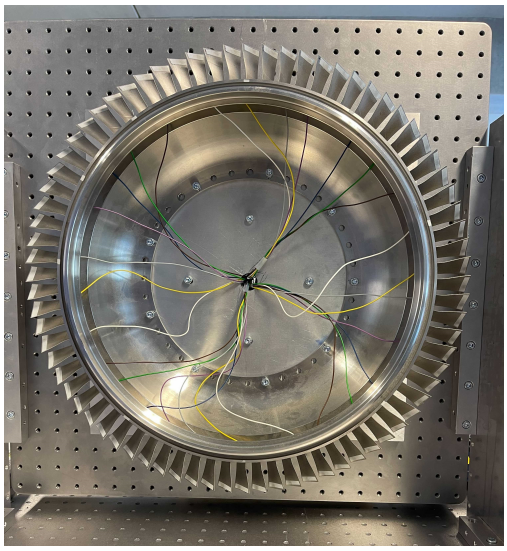

(a)

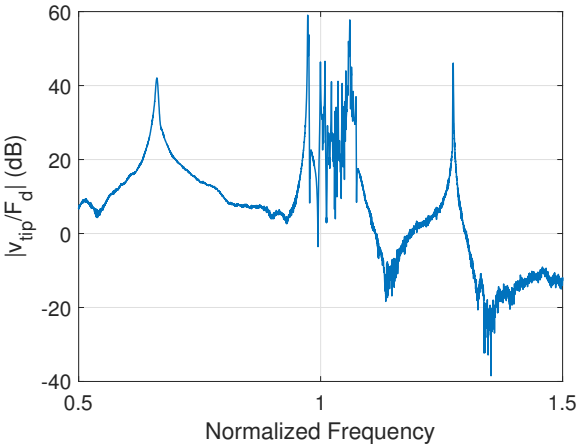

(b)

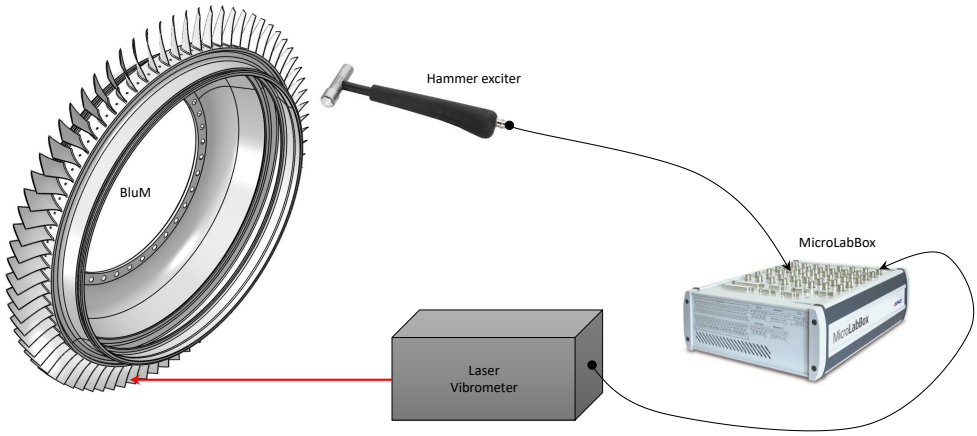

(c)

Figure 5.2: a) Experimental setup of the BluM. b) FRF of the system from the hammer to the laser vibrometer. c) Schematic of the experimental test.

In order to show the mode shapes of the BluM, a numerical study based on finite element method (FEM) in Abaqus has been performed, using quadratic tetrahedral solid elements. According to Figure 5.2b, there are three resonances before the resonances of the first family. These resonances have been also observed in the numerical analysis. The mode shapes of these three resonances are shown in Figure 5.3. It can be seen that the mode shapes appear with two, three, and four nodal diameter. The mode shapes with two and three nodal diameter are called drum dominate modes that the maximum deformation appear on the drum. In this case, the blades have only translational motion caused by the deformation of the drum part. Furthermore, the mode shape with four nodal diameter corresponds to the couple mode that the maximum motion is distributed on both the drum and blades.

Figure 5.4 shows mode shapes of three resonances of the first family. The mode shapes correspond to zero, one, and five nodal diameter. Note that these three mode shapes have been chosen arbitrary among all resonances of the first family to show the typical behavior of mode shapes of the first family. These modes are called the blade dominate modes where the maximum deformations occur on the blades. In particular, the maximum deformation occurs at the tip of the blades that are placed far from the nodal line(s). It can also be seen that the motion of the blades with respect to the drum represents the first bending mode of the blades. It should be noted that in

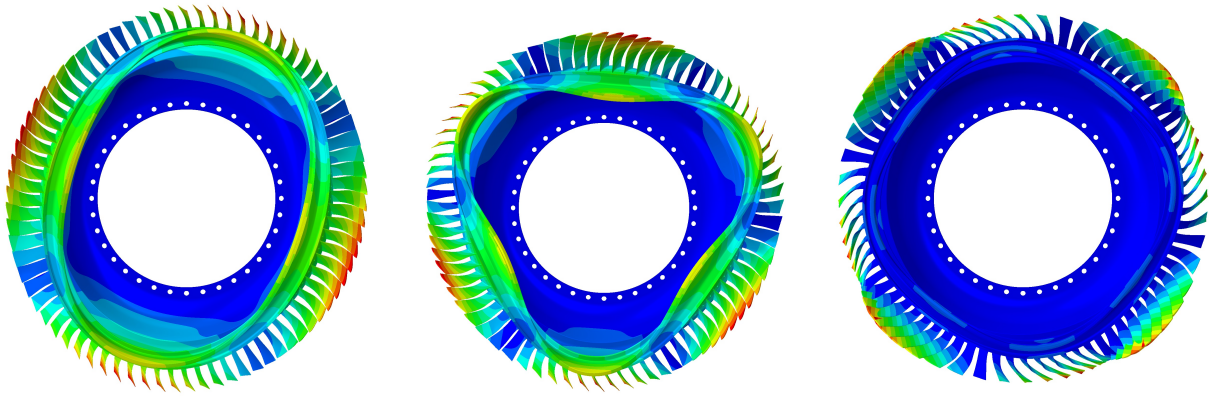

(a) (b) (c)

Figure 5.3: Low frequency mode shapes of the BluM with a) two, b) three, and c) four nodal diameter.

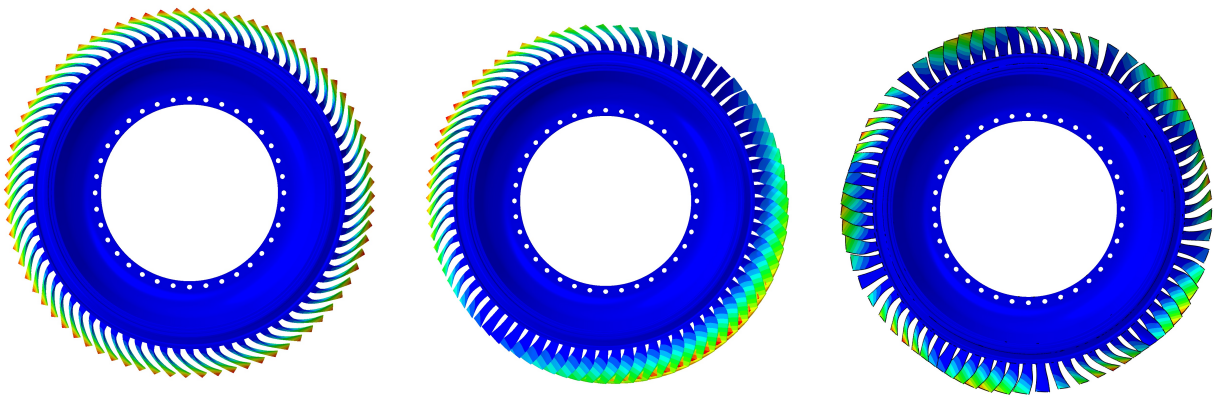

(a) (b) (c)

Figure 5.4: Mode shapes of the first family with a) zero, b) one, and c) five nodal diameter.

the next mode families, another mode shapes of the blades such as torsion modes or high order bending modes will be excited. For all resonances in each family, the blades experience the same behavior although they can still move in-phase or out-of-phase with respect to the ones in their neighborhood. If all the blades are in-phase, there will be no nodal line and if all of them are out-of-phase, there will be 38 nodal lines as 76 blades symmetrically placed on the BluM.

Due to the cyclic symmetry of the structure, the mode shapes appear in pair. This is valid for all types of mode shapes including drum dominate modes, coupled modes, and blade dominate modes except those with zero and 38 nodal diameters. Assuming the drum is perfectly symmetrical and the blades are ideally identical, both modes of a pair are associated to the same resonance frequency. Since imperfections are inevitable in the manufacturing process, the resonances of a pair could be slightly different. This difference can be negligible. It should be noted that the resonances of a pair come in orthogonal mode shapes which exhibits the same shape with 90° phase shift. This means that the blades, which are close to the nodal line in one mode, will have maximum deformation in the orthogonal mode.

5.1.2 Optimal location of piezoelectric patches

In order to increase the damping of the structure, piezoelectric patches are proposed to be used because of several reasons including i) they behave almost linearly, ii) they can be found in any size and shape, iii) they can be used for both active and passive control strategies, iv) they can be used as sensor and/or actuator for the application of the active control system, etc. In addition, the piezoelectric patches can have a relatively good electromechanical coupling factor which is defined as the ability of the transducer to convert mechanical energy into electrical energy and vice versa. As discussed in [25], this factor has a direct effect on the performance of the control system because it can determine the observe-ability of the piezoelectric sensor and the control-ability of the piezoelectric actuator. Moreover, this factor is proportional to the strain energy in the piezoelectric patch. Consequently, the optimal locations of piezoelectric patches are defined to be the areas of the structure where the strain energy is larger for a target mode(s). Figure 5.5 presents the strain energy map of the BluM for three resonances of the first family with zero, one, and five nodal diameter. In all cases, the maximum strain energy appears close to the root of the blades. Figure 5.6a illustrates the typical strain map of a blade which is placed far from the nodal line. Note that the strain map of the blades look the same for all the resonances as long as the first bending mode of the blades corresponding to the first family is considered. Although locating the patches

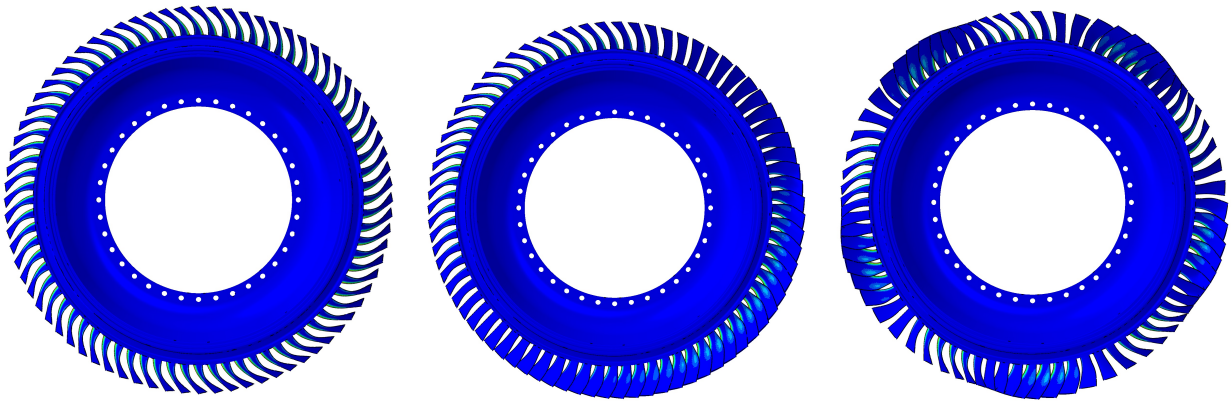

(a) (b) (c)

Figure 5.5: Strain energy distribution of the BluM for three resonances of the first family with a) zero, b) one, and c) five nodal diameter.

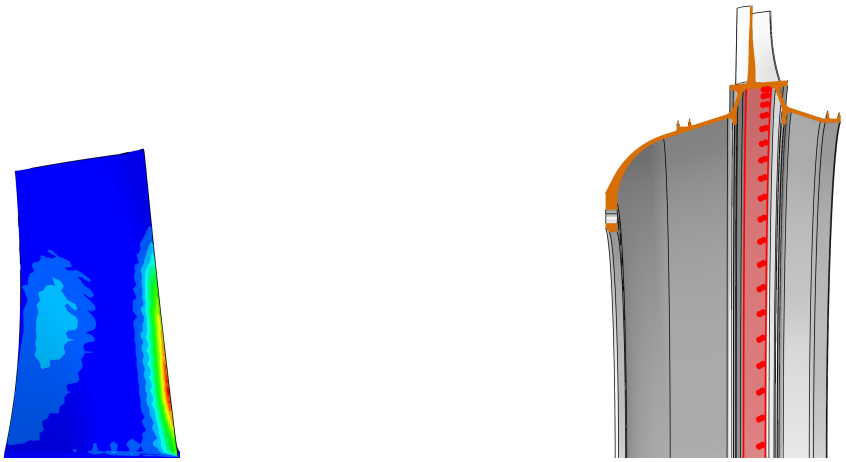

(a) (b)

Figure 5.6: a) Typical strain energy distributed on a blade which is excited by a resonance of the first family. b) A cutted view of the BluM to show the possible location for mounting piezoelectric patches.

at the blade root clearly maximizes the strain energy, it results in important perturbations of the aerodynamic flow.

Figure 5.6b shows a cutted view of the internal part of the BluM. The only possible location of piezoelectric patches on the BluM is highlighted with a red color. This is basically the location of the BluM where the blades are located on the other side. For this location, Figure 5.7 plots the strain energy distribution for three resonances of the first family with zero, one, and five nodal diameters. Interestingly, local strain distributions, caused by the motion of the blades, appear in this region. Clearly, piezoelectric patches are proposed to be placed on these local deformation in order to maximize the control-ability and observe-ability. Owing to the application of active control systems where sensors and actuators are required, the patches come in pair such that two rectangular piezoelectric patches are mounted on each local deformation. In this case, one patch of a pair can be used as sensor and other one as an actuator. This is the only configuration of piezoelectric patches which makes the system observe-able and control-able for all the resonances of the family. Note that the size of the piezoelectric patches are chosen such that a pair of patches fully covers the local deformation. If the size of patches are larger than that, two major problems arise as follow:

- The observe-ability and the control-ability reduce significantly for some modes because of charge cancellations. The charge cancellation may occur in a patch which covers some local deformations while the signs of those local strain distributions are not the same. The strain sign depends on the direction of the motion of the corresponding blade. Thus, two local deformations have the same strain sign if their blades are moving in-phase. While, they have an opposite strain sign if their blades are moving out-of-phase. Clearly, a higher number of nodal diameters brings a higher fluctuation of the strain signs. Therefore, the charge cancellation in a patch can easily happen for these resonances. On the other hand, it has been shown in [7] that a large size piezoelectric patch can be still used when only one mode of the BluM is targeted.

- An active control system becomes impossible to be implemented since the FRF of the open-loop transfer function from a piezoelectric actuator to a piezoelectric sensor is no longer collocated in terms of pole-zero pattern. Non-collocated open-loop transfer function makes the system unstable by closing any feedback loop. More information regarding this concept

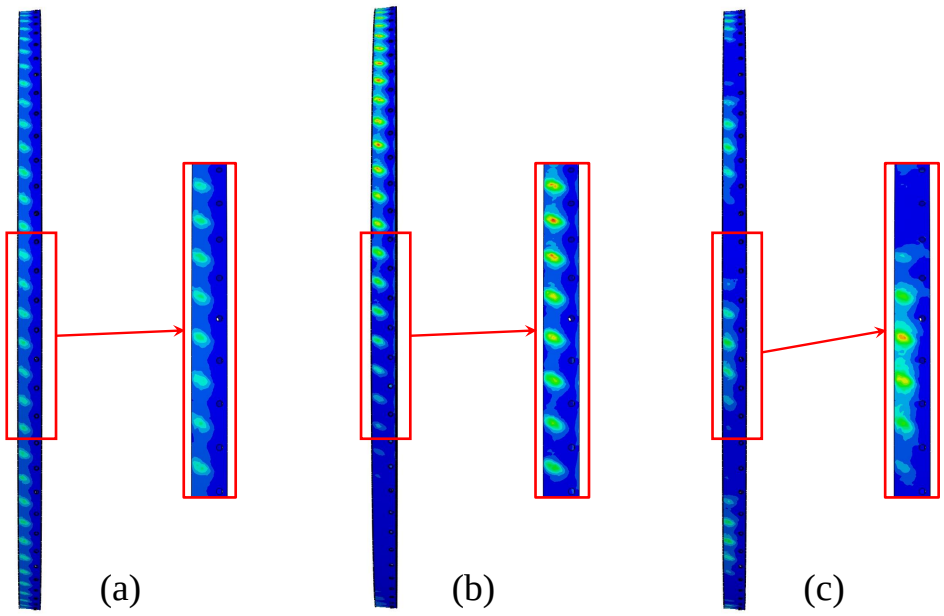

Figure 5.7: Strain energy map of the internal part of the BluM from side view for three resonances with a) zero, b) one, and c) five nodal diameters.

is given in [25]. Locating the piezoelectric sensor and the piezoelectric actuator on the area of the structure where the strain sign does not change guarantees a collocated open-loop transfer function.

Figure 5.8 shows the schematic of the BluM including piezoelectric patches in the order which have been explained above. In this configuration, there are 76 independent pairs of patches.

The type of piezoelectric patches still remains to be defined. Among all three main possible operating modes of piezoelectric patches including the bending mode, the shear mode, and the longitudinal mode, it is proposed to use piezoelectric patches in bending mode. This is simply because the other kinds are mainly effective when a relative motion occurs between the two ends of a patch. In the market, many companies producing piezoelectric patches with specific electromechanical properties. In the following section, different types of piezoelectric patches are experimentally compared on the BluM.

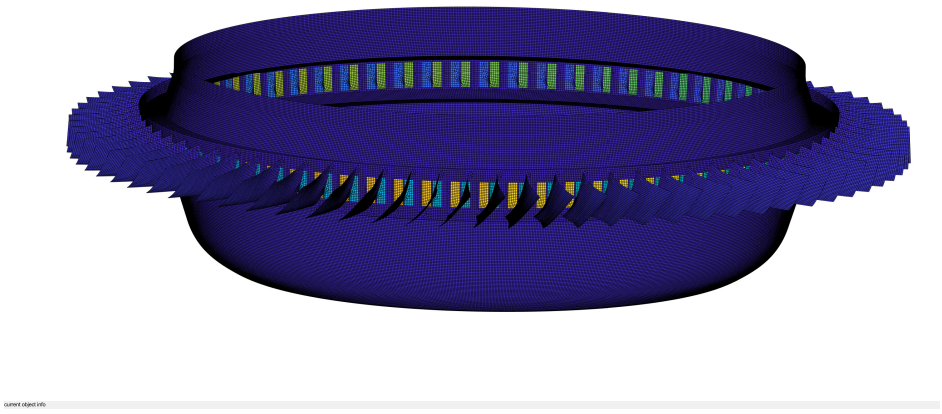

Figure 5.8: Schematic of the BluM with the piezoelectric patches.

Figure 5.9a shows the experimental setup with four different types of piezoelectric patches. They include 1) Piezoelectric Ceramic based on Lead Zirconate Titanate (PIC-151) with 0.2mm thickness from PI company[1], 2) PIC-151 with 0.5mm thickness from PI company[2], 3) Macro Fiber Composite (MFC p2 type) from Smart-Material company[3], and 4) Dura-Act transducers from PI company[4]. It should be noted that the size of the patches has been modified accordingly such that they fit there.

In order to conduct the experiment, a *dSPACE MicroLabBox* is used for the data acquisition. The system is designed first inside the graphical *SIMULINK* environment of *MATLAB* and then compiled. The compiled file is downloaded onto the *ControlDesk* environment of *dSPACE* software, which is connected directly to the *MicroLabBox* hardware, to be executed in real time. The system is discretized at a sampling frequency of 40 kHz. A chirp signal has been considered to excite the actuator in a period of 50 seconds from a frequency 0.9346 times lower than the first resonance of the first family to a frequency 1.1215 times higher than the first resonance of the first family. The chirp signal automatically repeats four times in order to be able to average the response in the post-processing. Figure 5.9b shows the magnitude, the phase, and the coherence of the open-loop response for four pairs of patches. Most importantly, it can be seen that the open-loop response are collocated in terms of pole-zero pattern for all cases. However, the FRF starts with a zero for

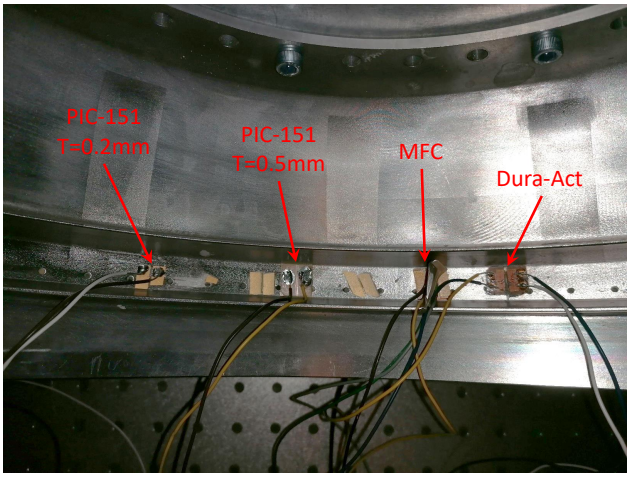

(a)

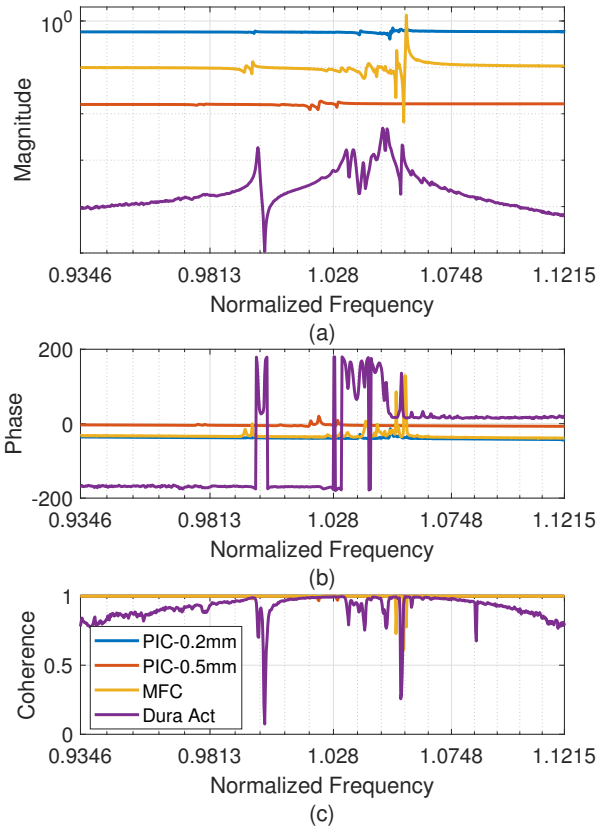

(b)

Figure 5.9: a) Experimental setup of the BluM with four different pairs of piezoelectric patches. b) Experimental open-loop response for four different pairs of piezoelectric patches showing a) the magnitude, b) the phase, and c) the coherence.

[1]https://www.piceramic.com/en/products/piezoelectric-materials/
[2]https://www.piceramic.com/en/products/piezoelectric-materials/
[3]https://www.smart-material.com/MFC-product-main.html
[4]https://www.piceramic.com/en/products/piezoceramic-actuators/patch-transducers/p-876-duraact-patch-transducer-101790/

the PIC(s) and MFC while it starts with a pole for the Dura-Act. It is interesting to note that they do not present the same observe-ability and control-ability on different resonances. The observe-ability is determined by the number of resonances appear in the FRF. Also, the control-ability can be estimated be the distance between the frequencies of the pole and the corresponding zero. Thus, MFC and Dura-Act qualitatively show a better observe-ability and control-ability in comparison to the PIC(s). The difference between the MFC and the Dura-Act comes at the static gain. This is lower for the Dura-Act. This means that a higher value of the feedback gain would be required in the closed-loop for the Dura-Act.

5.2 The bladed rail

5.3 Numerical modeling of the bladed rail

Figure 5.10 shows the manufactured bladed rail which was made of aluminium. The monobloc bladed rail comprises five identical blades placed on a support. Its geometry is adapted to that of the conventional compressor bladed drum (BluM) 5.2a. As a boundary condition, the bottom part of the structure is clamped to a rigid wall. Due to the complexity of the structure, its finite-element-model (FEM), shown in Figure 5.11a, was built using shell elements. The normalized frequencies of the first seventeen modes of the structure are shown in Figure 5.11b. Note that the frequencies are normalized with respect to the frequency of the first resonance. Clearly, modes can be categorized into two types. The first type corresponds to the mode family consisting of five resonances with very close frequencies. Figure 5.12 shows the first mode shapes of the first three families. One sees that the motion of the blades are dominant such that the mode shapes of the first, second and third families are representing the first bending, the first torsion and the second bending of the blades, respectively. Note that the separation of the resonance frequencies in a family depends on the rigidity of the support. In addition, the second type of modes represent the resonances of the support which are isolated from others. In this study, the vibration of the first family of modes is of interest.

When a piezoelectric patch is used as a sensor, the output voltage is proportional to the relative rotation of its extremities. Similarly, the moment applied by a piezoelectric patch is proportional to the relative rotation of its extremities. To maximize the observability and controlability, the optimal location of these transducers is the area of the structure where the strain energy is max-

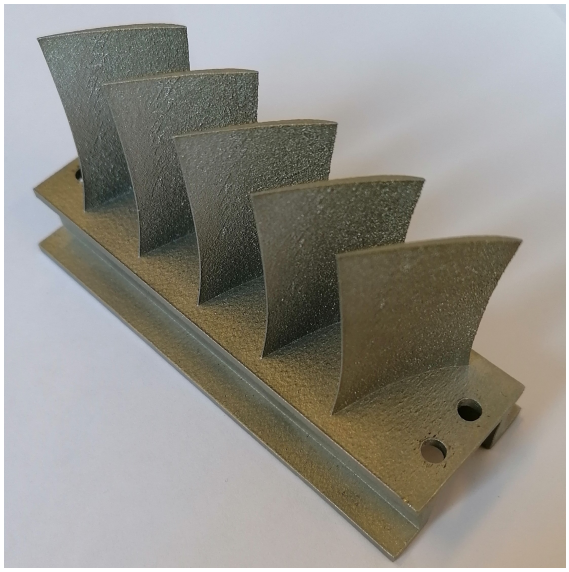

Figure 5.10: The bladed rail

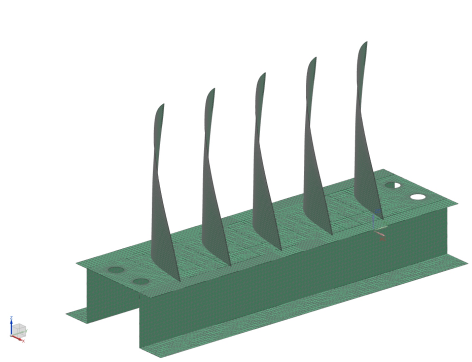

(a)

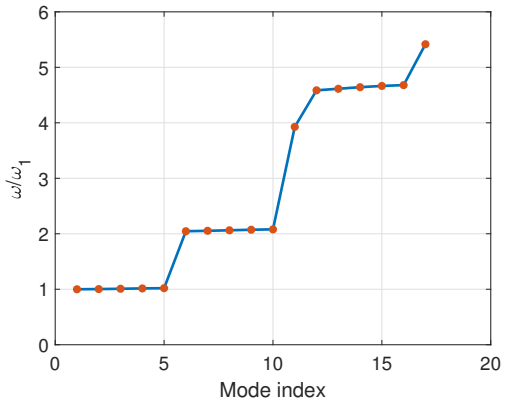

(b)

Figure 5.11: (a) Model of the bladed rail structure. (b) Normalized resonance frequencies of the bladed assemblies (ω_1 is the first bending mode frequency of the first family)

imized. The strain energy map of the first five modes corresponding to the first family of modes is shown in Figure 5.13. One sees that the strain energy is maximized at the root of each blades.

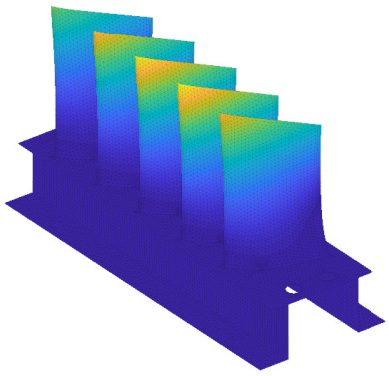

(a) Mode1

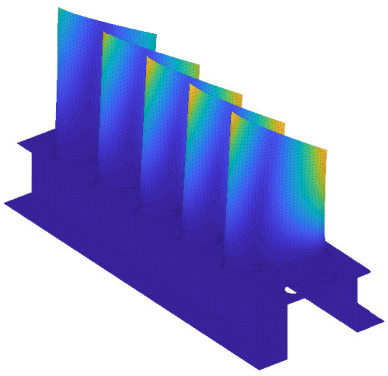

(b) Mode6

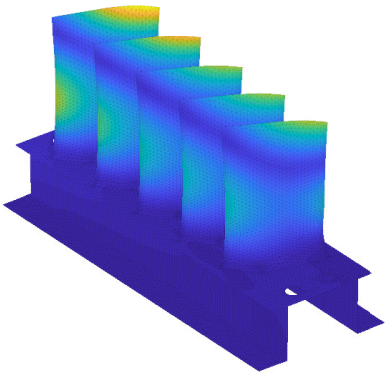

(c) Mode12

Figure 5.12: First mode shape of the (a) first, (b) second, and (c) third families

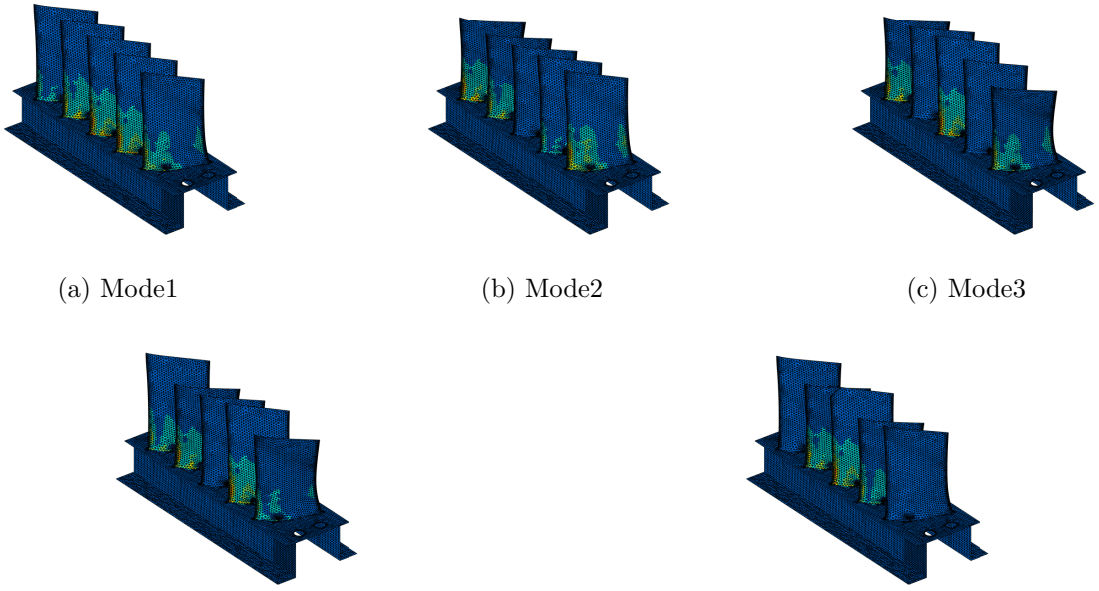

(a) Mode1 (b) Mode2 (c) Mode3

(d) Mode4 (e) Mode5

Figure 5.13: Strain energy distribution of the first five modes corresponding to the first family

However, the patches cannot be placed there because they can easily disturb the aerodynamic flow. To overcome the aforementioned limitation, it is required to place the transducers on the internal part of the support. For this area, the strain map is shown in Figure 5.14. It is clearly visible that a local strain distribution is generated below each blade. The local deformations are separated by an artificial nodal line where no strain is generated. Depending on the motion of a blade, the deformation is either in tension or in compression; and subsequently, the charge generated in a piezoelectric patch is either positive or negative. In order to avoid charge cancellation in the

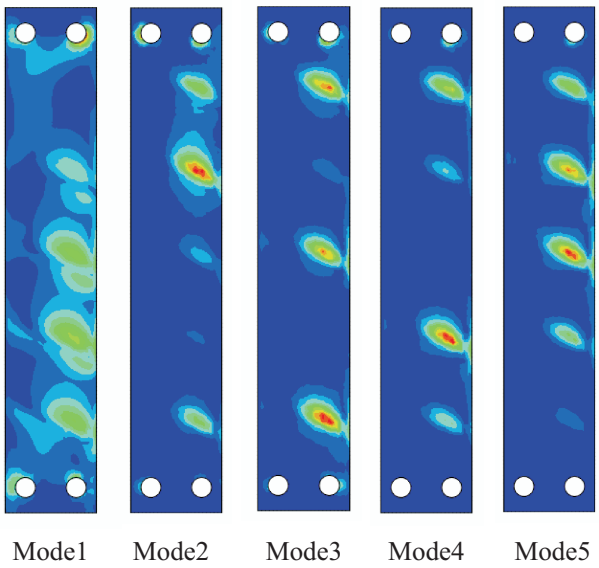

Figure 5.14

Figure 5.15: (a) Strain distribution of the internal part of the support for the first family of modes. (b) Configuration of the piezoelectric patches on the structure

patches, the size of piezoelectric patches can not be greater than the local deformation area.

For the application of the piezoelectric shunt damping, one patch can be simply mounted on each local strain map as shown in Figure 5.16a. While, for the active control strategies, the locations of piezoelectric sensor and piezoelectric actuator are important with respect to each other since it directly affect the open-loop transfer function and subsequently the design of the active control system. Assuming that the relative rotation of the extremities of both sensor and actuator is almost the same when they are placed next to each other, the frequency response function (FRF) from voltage applied by the actuator to the voltage measured by the sensor contains alternating pole-zero, i.e. collocated system, which is of interest in active control techniques since its phase is always between -180° and 180°. Consequently, two collocated piezoelectric patches (using one of them as sensor and the other one as an actuator) are placed on the support below each blade such that they cover local strain distribution as it can be seen in Figure 5.16b.

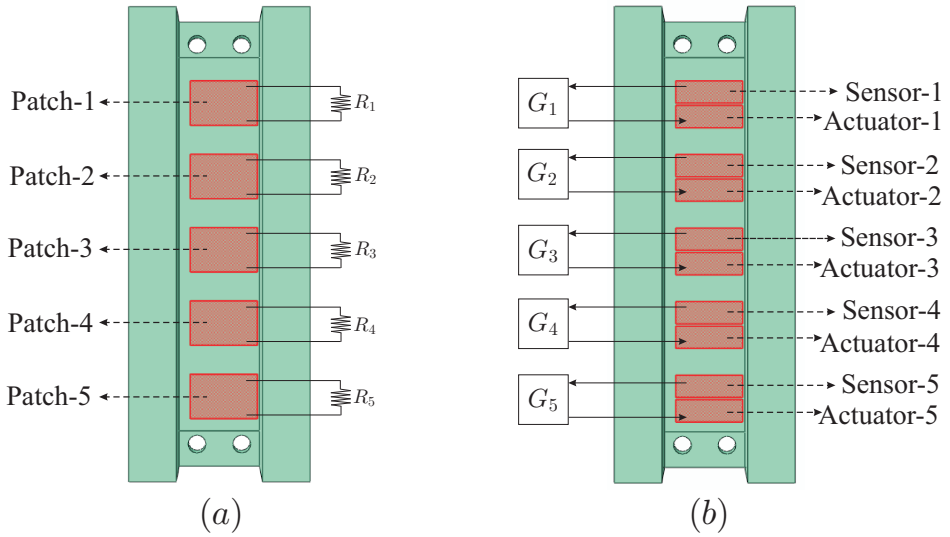

Figure 5.16: Configuration of the piezoelectric patches for the implementation of (a) the passive resistive shunt and (b) the active control system

5.3.1 Vibration control of the bladed rail

Broadband control system

The aim of this section is to design and compare a passive and an active control device which are less sensitive to resonance uncertainties. Although resonant controllers like piezoelectric RL shunt damping outperform broadband vibration absorbers in terms of vibration attenuation, tuning their parameters is highly dependent on the precise estimation of the primary system resonances. Therefore, resistive shunt damping is proposed in the present study for the passive control system due to the robustness to fluctuations of resonances. The piezoelectric patches shown in Fig. 5.16a are then modeled as charge actuators and voltage sensors. Fig. 5.17a illustrates the frequency-response-function (FRF) from the charge actuator of each piezoelectric patch to the voltage sensor of the same patch. Note that the frequency is normalized with respect to the frequency of third mode. Basically, the frequency of zeroes corresponds to the resonances of the structure when the electrodes are short-circuited and the frequency of poles is related to the resonance of the structure when the electrodes are open-circuited. It has been shown by Preumont [**?**] that assuming the modes are well separated in frequency, the separation between the frequency of the pole and the zero determines the maximum attainable damping ratio in the closed loop response for the i-th

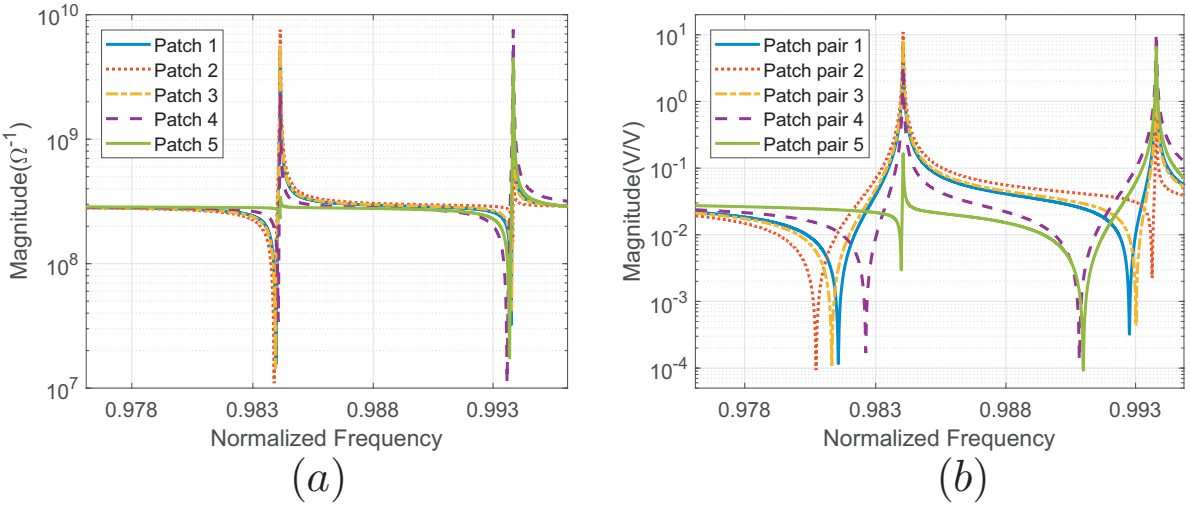

Figure 5.17: (a) The magnitude of the transfer function from charge to the voltage of each piezoelectric patches. (b) The magnitude of the transfer function from voltage actuator to the voltage sensor of each pair of patches. (The frequency is normalized with respect to the frequency of third resonance.)

mode. The maximum modal damping (ξ_i^{max}) is then given by:

$$\xi_i^{max} = \frac{\omega_i^p - \omega_i^z}{2\omega_i^z} \tag{5.1}$$

where ω_i^z and ω_i^p are the frequencies of zero and pole of the i-th mode, respectively. Fig. **??**a depicts the maximum achievable closed-loop damping of each mode by using different piezoelectric patches. In order to optimize the damping of each mode, one patch is used to maximize the damping of one mode. Therefore, first, fourth, fifth, second and third patch are used to maximize the damping of mode 1, mode 2, mode 3, mode 4 and mode 5, respectively.

On the other hand, low electromechanical coupling between the transducers and the structure significantly diminishes the control authority of the passive technique. Therefore, let us use a sim-

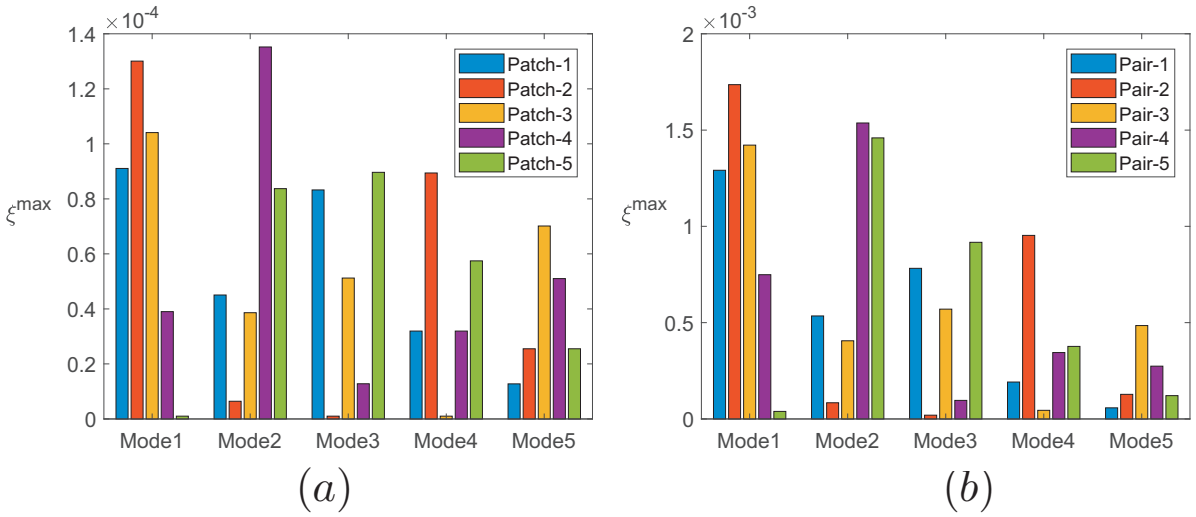

Figure 5.18: The maximum attainable closed-loop damping of each mode by the implementation of (a) the passive resistive shunt, or (b) the active control system

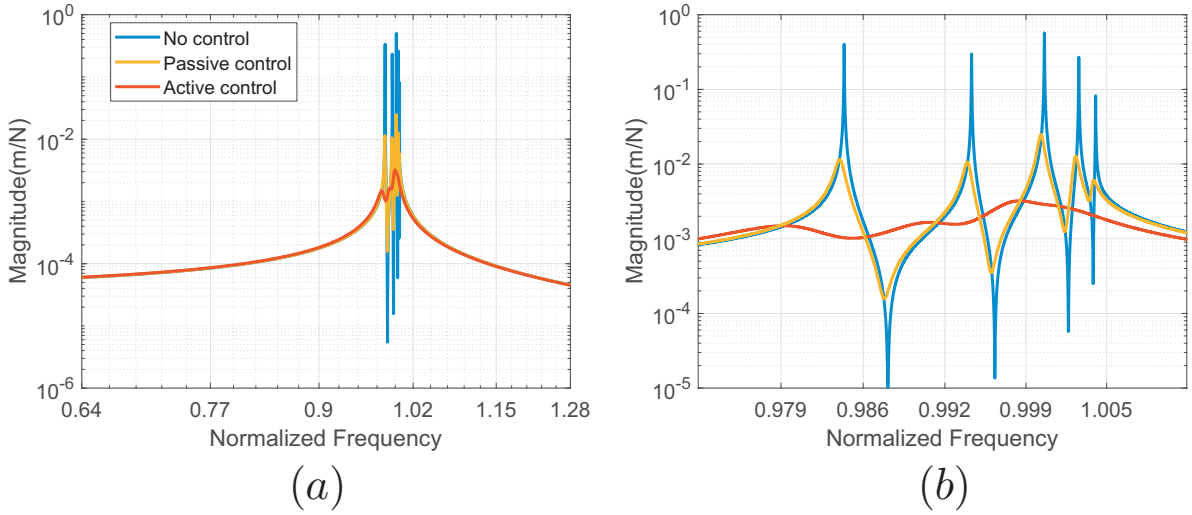

Figure 5.19: (a) FRFs of the system with no control (blue curve), the active control (red curve) and the passive absorber (yellow curve), (b) zoom close to the resonances. (The frequency is normalized with respect to the frequency of third resonance.)

ple broadband active control law, i.e. an integrator, to damp the resonances of the first family based on the configuration shown in Fig. 5.16b. Fig. **??**b shows the magnitude of the transfer function from each actuator to the collocated sensor for the first two modes. One sees that the system contains alternating zero-pole configuration with no high frequency roll-off. For each mode, the frequency of the pole is the same for all pairs because it corresponds to a resonance frequency of the structure, while the frequency of the zero changes. According to Fig. **??**b which demonstrates the maximum achievable closed-loop damping using different pair of patches, the order of the closed loop damping ratio is ten times higher than that of resistive shunt.

As it was already explained in the previous section, the maximum displacement of the first family of modes occurs at the tip of the blades. Then, a representative compliance curve is defined as a performance index from an excitation force to a displacement sensor which are located at the tip of one blade. Fig. 5.19 presents the FRFs of the performance index obtained with and without control devices. This figure shows that the active control system provides an attenuation of the response amplitude which is 18dB greater than for the passive resistive shunt

Resonant control system

The open-loop transfer function from each piezoelectric actuator to its collocated piezoelectric sensor is shown in Figure 5.16b. One sees that the system contains alternating zero-pole configuration with no high frequency roll-off. For each mode, the frequency of the pole is the same for all pairs because it corresponds to a resonance frequency of the blades, while the frequency of the zero changes. In an active control system, the controllability of a target resonance can be assessed by the distance between the frequency of the pole and the frequency of the zero. For example, the third pair is not efficient enough to damp the second resonance due to the close location of second zero with respect to the second pole. It is also similar for the fourth resonance too. However, this pair can highly add damping to the first, third and fifth resonances.

The control configuration is shown in Figure 5.20, which is a multi-input-multi-output (MIMO) system with decentralized control system using the same control law. The choice of the control law is dependent on the location of zeroes with respect to poles. When the zeroes appear before poles, the open-loop transfer function is similar to that of a system when a force actuator is collocated

to a force sensor. For such a system, two active control laws, including a simple integrator, known as integral-feedback (IF), or a double integrator combined with a real zero, known as α-controller, were proposed. Therefore, these two control laws are implemented in the present system as shown below:

$$H(s) = \frac{g_i}{s} \tag{5.2}$$

$$H(s) = \frac{g_{ii}(s+\alpha)}{s^2} \tag{5.3}$$

In order to tune the control parameters, a numerical optimization in MATLAB is employed using *fminsearch* function. The optimization consists in maximizing the minimum damping of the system. Figure 5.21a shows the minimum damping ratio of the first family of modes against the number of the closed-loops. As it can be seen when all the loops are closed, the minimum damping of the system is about 2.5% and 8% when the IF or α-controller is used, respectively. To check how effective the control system is, the performance index of the system is defined as the transfer function from the force injected at a tip of the fifth blade to the displacement at the same location. The FRF of the performance index with and without control systems is shown in Figure ??. It can be clearly seen that the maximum amplitude of response when α-controller is used is three times

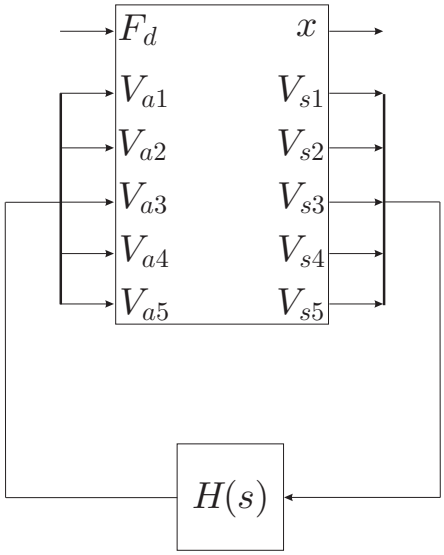

Figure 5.20: Block diagram of the numerical controller architecture.

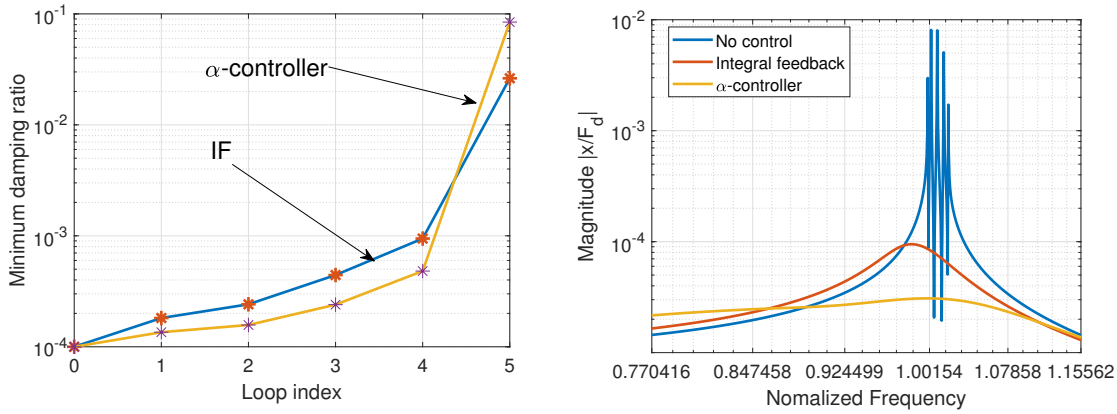

(a)

Figure 5.21: (a) Minimum damping ratio of the system against the number of closed loops. (b) Numerical FRF of the performance index with and without control system.

lower than that of IF controller. Better control performance obtained by α-controller comes at the expense of a decrease in the phase margin. This can be seen in Figure **??** where the phase margin is plotted against the number of the closed-loop system. Note that the system is assumed to be multi-single-input-single-output (multi-SISO).

5.3.2 Experimental result

To perform the experimental tests, a dSPACE MicroLabBox was used for the purpose of both the data acquisition and the control system. The control configuration is designed first inside the graphical SIMULINK environment of MATLAB and then compiled. The compiled file is uploaded into the ControlDesk software connected directly to the MicroLabBox hardware. The system is running in real time at a sampling frequency of 20 kHz. The measured data were recorded at the same sampling frequency.

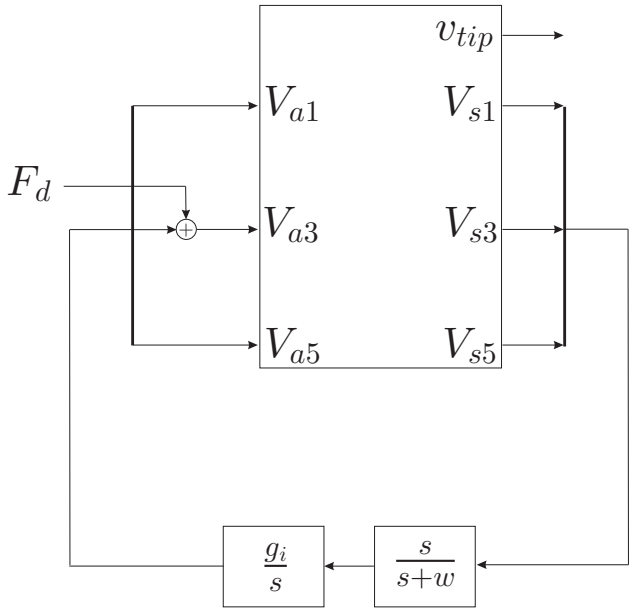

Figure 5.22: Block diagram of the experimental controller architecture.

In this study, the experiments were performed using only the fourth pair of patches. The configuration scheme for the experimental study is shown in Figure 5.22. F_d and V_a are the disturbance force and the actuation control voltage, respectively. Note that the same piezoelectric actuator was used for the excitation. A chirp signal generator excited the structure around the first family of resonances. v_{tip} and V_s are the tip velocity of the fifth blade and the voltage measured by the fourth piezoelectric patch, respectively. The velocity of the tip blade v_{tip} was measured by the polytec laser vibrometer. Therefore, the performance index is defined as the transfer function from the disturbance force F_d to the velocity of the tip blade v_{tip}.

The FRF of the experimental open-loop transfer functions for the first, the third, and the fifth pairs are shown in Figure 5.23a. The obtained modal damping of the these resonances is 0.5%, 0.062%, 0.055%, 0.05% and 0.045% for the first, second, third, fourth and fifth modes, respectively. One sees that each pair shows different the observe-ability and the control-ability for each mode. For example, the firth and the third pairs have no observe-ability and control-ability on the fifth mode; while, the fifth pair shows high observe-ability and control-ability. This also implies that almost no strain is generated at the location of the first and the third piezoelectric pairs when the fifth resonance is excited.

In this study, we only focus on the implementation of an integral feedback. In order to avoid

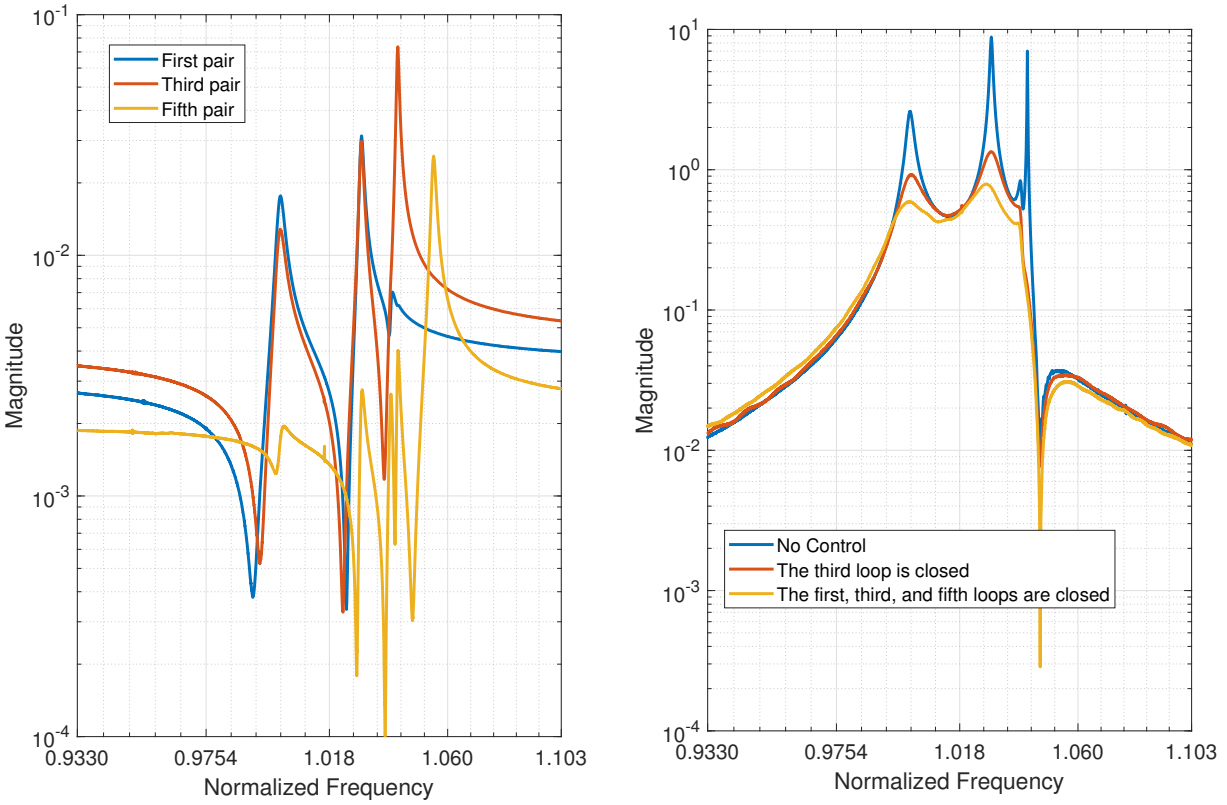

(a)

Figure 5.23: (a) Experimental FRF of the open-loop transfer function from the fourth piezoelectric patch to the fourth piezoelectric sensor. (b) Experimental FRF of the performance index with and without control system.

integrating the low-frequency contents of the sensor, a high-pass filter is also added in the feedback loop. The optimal value of the feedback gain is tuned following the procedure explained in the previous section. The FRF of the experimental performance index from the disturbance force to the velocity of the tip fifth blade is presented in Figure ??. All resonances of the first family are visible. It can be seen that, the controller can damp the second, third and fifth resonance while it has no control over the first and fourth resonances as it was expected.

5.4 Conclusions

Chapter 6

Conclusions and Perspective

The conclusions come here.

Appendix A

The Parseval's theorem

The mean square value of the electrical power in time domain $P_e(t)$ read as:

$$\int_{t=-\infty}^{\infty} P_e(t)\,dt = \int_{t=-\infty}^{\infty} V(t) \times I^*(t)\,dt \tag{A.1}$$

where $V(t)$ and $I^*(t)$ are the voltage and the conjugate of current of a signal. Considering the inverse Fourier transform, the above equation can be re-written as:

$$\int_{t=-\infty}^{\infty} V(t) \times (\frac{1}{2\pi} \int_{\omega=-\infty}^{\infty} I^*(\omega) e^{-j\omega t}\,d\omega)\,dt \tag{A.2}$$

where $I(\omega)$ is the current in frequency domain. After some manipulation, the above integral can be modified as:

$$\frac{1}{2\pi} \int_{\omega=-\infty}^{\infty} I^*(\omega) \times (\int_{t=-\infty}^{\infty} V(t) e^{-j\omega t}\,dt)\,d\omega \tag{A.3}$$

The value of parenthesis is equal to the Fourier transform of the voltage. Then, the integral can be modified as:

$$\frac{1}{2\pi} \int_{\omega=-\infty}^{\infty} V(\omega) \times I^*(\omega)\,d\omega = \frac{1}{2\pi} \int_{\omega=-\infty}^{\infty} P_e(\omega)\,d\omega \tag{A.4}$$

which is equal to the mean square value of the electrical power in frequency domain $P_e(\omega)$. It should be mentioned that similar to the electrical power, this theorem is also valid for the mechanical power as well:

$$\int_{t=-\infty}^{\infty} P_m(t)\,dt = \frac{1}{2\pi} \int_{\omega=-\infty}^{\infty} P_m(\omega)\,d\omega \tag{A.5}$$

By considering the Maxwell analogy which states that the force F and the velocity v in mechanical domain are variables analogous to the voltage V and the current I in electrical domain, we have:

$$\int_{t=-\infty}^{\infty} F(t) \times v^*(t)\,dt = \frac{1}{2\pi} \int_{\omega=-\infty}^{\infty} F(\omega) \times v^*(\omega)\,d\omega \tag{A.6}$$

A.1 A practical example

In the following section, we will use the example of the electromagnetic transducer shunted with RC elements, which has been discussed in Chapter 2, to calculate the power of the actuator in the time and the frequency domains. The parameters of the primary system follows the numerical values explained in Chapter 2 and the parameters of the shunt are tuned according to the Eqs. (2.10). In order to calculate the power, the following steps need to take:

1. The state space model of the system is extracted. The model contains two inputs and one output. The inputs are the external disturbance force f_d and the actuator force f_a, and the output is the displacement of the mass x.

2. The model is imported into the Simulink environment.
3. A random noise excitation based on Gaussian distribution is used to excite the system.
4. The passive control system is implemented in the feedback loop.
5. The simulation is running in 10kHz sampling frequency.
6. The simulation is recorded for 100 seconds.
7. The data of the velocity and the actuator force is saved for the calculation of the mechanical power.

The script below is used to extract the state space model:

```
clearall
clc
s = tf('s');
m = 1; %Mass
k = 1e4; %Stiffness
T = 1; %Coupling constant
L = 1e-3; %Inductance of the coil
G1 = 1/(m*s^2 + k); %Transfer function from disturbance force to the displacement
[b1, a1] = tfdata(G1);
G11 = nd2sys(b1{1,1}, a1{1,1});
G2 = 1/(m*s^2 + k); %Transfer function from actuator force to the displacement
[b2, a2] = tfdata(G2);
G22 = nd2sys(b2{1,1}, a2{1,1});
G = sbs((G11), (G22));
[A, B, C, D] = unpck(G);
sys = ss(A, B, C, D); %State space model
```

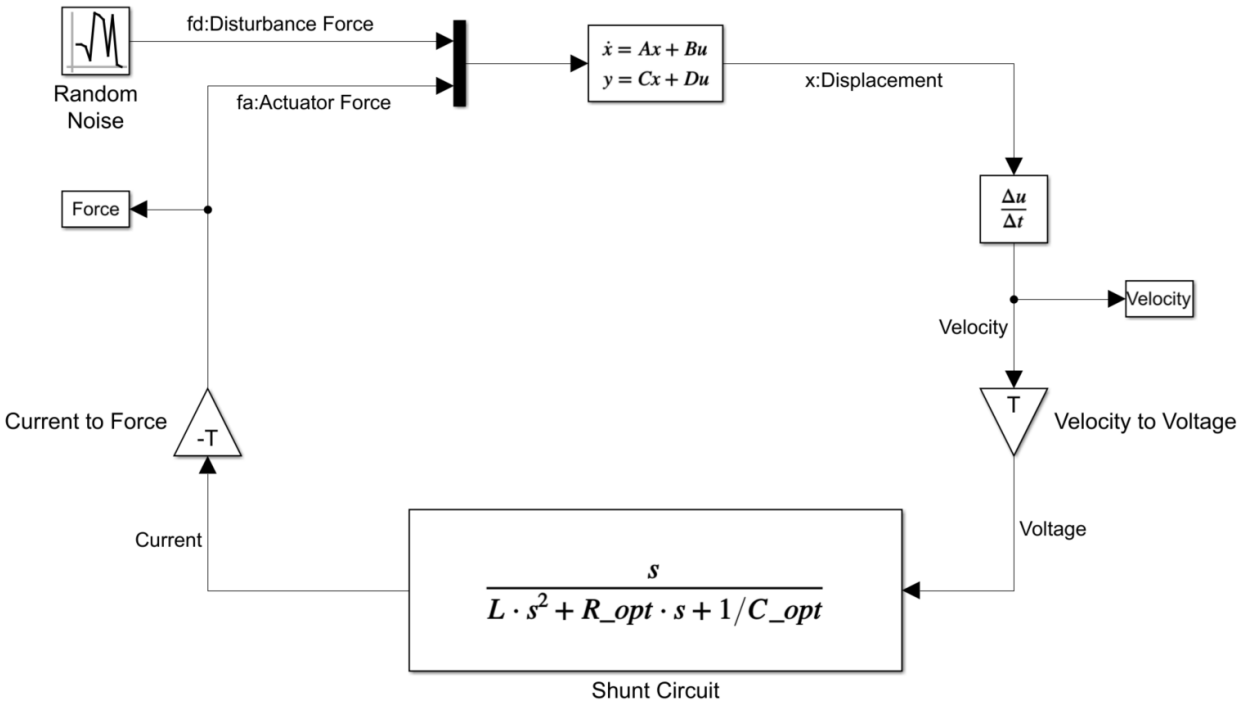

Figure A.1: Configuration of the simulink model to extract the mechanical power of the actuator.

The configuration of the simulink for the system is shown in the Figure A.1. One sees that the system is excited by a uniformly random noise signal distributed over all range of frequency. It can be seen that by derivating the output signal with respect to the time, the velocity of the mass is obtained. Then, by multiplying the signal to the coupling constant of the actuator T, the signal will be proportional to the voltage of the actuator according to the Eq. (2.1). Next, the signal is amplified with a filter (Eq. (2.2)) representing the shunt circuit to extract the current of the actuator. In the end, the actuator force is obtained when the signal is magnified with the coupling constant of the actuator T. In order to calculate the RMS value of the mechanical power in time and frequency domains, the following script is used:

$Pm\_time = Force.Data. * Velocity.Data; \%Mechanical\ power\ in\ time\ domain$
$Pm\_freq = fft(Pm\_time)/sqrt(length(Force.Data)); \%Mechanical\ power\ in\ frequency\ domain$
$rms\_Pm\_time = rms(Pm\_time) \%RMS\ value\ of\ the\ power\ in\ time\ domain$
$rms\_Pm\_freq = rms(abs(Pm\_freq)) \%RMS\ value\ of\ the\ power\ in\ frequency\ domain$

The output is: $rms\_Pm\_time = rms\_Pm\_freq = 9.1991e-05$ which proves the RMS value of the power i time and frequency domains are equal.

Appendix B

H_∞ optimization of linear and nonlinear positive position feedback (PPF)

In this section, the optimal parameters for linear PPF (LPPF) and nonlinear PPF (NPPF) are derived based on the H_∞ criterion.

B.1 H_∞ optimization of linear PPF controller

The system with a linear PPF controller is considered first. This is done by setting the parameter δ in Eqs. (3.56) and (3.57) equal to zero. Thus, the normalized driving point receptance of the primary structure is then given by:

$$y_1 = \frac{s^2 + 2\xi\alpha s + \alpha^2}{s^4 + 2\xi\alpha s^3 + \alpha^2 s^2 + s^2 + 2\xi\alpha s + \alpha^2 - \beta} \tag{B.1}$$

where $s = j\omega$ is the Laplace variable and the magnitude of y_1 is calculated as:

$$|y_1| = \frac{\sqrt{\Omega^4 + (4\xi^2 - 2)\alpha^2\Omega^2 + \alpha^4}}{\sqrt{(\Omega^2 - 1)^2\alpha^4 + 2((2\xi^2 - 1)\Omega^4 + (-2\xi^2 + 1)\Omega^2 + \beta)(\Omega^2 - 1)\alpha^2 + (-\Omega^4 + \Omega^2 + \beta)^2}} \tag{B.2}$$

From the mathematical point of view, the control effectiveness of a PPF controller according to Eq. (B.1) would be similar to that of a tuned mass damper, where an additional zero is introduced to interfere with the resonance of the primary system aiming to reduce certain vibration metrics in the frequency band of interest. Following the H_∞ optimization procedure proposed by Den Hartog [64], the parameters of the linear PPF controller are optimally tuned such that the response at the fixed points are minimized. Fixed point refers to the frequency location at which the magnitude of the driving point receptance of the primary structure is invariant in terms of the damping coefficient of the TMD or the parameter ξ of the PPF controller.
The frequencies at which the fixed points occur can be calculated by differentiating Eq. (B.2) with respect to the damping coefficient, ξ , and equating the derivative to zero, which yields:

$$\Omega_{f1} = \frac{\sqrt{2\alpha^2 + 2 - 2\sqrt{\alpha^4 - 2\alpha^2 + 2\beta + 1}}}{2} \tag{B.3}$$

$$\Omega_{f2} = \frac{\sqrt{2\alpha^2 + 2 + 2\sqrt{\alpha^4 - 2\alpha^2 + 2\beta + 1}}}{2} \tag{B.4}$$

The optimal α is set to equalize the resulting performance index as defined in Eq. (B.2) at the two fixed points. This can be achieved by substituting Eqs. (B.3) and (B.4) into Eq. (B.2) and equating the resulting expressions for $\xi = 0$ which yields,

$$\alpha_{opt} = 1 \tag{B.5}$$

For the optimal ξ, it is sought to make the performance index pass horizontally through the fixed points. Thus, two optimal damping coefficients associated with the two fixed points are obtained:

$$\xi_1 = \sqrt{\frac{3\beta}{4\sqrt{2}(\sqrt{2} - \sqrt{\beta})}} \tag{B.6}$$

$$\xi_1 = \sqrt{\frac{3\beta}{4\sqrt{2}(\sqrt{2} + \sqrt{\beta})}} \tag{B.7}$$

The optimal ξ can be calculated in practice by calculating the quadratic average of Eqs. (B.6) and (B.7), which is given by:

$$\xi_{opt} = \sqrt{\frac{3\beta}{4(2 - \beta)}} \tag{B.8}$$

It should be noted that this approach is an empirical method as the resulting resonance points (the derivative of Eq. (B.2) with respect to Ω is equal to zero) do not necessarily coincide simultaneously with the corresponding fixed points. An exact solution for this problem was proposed in Eq. (B.2), with which the two resulting resonance points are equally damped. In this study this exact approach is not considered because this would result in very long and therefore rather impractical polynomial expressions.

Up to now, only the parameter β (normalized feedback gain) is left un-optimized for implementing the linear PPF controller. The function of the feedback gain β can be assessed by evaluating the magnitude of driving point receptance at the fixed points. This is done by substituting Eqs. (B.3) and (B.5) into Eq. (B.2) for $\xi = 0$ which yields, the minimal maximum response

$$y_{1mm} = \sqrt{\frac{2}{\beta}} \tag{B.9}$$

As shown in Eq. (B.8), the minimal maximum response is inversely proportional to the gain β, indicating that the value of the feedback gain g should be as high as possible without compromising the stability of the active system.
The stability of an active system can be studied by applying the Routh-Hurwitz stability criterion to its closed loop characteristic Eq. (B.6). The characteristic equation of the system can be formed as:

$$A_4 s^4 + A_3 s^3 + A_2 s^2 + A_1 s + A_0 = 0 \tag{B.10}$$

where A_0, A_1, A_2, A_3 and A_4 are the corresponding coefficients of Laplace variable in the denominator of Eq. (B.1).
The Routh-Hurwitz stability criterion states that the roots of the characteristic equation have negative real parts if and only if the following conditions are satisfied:

$$A_0, A_1, A_2, A_3, A_4 > 0 \tag{B.11}$$

$$A_2 A_3 - A_1 A_4 > 0 \tag{B.12}$$

$$A_1 A_2 A_3 - A_1^2 A_4 - A_0 A_3^2 > 0 \tag{B.13}$$

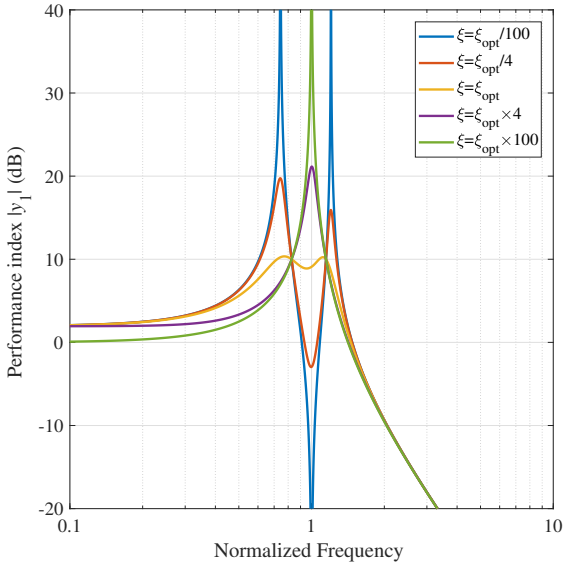

Figure B.1: The driving point receptance for different active damping ratios

It can be derived that the system is stable if and only if the gain β is defined such that:

$$\beta < \alpha^2 \tag{B.14}$$

In the following, numerical studies are performed to illustrate the control effectiveness of the linear PPF controller for the system under consideration. Figure B.1 shows the performance index $|y_1|$ plotted against frequency for five different damping ratios defined as $\frac{\xi}{\xi_{opt}} : 0, 1/4, 1, 4$ and ∞, where the control parameters μ is set to its optimal value as given in Eq. (B.5) and the gain is set to 0.2. It can be seen that all the curves with different damping values intersect at two frequencies and only with the optimal damping the response at the two fixed frequencies becomes the maximum. One should also note that the system becomes dynamically softer with the application of PPF control as the control signal is positively proportional to the displacement of the system in the low frequency range whereas the PPF control effectiveness is similar to that of a negative spring. However, when the damping value approaches infinity, the softening effect disappears as the control action is lost. Figure B.2 depicts the performance index $|y_1|$ plotted against frequency for four different feedback gains namely $\beta : 0, 0.01, 0.05$, and 0.5, where the control parameters α and ξ are both set to their optimal values. As can be seen, the performance index indeed decreases with an increase in the gain as indicated by Eq. (B.8). With this respect, the feedback gain g of the PPF controller can be understood to play the same role as the mass ratio between tuned mass dampers and host primary structures, where better performance comes with a greater values of this quantity. However, the approximation errors induced by the estimation of the damping parameter ξ is more pronounced with an increase in the feedback gain. In the same fashion, the response in the low frequency range will be more amplified because of the negative stiffness effect. Therefore, the maximum feedback β under H_∞ optimization criterion is not only limited by the stability concern, but also by the amplification of the low frequency response.

B.2 H_∞ optimization of nonlinear PPF controller

In this subsection, H_∞ optimization of the NPPF controller is performed. Due to the cubic terms, it is difficult to derive the explicit expression of the performance index from Eqs. (3.56) and (3.57). As reported in [86, 87, 88], harmonic solutions can be used to approximate the exact solutions

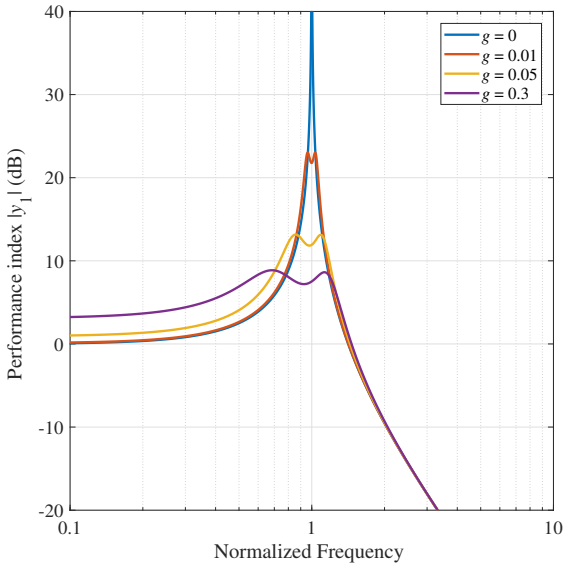

Figure B.2: The driving point receptance for different feedback gains

with a good agreement. In this study, the performance index is approximated using the first-order harmonics. Thus, a pair of one-term harmonic balance approximation is assumed as the solutions:

$$y_1 = A_1 cos(\Omega\tau) + B_1 sin(\Omega\tau) \tag{B.15}$$

$$y_2 = A_2 cos(\Omega\tau) + B_2 sin(\Omega\tau) \tag{B.16}$$

Substituting Eqs. (B.15) and (B.16) into Eqs. (3.56) and (3.57), and applying the approximations $cos(\Omega\tau)^3 = 3/4 cos(\Omega\tau)$ and $sin(\Omega\tau)^3 = 3/4 sin(\Omega\tau)$, a set of polynomial equations is obtained by balancing cosine and sine terms:

$$-A_1\Omega^2 + A_1 + g\Omega^2 A_2 + 3/4\delta A_1(A_1^2 + B_1^2) = 1 \tag{B.17}$$

$$-B_1\Omega^2 + B_1 + g\Omega^2 B_2 + 3/4\delta B_1(A_1^2 + B_1^2) = 0 \tag{B.18}$$

$$-A_2\Omega^2 + 2\xi\alpha\Omega B_2 - A_1 + \alpha^2 A_2 + 3/4\delta\mu A_2(A_1^2 + B_1^2) = 0 \tag{B.19}$$

$$-B_2\Omega^2 - 2\xi\alpha\Omega A_2 - B_1 + \alpha^2 B_2 + 3/4\delta\mu B_2(A_1^2 + B_1^2) = 0 \tag{B.20}$$

Although the original nonlinear differential equations have been transformed to a set of nonlinear algebraic equations, it is not yet possible to find explicit solutions of B.14-B.17. They are instead solved with approximate solutions. It is further assumed that the nonlinear coefficient δ is a small quantity and the harmonic coefficients and can be expanded into series with respect to the primary nonlinear coefficient δ , i.e. $A_1 = A_{11} + \delta A_{12}$, $B_1 = B_{11} + \delta B_{12}$, $A_2 = A_{21} + \delta A_{22}$ and $B_2 = B_{21} + \delta B_{22}$.
Substituting the above ansatz into Eqs. (B.14)-(B.17), and collecting the resulting expressions with respect to the order of the parameter δ, and omitting the expressions whose orders are higher than δ^1, one obtains:

$$(\beta A_{21} - A_{11})\Omega^2 + A_{11} - 1 = 0 \tag{B.21}$$

$$1/4(4\beta A_{22} - 4A_{12})\Omega^2 + 3/4A_{11}^3 + 3/4A_{11}B_{11}^2 + A_{12} = 0 \tag{B.22}$$

$$(\beta B_{21} - B_{11})\Omega^2 + B_{11} = 0 \tag{B.23}$$

$$1/4(4\beta B_{22} - 4B_{12})\Omega^2 + 3/4A_{11}^2 B_{11} + 3/4B_{11}^3 + B_{12} = 0 \tag{B.24}$$

$$1/4(3A_{21}^3 + 3A_{21}B_{21}^2)\beta + 1/4(4\alpha^2 - 4\Omega^2)A_{22} + 2\xi\alpha\Omega B_{22} - A_{12} = 0 \tag{B.25}$$

$$(\alpha^2 - \Omega^2)A_{21} + 2\xi\alpha\Omega B_{21} - A_{11} = 0 \tag{B.26}$$

$$(\alpha^2 - \Omega^2)B_{21} - 2\xi\alpha\Omega A_{21} - B_{11} = 0 \tag{B.27}$$

$$1/4(A_{21}^2 B_{21} + 3B_{21}^3)\beta + 1/4(4\alpha^2 - 4\Omega^2)B_{22} - 2\xi\alpha\Omega A_{22} - B_{12} = 0 \tag{B.28}$$

Solving for A_{ij} and B_{ij} $(i = 1, 2, j = 1, 2)$ from Eqs. (B.18)-(B.25), the resulting solutions are found to be in terms of the control gains ξ, α, β and the normalized frequency Ω. Due to the complexity, these expressions are not given here. Nevertheless, the absolute value of the normalized frequency response $|y_1(\Omega)|$, namely the performance index, can be expressed as:

$$|Q(\Omega)| = \sqrt{A_{11}^2 + B_{11}^2 + 2\delta(A_{11}A_{12} + B_{11}B_{12}) + \delta^2(A_{12}^2 + B_{12}^2)} \tag{B.29}$$

An additional condition is imposed in order to derive the optimal coefficient of the nonlinear compensator β, which is sought to maintain the equal peaks at the fixed points associated with the LPPF controller for the linear primary system i.e.:

$$|Q(\Omega_{f1})| = |Q(\Omega_{f2})| \tag{B.30}$$

Substituting the optimal setting of α and ξ as given in Eqs. (B.5) and (B.8) as well as the solutions of A_{ij} and B_{ij} (i=1,2 , j=1,2) of Eqs. (B.21)-(B.28) into Eq. (B.30), one obtains:

$$\mu_{opt} = 2\beta - 9/16\beta^2 + O(\beta^3) \tag{B.31}$$

In fact, Eq. (B.31) represents a simpler and more easily interpretable relation which is the Taylor series expansion of the exact solution with respect to the feedback gain β given $\beta << 1$. The relative error introduced by the approximation is fewer than 1.5% up to the dimensionless feedback gain.

Up to now, the derivation of the explicit expressions for forming the NPPF controller h(.) is complete wherein the optimal control parameters μ, α and β are given in Eqs. (B.5), (B.8) and (B.31), respectively. As for the maximum feedback gain β for the NPPF controller, Eq. (B.14) which constrains the maximum β for the LPPF controller is still applicable according to the Lyapunov's linearisation theory [83]. This theorem states that if the linearized system is strictly stable, then the equilibrium point for the actual nonlinear system is asymptotically stable. It can be proved that the nonlinear system coupled with the NPPF controller as described by Eqs. (3.56) and (3.57) can be linearized to the same linear system as described in Section B.1. However, the Lyapunov's linearisation theory is only valid for small range of motions around the equilibrium points (a local stability theorem) and it is not yet clear what are the boundary conditions for the linearisation approximations to hold (global stability theorem is needed). It is left for the subject of future work.

B.3 Performance of the NPPF controller

Numerical studies are performed to validate and examine the control effectiveness of the NPPF controller for the Duffing oscillator. The performance index derived from the system governing equations given by Eqs. (3.56) and (3.57) is computed using a path-following algorithm combining harmonic balance and pseudo-arclength continuation [89]. The first 5 harmonics are taken for a good approximation and the convergence requirement. The stability of the solutions is determined using Hill's method and the type of instabilities i.e. fold and Neimark-Sacker bifurcations is detected using a test function based on the Floquet multipliers [89]. The 'stability' in the current context is referred to as the local stability of the solutions of the nonlinear equations where the system motion is always bounded. This is different from the concept discussed in Section B.1 and B.2, where the system motion exponentially increases until the system is destroyed if instability happens. In addition, a modal damping of 1% is added to the primary structure during the computation in order to avoid unnecessary numerical errors i.e. infinite-amplitude responses. This particular value is chosen

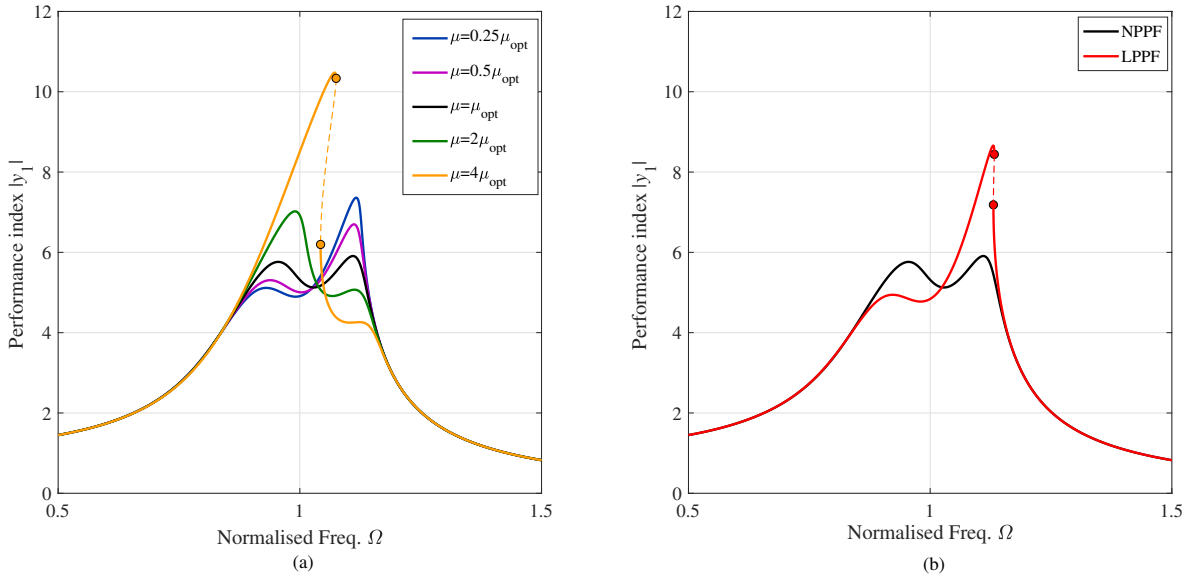

(a) (b)

Figure B.3: The performance index $|y_1|$ with the NPPF controller for the feedback gain of 0.05, the primary nonlinear coefficient δ of 0.003 and: (a) different values of the nonlinear coefficient (b) the optimal nonlinear coefficient μ, and comparison with an optimal LPPF controller (—:stable solution, –: unstable solution, •: fold bifurcation)

as it also represents the modal damping of the experimental set-up that is presented in Section 3.3.2.

The first study is focused on the validity of Eq. (B.31) which describes the optimal coefficient of the nonlinear compensator i.e. the cubic term of the NPPF controller. Figure B.3a plots the frequency response of the performance index of the Duffing oscillator attached with a NPPF controller whose parameters are configured as follows: the normalized feedback gain β is set to 0.05, the damping ratio and the resonance ratio ξ and α are calculated as in Eqs. (B.5) and (B.8), respectively, the nonlinear coefficient δ is set to 0.003 and the parameter μ varies with respect to its optimal value as μ/μ_{opt}: 1/4, 1/2, 1, 2 and 4. It is seen that the response at the first resonance frequency increases with an increase of the parameter μ and an opposite trend is observed for the second resonance peak. The resonance peaks of equal amplitudes are obtained with the optimal setting of the parameter as given in Eq. (B.31). For the parameter setting $\mu/\mu_{opt} = 4$, a pair of fold bifurcations is observed which modifies the stability of the solutions along the frequency response.

Figure B.3b compares the performance index of the Duffing oscillator attached with an optimally tuned NPPF controller and its counterpart optimal LPPF controller for the same parameter configuration $\delta = 0.05$ and $\delta = 0.003$. As can be seen, the LPPF controller is detuned for the system under consideration and a hardening behaviour characteristic of cubic springs with positive coefficients is present at the second resonance peak. On the other hand, the two resonance peaks still remain approximately equal with the NPPF controller which reveals the superior performance of the NPPF controller compared to that of the LPPF controller.

For the second study, the comparison between the LPPF and NPPF controllers is extended for some other values of the nonlinear coefficient δ which is chosen to vary between 0.0001 and 0.008. Figure B.4a compares the frequency response of the Duffing oscillator with the optimally tuned LPPF controller. As can be seen, when is smaller than 0.0008, the LPPF controller works properly, where the responses at the two resonances remain equal and the classical linear results are observed. This is because the input excitation level is not high enough to trigger the nonlinearity of

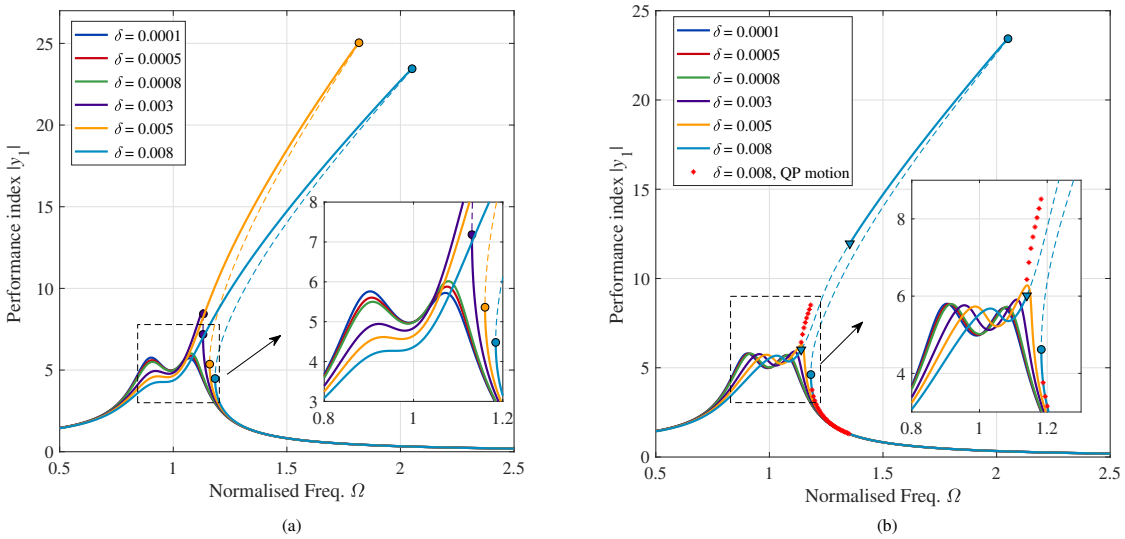

(a) (b)

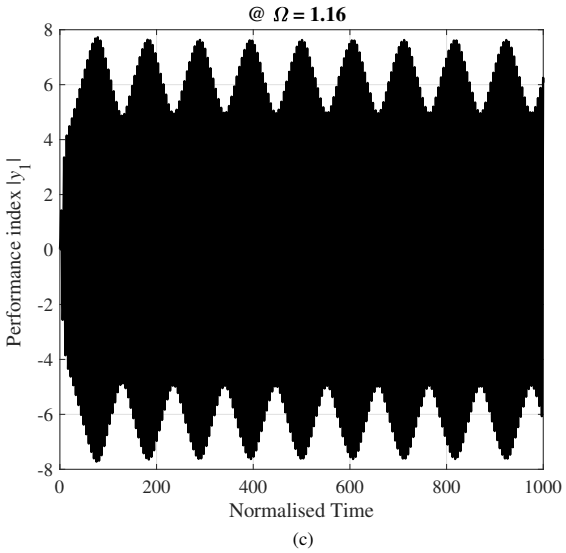

(c)

Figure B.4: The performance of the system under consideration where the feedback gain is set to 0.05 and the primary nonlinear coefficient δ varies between 0.0001 and 0.008: (a) with LPPF controller, (b) with NPPF controller and (c) quasiperiodic motion at $\Omega = 1.16$ (—:stable solution, –: unstable solution, •: fold bifurcation, ▼: Neimark-Sacker bifurcation

the primary system. However when is increased to 0.003, a visible difference between the two peak amplitudes is observed, which indicates that the optimal LPPF controller starts to be detuned. Above 0.005, the controller is completely detuned as the response at the second resonance is much greater than that at the first resonance. It is also noted that a sudden shift of the location of the second resonance occurs when is increased from 0.003 to 0.005 which is not the case for example when is increased from 0.005 to 0.008. This phenomenon is observed because there is an isolated resonance branch, also termed an isola, coexisting with the main frequency response function curve due to the non-uniqueness solutions of nonlinear equations. For , the isola merges with the main curve at the second resonance leading to a sudden shift of the resonance. On the ground of the observed results, it can be concluded that the LPPF is only effective for weakly nonlinear systems

in terms of vibration mitigation.

Figure B.4b depicts the control effectiveness of the optimal NPPF controller for the same system parameter configuration as that applied for the LPPF controller. It shows that the nonlinear controller can compensate LPPF detuning until δ reaches 0.005. However, it is not able to fully eliminate the coalescence of the isola and the main frequency response curve by the proposed NPPF controller as seen for the case when $\delta = 0.008$. This means that the NPPF controller fails to maintain the equal peak property in the presence of a very strong nonlinearity. In addition, another type of dynamical instability i.e. a pair of Neimark-Sacker bifurcations is observed which leads to a branch of quasiperiodic solutions. The quasiperiodic solutions are computed using direct time integration techniques and the maximum peak amplitude is taken as the response for the plot. It is noted that the quasiperiodic branch suddenly breaks around the first fold bifurcation point and the quasiperiodic solutions after this point merge with the normal oscillation solutions. This indicates that the second half branch of the quasiperiodic oscillations may not be stable i.e. it cannot be physically realized.

A time series of the quasiperiodic motions at $\Omega = 1.16$ is plotted in Figure B.4c. It is shown that the control performance degrades in the presence of the quasiperiodic motions as the resonance peak is amplified. Nevertheless, the proposed NPPF controller is shown to be able to delay the occurrence of the coalescence of the isola and the main frequency response function curve for relatively large forcing amplitudes compared to the LPPF controller, which also allows to extend the linearity bandwidth of the nonlinear system under control to a relatively large extent. It is foreseen that this bandwidth can be further extended if β is assumed to be also dependent on the nonlinear coefficient δ instead of Eq. (B.29) which is solely determined by β. This is also left for the subject of future work.

Bibliography

[1] M. P. Boyce, *Gas turbine engineering handbook*. Elsevier, 2011.

[2] R. Royce, *The jet engine*. John Wiley & Sons, 2015.

[3] A. T. S. Bureau, "Examination of a failed fan blade turbofan engine," 2001.

[4] B. Mokrani, *Piezoelectric shunt damping of rotationally periodic structures*. PhD thesis, Ph. D. Thesis, Université Libre de Bruxelles, Active Structures Laboratory ..., 2015.

[5] B. Mokrani, R. Bastaits, R. Viguié, and A. Preumont, "Vibration damping of turbomachinery components with piezoelectric transducers: Theory and experiment," in *ISMA2012 International Conference on Noise and Vibration Engineering, Leuven, Belgium*, vol. 69, 2012.

[6] N. Nguyen, "Blading system and method for controlling structural vibrations," Aug. 15 2000. US Patent 6,102,664.

[7] B. Mokrani, R. Bastaits, M. Horodinca, I. Romanescu, I. Burda, R. Viguié, and A. Preumont, "Parallel piezoelectric shunt damping of rotationally periodic structures," *Advances in Materials Science and Engineering*, vol. 2015, 2015.

[8] K. P. Duffy, B. B. Choi, A. J. Provenza, J. B. Min, and N. Kray, "Active piezoelectric vibration control of subscale composite fan blades," *Journal of engineering for gas turbines and power*, vol. 135, no. 1, 2013.

[9] J. C. Simonich, "Actuator feasibility study for active control of ducted axial fan noise," 1994.

[10] J. Tang and K. Wang, "Active-passive hybrid piezoelectric networks for vibration control: comparisons and improvement," *Smart Materials and Structures*, vol. 10, no. 4, p. 794, 2001.

[11] G. Zhao, G. Raze, A. Paknejad, A. Deraemaeker, G. Kerschen, and C. Collette, "Active tuned inerter-damper for smart structures and its h_∞ optimisation," *Mechanical systems and signal processing*, vol. 129, pp. 470–478, 2019.

[12] A. R. Rao and B. Dutta, "Vibration analysis for detecting failure of compressor blade," *Engineering Failure Analysis*, vol. 25, pp. 211–218, 2012.

[13] D. I. Jones, *Handbook of viscoelastic vibration damping*. John Wiley & Sons, 2001.

[14] A. Ferri, "Friction damping and isolation systems," *Journal of vibration and acoustics*, 1995.

[15] J. Ormondroyd, "The theory of the dynamic vibration absorber," *Trans., ASME, Applied Mechanics*, vol. 50, pp. 9–22, 1928.

[16] N. W. Hagood and A. von Flotow, "Damping of structural vibrations with piezoelectric materials and passive electrical networks," *Journal of sound and vibration*, vol. 146, no. 2, pp. 243–268, 1991.

[17] S. Behrens, A. J. Fleming, and S. R. Moheimani, "Passive vibration control via electromagnetic shunt damping," *IEEE/ASME transactions on mechatronics*, vol. 10, no. 1, pp. 118–122, 2005.

[18] J. H. Griffin, "A review of friction damping of turbine blade vibration," *International Journal of Turbo and Jet Engines*, vol. 7, no. 3-4, pp. 297–308, 1990.

[19] S. Yeo and P. J. Goodman, "Vibration damping," Dec. 9 2003. US Patent 6,659,725.

[20] D. Laxalde, C. Gibert, and F. Thouverez, "Experimental and numerical investigations of friction rings damping of blisks," in *ASME Turbo Expo 2008: Power for Land, Sea, and Air*, pp. 469–479, American Society of Mechanical Engineers Digital Collection, 2008.

[21] M. L. Stangeland, R. E. Berenson, G. A. Davis, and E. J. Krieg, "Turbine blisk rim friction finger damper," Apr. 23 2002. US Patent 6,375,428.

[22] S. M. Schwarzendahl, J. Szwedowicz, M. Neubauer, L. Panning, and J. Wallaschek, "On blade damping technology using passive piezoelectric dampers," in *ASME Turbo Expo 2012: Turbine Technical Conference and Exposition*, pp. 1205–1215, American Society of Mechanical Engineers Digital Collection, 2012.

[23] J. Kauffman and G. Lesieutre, "Vibration reduction of turbomachinery bladed disks with changing dynamics using piezoelectric materials," in *52nd AIAA/ASME/ASCE/AHS/ASC Structures, Structural Dynamics and Materials Conference 19th AIAA/ASME/AHS Adaptive Structures Conference 13t*, p. 2003, 2011.

[24] A. Hohl, M. Neubauer, S. Schwarzendahl, L. Panning, and J. Wallaschek, "Active and semi-active vibration damping of turbine blades with piezoceramics," in *Active and Passive Smart Structures and Integrated Systems 2009*, vol. 7288, p. 72881H, International Society for Optics and Photonics, 2009.

[25] A. Preumont, *Vibration control of active structures*, vol. 2. Springer, 1997.

[26] M. J. Balas, "Direct velocity feedback control of large space structures," *Journal of Guidance and Control*, vol. 2, no. 3, pp. 252–253, 1979.

[27] G. Zhao, A. Paknejad, G. Raze, A. Deraemaeker, G. Kerschen, and C. Collette, "Nonlinear positive position feedback control for mitigation of nonlinear vibrations," *Mechanical Systems and Signal Processing*, vol. 132, pp. 457–470, 2019.

[28] A. Fleming, S. Behrens, and S. Moheimani, "Synthetic impedance for implementation of piezoelectric shunt-damping circuits," *Electronics Letters*, vol. 36, no. 18, pp. 1525–1526, 2000.

[29] A. Preumont, A. Francois, F. Bossens, and A. ABU-HANIEH, "Force feedback versus acceleration feedback in active vibration isolation," *Journal of sound and vibration*, vol. 257, no. 4, pp. 605–613, 2002.

[30] A. Preumont and K. Seto, *Active control of structures*. Wiley Online Library, 2008.

[31] M. C. Smith, "Synthesis of mechanical networks: the inerter," *IEEE Transactions on automatic control*, vol. 47, no. 10, pp. 1648–1662, 2002.

[32] W. Sun, D. Thompson, and J. Zhou, "A mechanism for overcoming the effects of the internal resonances of coil springs on vibration transmissibility," *Journal of Sound and Vibration*, vol. 471, p. 115145, 2020.

[33] M. Z. Chen, C. Papageorgiou, F. Scheibe, F.-C. Wang, and M. C. Smith, "The missing mechanical circuit element," *IEEE Circuits and Systems Magazine*, vol. 9, no. 1, pp. 10–26, 2009.

[34] C. Papageorgiou, N. E. Houghton, and M. C. Smith, "Experimental testing and analysis of inerter devices," *Journal of dynamic systems, measurement, and control*, vol. 131, no. 1, 2009.

[35] X. Liu, J. Z. Jiang, B. Titurus, and A. Harrison, "Model identification methodology for fluid-based inerters," *Mechanical Systems and Signal Processing*, vol. 106, pp. 479–494, 2018.

[36] S. Swift, M. C. Smith, A. Glover, C. Papageorgiou, B. Gartner, and N. E. Houghton, "Design and modelling of a fluid inerter," *International Journal of Control*, vol. 86, no. 11, pp. 2035–2051, 2013.

[37] B. De Marneffe, M. Avraam, A. Deraemaeker, M. Horodinca, and A. Preumont, "Vibration isolation of precision payloads: A six-axis electromagnetic relaxation isolator," *Journal of guidance, control, and dynamics*, vol. 32, no. 2, pp. 395–401, 2009.

[38] A. Fleming, S. Behrens, and S. Moheimani, "Reducing the inductance requirements of piezoelectric shunt damping systems," *Smart materials and structures*, vol. 12, no. 1, p. 57, 2003.

[39] S. Zhou, C. Jean-Mistral, and S. Chesné, "Electromagnetic shunt damping with negative impedances: optimization and analysis," *Journal of Sound and Vibration*, vol. 445, pp. 188–203, 2019.

[40] I. Lazar, S. Neild, and D. Wagg, "Using an inerter-based device for structural vibration suppression," *Earthquake Engineering & Structural Dynamics*, vol. 43, no. 8, pp. 1129–1147, 2014.

[41] J. Høgsberg, M. L. Brodersen, and S. Krenk, "Resonant passive–active vibration absorber with integrated force feedback control," *Smart Materials and Structures*, vol. 25, no. 4, p. 047001, 2016.

[42] N. Alujevic, I. Catipovic, H. Wolf, and N. Vladimir, "Synthesis of the inerter by direct acceleration feedback," in *Proceedings of 23rd International Congress on Acoustic*, Physical aspects for active control of noise and vibration, (Aachen, Germany), 2019.

[43] A. Paknejad, G. Zhao, S. Chesné, A. Deraemaeker, and C. Collette, "Hybrid electromagnetic shunt damper for vibration control," *Journal of Vibration and Acoustics*, vol. 143, no. 2, 2020.

[44] D. Sutliff, Z. Hu, F. Pla, L. Heidelberg, D. Sutliff, Z. Hu, F. Pla, and L. Heidelberg, "Active noise control of low speed fan rotor-stator modes," in *3rd AIAA/CEAS Aeroacoustics Conference*, p. 1641, 1996.

[45] R. H. Thomas, R. A. Burdisso, C. R. Fuller, and W. F. O'Brien, "Active control of fan noise from a turbofan engine," *AIAA journal*, vol. 32, no. 1, pp. 23–30, 1994.

[46] K. A. Kousen and J. M. Verdon, "Active control of wake/blade-row interaction noise," *AIAA journal*, vol. 32, no. 10, pp. 1953–1960, 1994.

[47] P. Remington, D. Sutliff, and S. Sommerfeldt, "Active control of low-speed fan tonal noise using actuators mounted in stator vanes: part 1 control system design and implementation," in *9th AIAA/CEAS Aeroacoustics Conference and Exhibit*, p. 3190, 2003.

[48] M. Tso, J. Yuan, and W. O. Wong, "Design and experimental study of a hybrid vibration absorber for global vibration control," *Engineering structures*, vol. 56, pp. 1058–1069, 2013.

[49] P. Hagedorn and G. Spelsberg-Korspeter, *Active and passive vibration control of structures*, vol. 558. Springer, 2014.

[50] C. Collette and S. Chesne, "Robust hybrid mass damper," *Journal of sound and vibration*, vol. 375, pp. 19–27, 2016.

[51] S. Chesné and C. Collette, "Experimental validation of fail-safe hybrid mass damper," *Journal of Vibration and Control*, vol. 24, no. 19, pp. 4395–4406, 2018.

[52] G. S. Agnes, "Active/passive piezoelectric vibration suppression," in *Smart Structures and Materials 1994: Passive Damping*, vol. 2193, (Orlando, FL, United States), pp. 24–34, International Society for Optics and Photonics, 1994.

[53] M. Tsai and K. Wang, "On the structural damping characteristics of active piezoelectric actuators with passive shunt," *Journal of Sound and Vibration*, vol. 221, no. 1, pp. 1–22, 1999.

[54] R. A. Morgan and K. Wang, "An integrated active-parametric control approach for active-passive hybrid piezoelectric network with variable resistance," *Journal of intelligent material systems and structures*, vol. 9, no. 7, pp. 564–573, 1998.

[55] R. Morgan and K. Wang, "An active-passive piezoelectric absorber for structural vibration control under harmonic excitations with time-varying frequency, part 1: algorithm development and analysis," *J. Vib. Acoust.*, vol. 124, no. 1, pp. 77–83, 2002.

[56] R. Morgan and K. Wang, "An active-passive piezoelectric absorber for structural vibration control under harmonic excitations with time-varying frequency, part 2: experimental validation and parametric study," *J. Vib. Acoust.*, vol. 124, no. 1, pp. 84–89, 2002.

[57] M. Li, B. Fang, D. Cao, and W. Huang, "Modeling and analysis of cantilever beam with active-passive hybrid piezoelectric network," *Science China Technological Sciences*, vol. 56, no. 9, pp. 2326–2335, 2013.

[58] M. Tsai and K. Wang, "A coupled robust control/optimization approach for active-passive hybrid piezoelectric networks," *Smart materials and structures*, vol. 11, no. 3, p. 389, 2002.

[59] Y. Zhao, "Vibration suppression of a quadrilateral plate using hybrid piezoelectric circuits," *Journal of Vibration and Control*, vol. 16, no. 5, pp. 701–720, 2010.

[60] M. Tsai and K. Wang, "Control of a ring structure with multiple active-passive hybrid piezoelectrical networks," *Smart Materials and Structures*, vol. 5, no. 5, p. 695, 1996.

[61] S. Behrens, A. J. Fleming, and S. R. Moheimani, "Passive vibration control via electromagnetic shunt damping," *IEEE/ASME transactions on mechatronics*, vol. 10, no. 1, pp. 118–122, 2005.

[62] B. De Marneffe, "Active and passive vibration isolation and damping via shunted transducers," *These, Faculté des Sciences Appliquées, Université Libre de Bruxelles*, 2007.

[63] T. Inoue, Y. Ishida, and M. Sumi, "Vibration suppression using electromagnetic resonant shunt damper," *Journal of Vibration and Acoustics*, vol. 130, no. 4, 2008.

[64] J. P. Den Hartog, *Mechanical vibrations*. Courier Corporation, 1985.

[65] X. Tang, Y. Liu, W. Cui, and L. Zuo, "Analytical solutions to h_2 and h_∞ optimizations of resonant shunted electromagnetic tuned mass damper and vibration energy harvester," *Journal of Vibration and Acoustics*, vol. 138, no. 1, 2016.

[66] S. Zhu, W. Shen, and X. Qian, "Dynamic analogy between an electromagnetic shunt damper and a tuned mass damper," *Smart materials and structures*, vol. 22, no. 11, p. 115018, 2013.

[67] J. Ormondroyd, "The theory of the dynamic vibration absorber," *Trans., ASME, Applied Mechanics*, vol. 50, pp. 9–22, 1928.

[68] A. McDaid and B. Mace, "A self-tuning electromagnetic vibration absorber with adaptive shunt electronics," *Smart materials and structures*, vol. 22, no. 10, p. 105013, 2013.

[69] A. J. McDaid and B. R. Mace, "A robust adaptive tuned vibration absorber using semi-passive shunt electronics," *IEEE Transactions on Industrial Electronics*, vol. 63, no. 8, pp. 5069–5077, 2016.

[70] J. C. Doyle, B. A. Francis, and A. R. Tannenbaum, *Feedback control theory*. Courier Corporation, 2013.

[71] M. Zilletti, P. Gardonio, and S. J. Elliott, "Optimisation of a velocity feedback controller to minimise kinetic energy and maximise power dissipation," *Journal of Sound and Vibration*, vol. 333, no. 19, pp. 4405–4414, 2014.

[72] S. H. Crandall and W. D. Mark, *Random vibration in mechanical systems*. Academic Press, 2014.

[73] B. Yan, X. Zhang, Y. Luo, Z. Zhang, S. Xie, and Y. Zhang, "Negative impedance shunted electromagnetic absorber for broadband absorbing: experimental investigation," *Smart materials and structures*, vol. 23, no. 12, p. 125044, 2014.

[74] B. Yan, K. Wang, C.-X. Kang, X.-N. Zhang, and C.-Y. Wu, "Self-sensing electromagnetic transducer for vibration control of space antenna reflector," *IEEE/ASME Transactions on Mechatronics*, vol. 22, no. 5, pp. 1944–1951, 2017.

[75] S. Zhou, C. Jean-Mistral, and S. Chesné, "Electromagnetic shunt damping with negative impedances: optimization and analysis," *Journal of Sound and Vibration*, vol. 445, pp. 188–203, 2019.

[76] A. Preumont, J.-P. Dufour, and C. Malekian, "Active damping by a local force feedback with piezoelectric actuators," *Journal of guidance, control, and dynamics*, vol. 15, no. 2, pp. 390–395, 1992.

[77] G. Zhao, A. Paknejad, A. Deraemaeker, and C. Collette, "h_∞ optimization of an integral force feedback controller," *Journal of vibration and control*, vol. 25, no. 17, pp. 2330–2339, 2019.

[78] J. Yang, J. Z. Jiang, X. Zhu, and H. Chen, "Performance of a dual-stage inerter-based vibration isolator," *Procedia engineering*, vol. 199, pp. 1822–1827, 2017.

[79] K. Ramakrishnan, L. Yang, F. M. Ballo, M. Gobbi, and G. Mastinu, "Multi-objective optimization of road vehicle passive suspensions with inerter," in *International Design Engineering Technical Conferences and Computers and Information in Engineering Conference*, vol. 50138, p. V003T01A007, American Society of Mechanical Engineers, 2016.

[80] J. Z. Jiang, A. Z. Matamoros-Sanchez, R. M. Goodall, and M. C. Smith, "Passive suspensions incorporating inerters for railway vehicles," *Vehicle System Dynamics*, vol. 50, no. sup1, pp. 263–276, 2012.

[81] Y. Li, J. Z. Jiang, and S. Neild, "Inerter-based configurations for main-landing-gear shimmy suppression," *Journal of Aircraft*, vol. 54, no. 2, pp. 684–693, 2017.

[82] A. Paknejad, G. Zhao, M. Osée, A. Deraemaeker, F. Robert, and C. Collette, "A novel design of positive position feedback controller based on maximum damping and h 2 optimization," *Journal of Vibration and Control*, p. 1077546319892755, 2020.

[83] J.-J. E. Slotine, W. Li, *et al.*, *Applied nonlinear control*, vol. 199. Prentice hall Englewood Cliffs, NJ, 1991.

[84] P. Horowitz and W. Hill, *The art of electronics*. Cambridge Univ. Press, 1989.

[85] S. Chesne, K. Billon, C. Collette, and G. Zhao, "Power flow analysis for hybrid mass damper design," in *ASME 2018 International Design Engineering Technical Conferences and Computers and Information in Engineering Conference*, American Society of Mechanical Engineers Digital Collection, 2018.

[86] G. Habib, T. Detroux, R. Viguie, and G. Kerschen, "Nonlinear generalization of den hartog's equal-peak method," *Mechanical Systems and Signal Processing*, vol. 52, pp. 17–28, 2015.

[87] T. Detroux, G. Habib, L. Masset, and G. Kerschen, "Performance, robustness and sensitivity analysis of the nonlinear tuned vibration absorber," *Mechanical Systems and Signal Processing*, vol. 60, pp. 799–809, 2015.

[88] G. Habib and G. Kerschen, "A principle of similarity for nonlinear vibration absorbers," *Physica D: Nonlinear Phenomena*, vol. 332, pp. 1–8, 2016.

[89] T. Detroux, L. Renson, L. Masset, and G. Kerschen, "The harmonic balance method for bifurcation analysis of large-scale nonlinear mechanical systems," *Computer Methods in Applied Mechanics and Engineering*, vol. 296, pp. 18–38, 2015.

Publications associated with this thesis

The complete list of the author's publications is available in the institutional repository difusion with following online address: https://difusion.ulb.ac.be/

Journal articles

Paknejad, Ahmad, Guoying Zhao, Simon Chesné, Arnaud Deraemaeker, and Christophe Collette. "Hybrid Electromagnetic Shunt Damper for Vibration Control." Journal of Vibration and Acoustics 143, no. 2 (2021): 021010.

Paknejad, Ahmad, Gouying Zhao, Michel Osee, Arnaud Deraemaeker, Frederic Robert, and Christophe Collette. "A novel design of positive position feedback controller based on maximum damping and H_2 optimization." Journal of Vibration and Control 26, no. 15-16 (2020): 1155-1164.

Paknejad, Ahmad, Guoying Zhao, Simon Chesne, Arnaud Deraemaeker, and Christophe Collette. "Design and optimization of a novel resonant control law using force feedback for vibration mitigation." Journal of Structural Control and Health Monitoring In press.

Zhao, Guoying, Ghislain Raze, Ahmad Paknejad, Arnaud Deraemaeker, Gaetan Kerschen, and Christophe Collette. "Active nonlinear energy sink using force feedback under transient regime." Nonlinear Dynamics 102, no. 3 (2020): 1319-1336.

Raze, Ghislain, Ahmad Paknejad, Guoying Zhao, Christophe Collette, and Gaetan Kerschen. "Multimodal vibration damping using a simplified current blocking shunt circuit." Journal of Intelligent Material Systems and Structures 31, no. 14 (2020): 1731-1747.

Lacaze, Florian, Ahmad Paknejad, Didier Remond, and Simon Chesne. "Improved integral force feedback controllers for lightweight flexible structures." Journal of Vibration and Control (2020): 1077546320974549.

Zhao, Guoying, Ghislain Raze, Ahmad Paknejad, Arnaud Deraemaeker, Gaëtan Kerschen, and Christophe Collette. "Active nonlinear inerter damper for vibration mitigation of Duffing oscillators." Journal of Sound and Vibration 473 (2020): 115236.

Zhao, Guoying, Ahmad Paknejad, Ghislain Raze, Arnaud Deraemaeker, Gaëtan Kerschen, and Christophe Collette. "Nonlinear positive position feedback control for mitigation of nonlinear vibrations." Mechanical Systems and Signal Processing 132 (2019): 457-470.

Zhao, Guoying, A. Paknejad, Arnaud Deraemaeker, and Christophe Collette. "H_∞ optimization of an integral force feedback controller." Journal of vibration and control 25, no. 17 (2019): 2330-2339.

Zhao, Guoying, Ghislain Raze, Ahmad Paknejad, Arnaud Deraemaeker, Gaetan Kerschen, and Christophe Collette. "Active tuned inerter-damper for smart structures and its H_∞ optimisation." Mechanical Systems and Signal Processing 129 (2019): 470-478.

Conference articles

Paknejad, Ahmad, Ghislain Raze, Guoying Zhao, Arnaud Deraemaeker, Gaëtan Kerschen, and Christophe Collette. "Active vibration damping of bladed structures." In Proceedings of ISMA 2020-International Conference on Noise and Vibration Engineering and USD 2020-International Conference on Uncertainty in Structural Dynamics, pp. 105-114. 2020.

Paknejad, Ahmad, Ghislain Raze, Guoying Zhao, Michel Osée, Arnaud Deraemaeker, Frédéric Robert, Gaëtan Kerschen, and Christophe Collette. "Hybridization of Active Control and Pasive Resonant Shunt." In Proceedings of the 9th ECCOMAS Thematic Conference on Smart Structures and Materials, pp. 930-941. International Centre for Numerical Methods in Engineering (CIMNE), 2019.

Raze, Ghislain, Jennifer Dietrich, Ahmad Paknejad, Boris Lossouarn, Guoying Zhao, Arnaud Deraemaeker, Christophe Collette, and Gaëtan Kerschen. "Passive control of a periodic structure using a network of periodically-coupled piezoelectric shunt circuits." In Proceedings of ISMA 2020-International Conference on Noise and Vibration Engineering and USD 2020-International Conference on Uncertainty in Structural Dynamics, pp. 145-160. 2020.

Zhao, Guoying, Ghislain Raze, Ahmad Paknejad, Arnaud Deraemaeker, Gaëtan Kerschen, and Christophe Collette. "Active Nonlinear Energy Sink Using Integral Force Feedback." In Proceedings of the International Modal Analysis Conference (IMAC) XXXVIII. 2020.

Raze, Ghislain, Ahmad Paknejad, Guoying Zhao, Valery Broun, Christophe Collette, and Gaetan Kirschen. "Suppression of delay-induced instabilities of digital piezoelectric vibration absorbers." (2019).

Raze, Ghislain, Boris Lossouarn, Ahmad Paknejad, Guoying Zhao, Jean-François Deü, Christophe Collette, and Gaëtan Kerschen. "A multimodal nonlinear piezoelectric vibration absorber." In 28th International Conference on Noise and Vibration Engineering, ISMA2018. 2018.

Zhao, Guoying, Ahmad Paknejad, Ghislain Raze, Gaëtan Kerschen, and Christophe Collette. "H_∞ optimization of positive position feedback control for mitigation of nonlinear vibrations." Proceedings of ISMA2018 and USD2018 (2018): 143-151.

Zhao, Guoying, Ahmad Paknejad, Ghislain Raze, Gaëtan Kerschen, and Christophe Collette. "H_∞ optimization of an enhanced force feedback controller for mitigation of nonlinear vibrations." In 7th World Conference on Structural Vibration Control. 2018.